KTH ROYAL INSTITUTE
OF TECHNOLOGY

Doctoral Thesis in Physics

Development of Encapsulated UN-UO_2 Accident Tolerant Fuel

DIOGO RIBEIRO COSTA

Stockholm, Sweden 2023

Development of Encapsulated UN-UO_2 Accident Tolerant Fuel

DIOGO RIBEIRO COSTA

Academic Dissertation which, with due permission of the KTH Royal Institute of Technology, is submitted for public defence for the Degree of Doctor of Philosophy on Friday the 2nd June 2023, at 14:00. in F3, Lindstedtsvägen 26, Stockholm.

Doctoral Thesis in Physics
KTH Royal Institute of Technology
Stockholm, Sweden 2023

ISBN 978-91-8040-561-4
TRITA-SCI-FOU 2023:17

Printed by: Universitetsservice US-AB, Sweden 2023

Abstract

Accident tolerant fuels (ATFs) are designed to endure a severe accident in the reactor core longer than the standard UO_2-Zr alloy systems used in light water reactors (LWRs). Composite fuels such as UN-UO_2 are being considered as an ATF concept to address the lower oxidation resistance of the UN fuel from a safety perspective for use in LWRs, whilst improving the in-reactor behaviour of the UO_2 fuel. The main objective of this thesis is to fabricate, characterise, and evaluate an innovative ATF concept for LWRs: encapsulated UN spheres as additives for the standard UO_2 fuel. Several development steps were applied to understand the influence of the sintering parameters on the UN-UO_2 fuel microstructure, evaluate potential coating candidates to encapsulate the UN spheres by different coating methodologies, assess the oxidation resistance of the composites, and estimate the thermal behaviours of uncoated and encapsulated UN-UO_2 fuels. All composites were sintered by the spark plasma sintering method and characterised by many complementary microstructural techniques. Molybdenum and tungsten are shown, using a combination of modelling and experiments, to be good material candidates for the protective coating. It is shown that the powder coating methods form a thick, dense, and non-uniform coating layer onto spheres, while the chemical and vapour deposition methods provide thinner and more uniform layers. Finite element modelling indicates that the fuel centreline temperature may be reduced by more than 400 K when 70 wt% of encapsulated UN spheres are used as compared to the reference UO_2. Moreover, the severity of the degradation of the nitride phase is reduced when embedded in a UO_2 matrix and may also be reduced even more by the presence of a coating layer. These results contribute to further developments in methodologies for fabricating, characterising, and evaluating accident tolerant fuels within LWRs.

Sammanfattning

Olyckstoleranta bränslen (ATF) är utformade för att motstå en allvarlig olycka i reaktorhärden längre än de standard UO_2-Zr system som används i lättvattenreaktorer (LWR) idag. Kompositbränslen som UN-UO_2 anses vara ett ATF koncept som kan förbättra den lägre oxidationsbeständigheten hos UN bränslet ur ett säkerhetsperspektiv för användning i LWR, samtidigt som UO_2-bränslets beteende och prestanda i reaktorn förbättras. Huvudsyftet med denna avhandling är att tillverka, karakterisera och utvärdera ett innovativt ATF-koncept för LWR: inkapslade UN-sfärer som tillsatser för standardbränslet UO_2. Flera utvecklingssteg tillämpades för att förstå inverkan av sintringsparametrarna på mikrostrukturen för UN-UO_2 bränslet, utvärdera potentiella beläggningskandidater för att kapsla in UN sfärerna med hjälp av olika beläggningsmetoder, bedöma kompositernas oxidationsbeständighet och uppskatta det termiska beteendet hos obelagda och inkapslade UN-UO_2 bränslen. Alla kompositer sintrades med starkströmsassisterad varmpressning (SPS) och karakteriserades av flera komplementära tekniker. Molybden och volfram visar sig vara bra materialkandidater för den skyddande beläggningen med hjälp av en kombination av modellering och experiment. Det visas att pulverlackeringsmetoderna bildar ett tjockt, tätt men ojämnt skikt på sfärerna, medan kemiska- och fysikaliska- ångavsättningsmetoder ger tunnare och mer enhetliga skikt. Finita elementmodellering indikerar att bränslets centertemperatur kan minskas med mer än 400 K när 70 wt% av inkapslade UN-sfärer används jämfört med referensen UO_2. Dessutom reduceras degraderingen av nitridfasen när den är inbäddad i en UO_2-matris och den kan också reduceras ännu mer genom närvaron av ett beläggningsskikt. Dessa resultat bidrar till ytterligare utveckling av metoder för att tillverka, karakterisera, och utvärdera olyckstoleranta bränslen för LWR.

Resumo

Combustíveis tolerantes a acidentes (ATFs) são projetados para suportar um acidente severo no núcleo do reator por mais tempo que os sistemas combustíveis padrão composto por UO_2 e liga de Zr, atualmente usados em reatores de água leve (LWRs). Combustíveis compósitos do tipo UN-UO_2 estão sendo considerados como um conceito ATF para solucionar a inferior resistência à oxidação do combustível UN, tendo em vista perspectivas de segurança para uso em LWRs, enquanto melhora o comportamento do combustível de UO_2 no reator. O objetivo principal desta tese é fabricar, caracterizar, e avaliar um conceito inovador de ATF para LWRs: esferas de UN encapsuladas como aditivos para o combustível padrão de UO_2. Várias etapas de desenvolvimento foram aplicadas para: entender a influência dos parâmetros de sinterização na microestrutura do combustível UN-UO_2, avaliar potenciais candidatos para encapsular as esferas de UN utilizando diferentes metodologias de revestimento, acessar a resistência à oxidação dos compósitos, e estimar o comportamento térmico dos combustíveis compósitos UN-UO_2 sem e com revestimentos. Todos os compósitos foram sinterizados pelo método de sinterização por descarga elétrica (SPS) e caracterizados utilizando diversas técnicas de caracterização microestrutural complementares. Molibdênio e tungstênio demonstraram ser bons materiais candidatos para o revestimento protetivo pela combinação de resultados de modelagem e experimentos. É demonstrado que o método de revestimento utilizando pó forma uma camada espessa, densa e não uniforme nas esferas, enquanto os métodos de deposição química e a vapor proporcionam camadas mais finas e uniformes. Modelagem por elementos finitos indica que a temperatura central do combustível pode ser reduzida em mais de 400 K quando 70 %m de esferas encapsuladas são utilizados, em comparação ao combustível referência UO_2. Além disso, a severidade da degradação da fase nitreto é reduzida quando integrada na matriz de UO_2, podendo ser reduzida ainda mais pela presença de uma camada de revestimento. Esses resultados contribuem para futuros desenvolvimentos em metodologias de fabricação, caracterização e avaliação de combustíveis tolerantes a acidentes em LWRs.

List of Publications

Included publications

I. **D. R. Costa**, M. Hedberg, S. C. Middleburgh, J. Wallenius, P. Olsson, and D. A. Lopes, *UN microspheres embedded in UO_2 matrix: An innovative accident tolerant fuel*, Journal of Nuclear Materials 540 (2020) 152355.

II. H. Liu, **D. R. Costa**, D. A. Lopes, A. Claisse, L. Messina, and P. Olsson, *Compatibility of UN with refractory metals (V, Nb, Ta, Cr, Mo and W): An ab initio approach to interface reactions and diffusion behavior*, Journal of Nuclear Materials 560 (2022) 153482.

III. **D. R. Costa**, H. Liu, D. A. Lopes, S. C. Middleburgh, J. Wallenius, and P. Olsson, *Interface interactions in UN-X-UO_2 systems (X = V, Nb, Ta, Cr, Mo, W) by pressure-assisted diffusion experiments at 1773 K*, Journal of Nuclear Materials 561 (2022) 153554.

IV. **D. R. Costa**, M. Hedberg, H. Liu, D. A. Lopes, S. C. Middleburgh, J. Wallenius, and P. Olsson, *Coated UN microspheres embedded in UO_2 matrix as an innovative advanced technology fuel: Early progress*, Proceedings in TopFuel 2021 - Water Reactor Fuel Performance, 24-28 October, Santander, Spain, ISBN: 978-92-95064-35-5.

V. **D. R. Costa**, M. Hedberg, D. A. Lopes, M. Delmas, S. C. Middleburgh, J. Wallenius, and P. Olsson, *Coated ZrN sphere-UO_2 composites as surrogates for UN-UO_2 accident tolerant fuels*, Journal of Nuclear Materials 567 (2022) 153845.

VI. **D. R. Costa**, M. Hedberg, D. A. Lopes, M. Delmas, S. C. Middleburgh, J. Wallenius, and P. Olsson, *Encapsulated additive nuclear fuels as an innovative accident tolerant fuel concept: fabrication, characterisation and oxidation resistance*, Manuscript in preparation.

VII. **D. R. Costa**, M. Hedberg, S. C. Middleburgh, J. Wallenius, P. Olsson, and D. A. Lopes, *Oxidation of UN/U_2N_3-UO_2 composites: an evaluation of UO_2 as an oxidation barrier for the nitride phases*, Journal of Nuclear Materials 544 (2021) 152700.

VIII. F. B. Sweidan, **D. R. Costa**, H. Liu, and P. Olsson, *Finite element modeling of UN-UO_2 and UN-X-UO_2 (X = Mo,W) composite nuclear fuels: temperature-dependent thermal conductivity and fuel performance*, Nuclear Materials and Energy JNME-D-22-00099R1 (2023) (Manuscript under review).

Author's contributions

The author has performed and participated in all experimental work of Papers I, III, IV, V, VI and VII, including UN powder synthesis, spark plasma sintering experiments, sample characterisation, data analysis, and has written the manuscripts. The author has not participated in the PVD coating and FIB analysis in PaperVI but visited the laboratories at SCK CEN, discussed the results, and wrote the manuscript. In Paper II, the author has not performed the DFT calculations but has written part of the introduction section, planned the modelling systems, discussed the results, and reviewed and edited the manuscript. In Paper VIII, the author has not performed the simulations but participated in the conceptualisation, data analysis, and reviewed and edited the manuscript.

Other publications not included in the thesis

IX. C. Ekberg, **D. R. Costa**, M. Hedberg, M. Jolkkonen, *Nitride fuel for Gen IV nuclear power systems*, Journal of Radioanalytical Nuclear Chemistry 318 (2018) 1713–1725.

X. A. C. de Freitas, **D. R. Costa**, P. M. Jardim, R. M. L. Neto, E. F. U. de Carvalho, M. Durazzo, *Effects of aluminum distearate addition on UO_2 sintering and microstructure*, Progress in Nuclear Energy 153 (2022) 104440.

XI. M. Lindroos, N. Vajragupta, J. Heikinheimo **D. R. Costa**, A. Biswas, T. Andersson, P. Olsson, *Micromechanical modeling of single crystal and polycrystalline UO_2 at elevated temperatures*, Journal of Nuclear Materials 573 (2023) 154127.

Acknowledgement

This section will be long due to the many great people and experiences I was fortunate to meet and have, but I encourage you to go through it until the end. There will be something special in Portuguese as well at the end (*terá algo especial escrito em Português também no final*)!

I start this section by thanking my dear supervisor, Pär Olsson, for trusting and encouraging me for almost five years. Without you, it would not be possible to do this PhD! I remember as it was today when I was waiting for you on the 9^{th} of July 2018 at around 9 a.m., outside the AlbaNova building, wearing a green T-shirt and extremely nervous. When I saw you, I said: "Wow, you are so young!". Your career achievements and progression inspire me and, I am sure, many others! I am very privileged to have you as my supervisor! I hope I have not disappointed you, as promised before starting the PhD.

I thank the Swedish Foundation for Strategic Research (SSF, *Stiftelsen för Strategisk Forskning*) for the financial support through project ID17-0078. Also, I thank Westinghouse Electric Sweden AB for hiring me as an industrial PhD student. I say that working at Westinghouse in Sweden is a dream that came true. I also thank you, Pontus Löf, for hiring me as a permanent employee within Westinghouse in the Process Development & Process Control (BQU) fabulous group! Great to be a part of such a skilled team!

Of course, many thanks to you, Magnus Limbäck, Simon Middleburgh, and Janne Wallenius, for agreeing to hire and supervise me during this life-changing journey! Many unforgettable moments together! Simon, it was a great experience to visit Bangor University and spend some days with you and your talented team there! Magnus, you are much more than a supervisor and manager; you are a friend that heard, helped, and encouraged me during these years. It is always fantastic to meet you at Westinghouse, have a coffee, and chat about professional and personal things. Janne, what a great learning experience to attend your courses! Great professor and professional!

Thank you, Mikael Jolkkonen, for teaching and supporting me with my lab activities! Great moments together! Also, thanks to Yulia, Elina, Faris and Sobhan, my lab colleagues, for the moments and activities together!

Special thanks to you, Denise Adorno Lopes! Everything started with you! You responded to that message, shared Pär's email, and encouraged me to apply for the

industrial PhD position. This moment was just the beginning of your outstanding contribution to my PhD project and, much more than that, to my personal life. You are a friend. You are an example of talent and success! Thank you very much, and let's continue doing fun things together!

Many others helped me during this journey. It would not be possible alone! Special thanks to you, Mirva Eriksson, for teaching me how to run the spark plasma sintering machine and for supporting me in many other things from the beginning to the end of my PhD. You were always willing to help! Many thanks to Gunilla Herting (KTH), Fredrik Gustavsson (SWERIM), and Joacim Hagström (SWERIM) for experimental support! To all of you at SCK CEN, who was essential to making the PVD coating work done! Specially, Rémi Delville, Daniel Penneman, Ann Leenaers and Marc Verwerft. Great collaboration! Amazing time together in Belgium! I am looking forward to what is coming next!

Thank you, Marcus Hedberg and Luis Gonzalez, for your vital support in fabricating the UN spheres. I will never forget those days in Gothenburg. Thank you very much, my friends! I am pleased and honoured to continue working with you, Luis, at Westinghouse!

A very special thank you to my dear friend, Ebrahim Mansouri. Since the first day I saw you in the meeting room in our corridor C3, I knew you were special. You taught me many things during our radiation damage and multiscale modelling courses. So simple for you, but very tough for me! I will never forget our conversations and moments together! I am sure our friendship will continue, independent of the circumstances!

I thank my dear friends at the Foursquare Gospel Church in Stockholm, especially Diogo & Vivi, Tiago & Lilian, Jamilton & Raquel, and pastors Levi & Mari. Your prayers, friendship, and hospitality were important for keeping me strong and progressing. Amazing moments together!

A bit of a "technical thanks" now: SEM-EDS maps of these almost five years show many Friend-rich regions in Brazil and Sweden. Moreover, high-resolution and well-spread Collaboration-rich phases are present in Europe and the UK. In Europe, the Sweden-rich spots contain Stockholm (KTH and Stockholm University), Gothenburg (Chalmers University of Technology), Uppsala (Uppsala University), Linköping (Linkping University) and Jönköping (Jönköping University) phases. Additionally, the Finland-rich area is identified as VTT Technical Research Centre (*Valtion teknillinen tutkimuskeskus*), and the Belgium-rich region is composed of the Belgian Nuclear Research Centre (SCK CEN, *Studiecentrum voor Kernenergie / Centre d'Etude de l'Energie Nucléaire*). In the UK, the EDS maps show high concentrations at Bangor University and Archer Technicoat Ltd. (ATL Advanced Coating Solutions). Quantitative measurements using WDS demonstrate that those regions well-represented all support received during this PhD project. The FIB cross-sections of all Friend- and Collaboration-rich phases confirm that the bulk structures are identical to the regular cross-section observations. The EBSD examinations show that all phases have a strong preferential grain orientation towards the (collaboration, results, success) direction. Finally, the XRD

data confirm that all regions are pure and crystalline Friendship and Collaboration phases. Therefore, these results prove that a hard and challenging PhD project is done when many Friend- and Collaboration-rich phases are present in our lives!

I separate this moment to thank my Lord and Saviour, Jesus Christ (John 3:16). I am grateful to my family in Brazil, Mom and Dad, brothers, and sister. It was tough to move to Sweden and leave you all there... You know that. But your support and encouragement helped me to move and achieve my dreams. I love you all very much! Please, allow me to say these words in Portuguese so that they will comprehend. *Eu separo este momento para agradecer a Jesus Cristo, meu Senhor e Salvador (João 3:16). Eu sou muito grato à minha família no Brasil, mãe e pai, irmãos e irmã. Foi muito difícil mudar para a Suécia e deixar vocês lá... Vocês sabem disso. Mas o apoio e encorajamento de vocês me ajudaram a mudar e a alcançar meus sonhos. Eu amo muito todos vocês!.*

What is the most important thing for me on Earth? The answer is straightforward: my lovely wife, Daniela, and daughter, Larissa. Always with me. Always supporting me. Always crying and laughing with me. Dani and Larissa, even if I had all friendship and collaboration mentioned here, it would never be possible to move to Sweden and do this PhD without your love, care, and support! Many tough moments, but many brilliant ones as well! I love you two from the bottom of my heart! Unconditionally!

Lastly and with the same importance, I would like to thank you. Yes, you who are reading this section right now. As I mentioned at the beginning, here is a special moment for me. My life was never easy. I was born and raised in a slum (*favela*) in Rio de Janeiro, Brazil, called "Morro da Formiga". My parents had to work very hard to take care of the family. I studied at public schools my whole life, which are (unfortunately) not good in Brazil. But I believed I could do something different even if the circumstances around me were telling otherwise. I believed If I studied hard, I could get a bachelor´s degree in engineering from a public University (they are very good and hard-to-enter universities in Brazil); and I did. I believed I could get a master's degree from the best University in Brazil; and I did. I believed I could get a PhD degree abroad from an outstanding institution... Now I'm here, writing this section, about to defend my PhD thesis and get a PhD degree from an outstanding institution (KTH Royal Institute of Technology), about to achieve what most people said would be impossible for a person who was born and raised where I was. Final and very important message: I encourage you to keep on working to achieve your dreams. Do not give up! If I could do and achieve all those things, you can as well! Share the message! Support those who are in need! Spread love! Next, I will write this paragraph in Portuguese because I will share this thesis with as many people as possible there in Brazil, who may not understand the content and probably will not be interested in what I did in my research. But maybe they will be inspired and encouraged to change their lives and achieve whatever they dream of! It is possible, indeed!

Por último, mas com a mesma importância, eu gostaria de agradecer a você. Sim, você que está lendo esta seção agora. Conforme eu mencionei no início, este

é um momento especial para mim. Minha vida nunca foi fácil. Eu nasci e cresci em uma favela no Rio de Janeiro, Brasil, chamada Morro da Formiga. Meus pais tiveram que trabalhar duro para cuidar da família. Eu estudei a minha vida inteira em escolas públicas, que não são (infelizmente) boas no Brasil. Mas eu acreditei que eu poderia fazer algo diferente mesmo com as circunstâncias ao meu redor dizendo o contrário. Eu acreditei que se eu estudasse bastante, eu poderia obter um título de engenheiro por uma universidade pública; e eu consegui. Eu acreditei que eu poderia obter um título de mestre em ciências pela melhor universidade do Brasil; e eu consegui. Eu acreditei que eu poderia obter um título de PhD por uma fantástica instituição... Agora eu estou aqui, escrevendo esta seção, próximo de defender minha tese e obter o título de PhD por uma fantástica instituição (KTH Instituto Real de Tecnologia), próximo de alcançar o que a maioria das pessoas diziam que seria impossível para uma pessoa que nasceu e cresceu no lugar onde nasci e cresci. Mensagem final e muito importante: eu encorajo você a continuar trabalhando para alcançar seus sonhos. Não desista! Se eu consegui alcançar todas essas coisas, você também pode! Compartilhe esta mensagem! Ajude aqueles que precisam! Espalhe amor! Eu escrevi esta mensagem em português pensando em você, que provavelmente não estará muito interessado no que eu fiz no PhD, ou de repente não entenderá muita coisa que está na tese. Mas, talvez, você será inspirado e encorajado a mudar sua vida e alcançar aquilo que você tem sonhado! É possível, verdadeiramente!

Acronyms

ATF	Accident tolerant fuel
BSE	Backscattered electron
BWR	Boiling water reactor
CVD	Chemical vapour deposition
DBA	Design basis accident
DEC	Design extension condition
DFT	Density functional theory
DSC	Differential scanning calorimetry
EBSD	Electron backscatter diffraction
EDS	Energy-dispersive X-ray spectroscopy
EPMA	Electron probe microanalysis
FC	Fast cooling
FEM	Finite element modelling
FIB	Focused ion beam
LOCA	Loss-of-coolant accident
LWR	Light water reactor
MAUD	Materials analysis using diffraction
MRT	Maximum reaction temperature
OOT	Oxidation onset temperature
PCI	Pellet-cladding interaction
PVD	Physical vapour deposition
PWR	Pressurised water reactor
SC	Slow cooling
SCC	Stress corrosion cracking
SCK CEN	Belgian Nuclear Research Centre
SE	Secondary electron
SEM	Scanning electron microscopy
SPS	Spark plasma sintering
SS	Steel sphere
TD	Theoretical density
TG	Thermogravimetry
TGA	Thermogravimetric analysis
WDS	Wavelength-dispersive X-ray spectroscopy
XRD	X-ray diffraction

Contents

List of Figures

List of Tables

Chapter 1

Introduction

Electricity is vital to several parts of life in modern societies and will become even more crucial with the expansion of industrialisation, transport, and heating systems. However, CO_2 emissions due to electricity production are a major cause of global warming. Since reliable, efficient, clean, and sustainable energy systems are necessary to overcome environmental issues, nuclear energy occupies a strategic and promising position. Unfortunately, the risks of nuclear accidents, such as the Fukushima Daiichi disaster in Japan, in 2021, generate opposition to the nuclear application. As a prompt response to this unprecedented disaster, the nuclear community introduced the concept and proposed developments in the so-called accident tolerant fuels (ATFs). The ATFs are designed to endure a severe accident in the reactor core longer than the standard UO_2-Zr alloy systems used in light water reactors (LWRs). Recent studies demonstrate that ATFs, including U_3Si_2 and UN, are essential contributors to enhancing the safety, competitiveness, and economics of nuclear power plants. However, the low oxidation resistance of these fuels limits their application in LWRs. This research aims to fabricate, characterise, and evaluate an innovative ATF concept for LWRs: encapsulated UN spheres as additives for the standard UO_2 fuel. This introductory chapter will provide the background and context of the thesis topic, followed by the research advancements on ATFs focusing on UN-UO_2 composites and their research challenges, as well as the thesis objectives, significance, and limitations. Finally, the outline will present the structure of this thesis.

1.1 Contextualisation

Fast global industrialisation and a constantly growing population demand a proportional increase in electricity production and consumption. Unfortunately, electricity production over the years has affected the climate and caused a significant impact on the environment around the world due to greenhouse gas emissions [1]. Around two-thirds of these emissions are due to the combustion of fossil fuels to produce

electrical energy [2]. It is estimated that the world reached a new all-time high of approximately 13.2 Gt CO_2 in power sector emissions in 2022, primarily owing to growth in fossil-fired generation in the Asia Pacific, Europe, and Eurasia [2]. This scenario may worsen if no actions are taken since the electricity consumption is expected to double by 2050 [3]. What is urgently needed to overcome the high emissions of greenhouse gases and reduce the effects of global warming? Reliable, efficient, clean, and sustainable energy systems are vital to address this question. The current energy crisis caused by the shortage of natural gas from Russia is an unfortunate example that the energy system cannot depend on the gas industry and rely upon renewable energy only.

Renewable energy sources such as wind and solar have increased considerably in the past decade. However, renewable sources alone are not enough to supply the current demand of electric consumption, and they strongly depend on variables and uncertainties in nature [4]. Conversely, nuclear energy is a sustainable, reliable, and carbon-free energy source. Over the past five decades, its application has reduced CO_2 emissions by over 60 gigatonnes, which corresponds to approximately two years' worth of global energy-related emissions [5]. Therefore, the increasing demand for clean, sustainable, reliable, and carbon-free energy sources puts nuclear energy in a strategic position.

At the end of 2021, 437 nuclear reactors were operational worldwide, and these supplied approximately 10 % of the world's electricity needs of that year. Additionally, 56 reactors were under construction in 19 countries [6]. Nevertheless, the expansion of nuclear power plants faces public opposition and public concerns. Furthermore, the current war in Ukraine is an unfortunate example that nuclear power is used to threaten and create panic in the world. Risks of nuclear accidents are also included as the main arguments by people opposed to nuclear application.

Most of the nuclear reactors operate with uranium dioxide (UO_2) and zirconium-based alloys as the fuel-cladding systems in LWRs [7]. Within LWRs, the current standard reactors are boiling water reactors (BWRs) and pressurised water reactors (PWRs) with UO_2 enriched to approximately 4 to 5 wt% in the fissile ^{235}U isotope.

Inside an LWR core, the UO_2 fuel is bombarded with neutrons. The ^{235}U isotope absorbs these neutrons and splits into two or more fission products, releasing a large amount of energy and more neutrons to sustain the chain reaction. Part of this energy is transferred to the coolant water, which has a crucial role in the reactor core.

In BWRs, the water is heated to its boiling point at about 75 bar to produce steam ($\sim$560 K) inside the reactor vessel. This generated steam is fed through pipes directly into a turbine to produce electricity. Afterwards, the water cycles back to the reactor core and is reheated by the fission reactions, repeating the process. In PWRs, the water is pressurised to considerably higher pressures (150-160 bar) to maintain its liquid form at high temperatures (600-623 K). This hot and pressurised coolant water is pumped into tubes inside a heat exchanger to create steam in a separate water source. Steam at about 60 bar and 550 K is then directed to a turbine to produce electricity. Unused steam is condensed back to water and

reused in the steam generation process.

The loss of the coolant water in LWRs constitutes an undesired and severe accident scenario, namely loss-of-coolant accident (LOCA). This type of accident occurred in Japan after the tsunami, which originated from the Tōhoku earthquake, hit the Fukushima Daiichi power plant in 2011 and caused a station blackout (SBO). All cooling systems and backup generators were compromised, eventually leading to fuel overheating and melting. This meltdown caused hydrogen production from the reaction between the zirconium fuel cladding and superheated steam, followed by a hydrogen accumulation and explosion in the upper part of the reactor building [8]. Responding to this unprecedented disaster, the international nuclear community has striven to engineer a successor to the current UO_2–Zr fuel-cladding systems. Since then, many studies have been aiming to improve the passive safety of the nuclear fuel system by using accident tolerant fuel (ATF) materials. These new fuel concepts have to maintain or enhance fuel performance under normal and transient operating conditions, as well as during a potential design basis accident (DBA) and design extension condition (DEC) [9].

1.2 Accident tolerant fuels

An accident tolerant fuel is defined as a material that can withstand a severe accident in the reactor core for a longer period than the standard UO_2-Zr alloy systems, whilst maintaining or enhancing the fuel performance under normal operation and operational transients. Some requirements for commercialisation of such fuels include [9]: (i) compatibility with the existing and future fuel systems in LWRs; (ii) maintain or extend operating cycles, reactor power output and reactor control; (iii) meets or exceeds current fuel system performance under normal and accident scenarios; (iv) adhere to fuel fabrication and operating plant regulations and policies; and (v) cannot degrade the transport, storage or repository performance of the fuel, possibly considering use within a closed fuel cycle.

There are specific requirements regarding the properties, behaviours, and performance of ATF cladding, ATF fuel, and the combined fuel-cladding systems. The cladding must confine the fissile fuel and fission products inside the fuel rod while having high thermal conductivity, melting temperature, ductility, and strength. Additionally, being corrosion-resistant, chemically compatible with the fuel, and sufficiently neutron transparent. The fuel candidates must have a high melting temperature, high thermal conductivity and density, low specific heat capacity and low coefficient of thermal expansion. Moreover, the materials must be chemically stable against the cladding and fission products, and be corrosion-resistant when in contact with the coolant water.

A variety of ATF fuel materials have been proposed to substitute the standard UO_2 fuel in LWRs, including uranium silicide (U_3Si_2) [10–13], uranium nitride (UN) [14–18], UN-U_3Si_2 composites [19–21] and UO_2-X composites (X=BeO [22], SiC [23], Mo [24], Cr_2O_3 [25], diamond [26], UB_2 [27]). Mainly, these fuels have a

high melting point, uranium density, and thermal conductivity. Table 1.1 presents some thermophysical properties of UO_2 and the principal ATF fuel candidates (U_3Si_2 and UN). Both silicide and nitride fuels have greater uranium density and thermal conductivity in comparison with UO_2. However, their major drawback is the low oxidation resistance when in contact with the coolant water and steam in LWRs [28–35].

Table 1.1: Thermophysical properties of UO_2 and ATF fuel candidates.

Properties	**UO_2**	**U_3Si_2**	**UN**
Melting temperature (K)	3147 [36]	1938 [37]	3120 [38]
Theoretical density (g/cm^3)	10.96 [39]	12.20 [40]	14.32 [39]
Uranium density (g/cm^3)	9.66	11.31	13.51
Thermal conductivity (W/m.K)*	6.0-2.5 [41]	15.0-27.0 [10]	19.0-25.0 [42]

*As a function of temperature of pristine fuels. .

The lower melting temperature and density of U_3Si_2 put UN in a prominent position. Nevertheless, the low oxidation resistance of UN continues to be a challenge to be addressed. To overcome this issue, UN-based composite fuels have been proposed to protect the nitride fuel against oxidation in an accident scenario. The central idea of such composites is to add a compound that acts as a protective barrier against UN oxidation. Some materials, including Cr [43–45], CrN [43, 44], AlN [43, 44, 46], CrN-AlN [43, 44], U_3Si_2 [19–21] and UO_2 [47–49], have already been studied for this purpose. Amongst them, the UO_2 fuel can be considered a promising candidate because of its widespread use as a standard nuclear fuel in LWRs, and its chemical and structural stability against water, fission products and cladding materials [50–52]. Thus, UN-UO_2 composites can benefit from the best properties of both fuels: the high uranium density and thermal conductivity of UN and the chemical stability of UO_2.

1.3 UN-UO_2 composite fuels

UN-UO_2 ATF composites are proposed to resolve the low oxidation resistance of UN while increasing the uranium density and thermal conductivity of the final fuel pellet. The first studies addressing this ATF composite concept were published in 2015. Yang et al. [47] used hot press sintering (1573-1863 K, vacuum) to fabricate UN(30–70 wt%)-UO_2 composites, using a UN powder synthesised by hydriding and then nitriding spherical U metal powders. The addition of 70 wt% UN increased the uranium density of UN-UO_2 by 13% (10.91 g/cm^3) and the thermal conductivity up to 100% (8.16 W/m.K at 1073 K), when compared to pure UO_2. Moreover, the authors observed by XRD analyses the formation of a third phase, α-U_2N_3 (sesquinitride), and suggested that it might originate from the $U(ON)_{2-x}$ type oxynitride phase during cooling. Similarly, Jaques et al. [48] identified a third phase after sin-

tering UN-UO_2 composites and attributed it to a hyper-stoichiometric nitride phase or a uranium oxynitride phase. The authors likewise used a UN powder synthesised by hydriding and nitriding spherical U metal particles to fabricate the composites by conventional sintering (1973-2273 K, Ar and Ar/N_2, 5 h). Malkki [53], also in 2015, observed the formation of α-U_2N_3 in UN pellet, specifically in the UO_2 inclusions (impurity). The explanations were based on an incomplete denitriding of α-U_2N_3 to UN powder during synthesis or diffusion of O impurity into UN bulk by substituting N atoms.

Three years later, Mishchenko [49] reported a secondary nitride phase in the UO_2 matrix after sintering UN-UO_2 composites. Dense UN pellets were crushed, sieved into two different particle size distributions (125-335 µm and 335-1000 µm), mixed with stoichiometric UO_2 powder, and then sintered at 1673 K and 1873 K using the spark plasma sintering (SPS) method in vacuum. Nitrogen was very mobile in the UO_2 matrix, forming a secondary nitride phase in the UO_2 matrix. After annealing experiments (1873 K, 20 h, Ar), the author identified the α-U_2N_3 phase and proposed that its formation occurs during the cooling stage when the temperature drops to approximately 1073 K. Later in 2019, Shivprasad et al. [54] presented isothermal corrosion studies of UN(5-30 vol%)-UO_2 composite fuels at 623 K, under 82 % steam for 12 h. The results show that the UO_2 fuel significantly delayed the oxidation onset temperature of UN in the UN-UO_2 composites.

The presented literature demonstrates that UN-UO_2 composites are potential ATF candidates in LWRs because of the improvements in the oxidation resistance of UN [54], as well as the enhancements in both the uranium density [47–49] and thermal conductivity [47] of the final fuel pellet. A fuel with such advancements may operate with a lower centreline temperature, which increases the margin to melting and thus improves the operating safety margins while decreasing the fission gas release and extending the fuel resident time [55–58]. These combined beneficial properties evidence the UN-UO_2 composites as promising ATF fuel candidates. However, the complex interaction between UN and UO_2 during sintering is a relevant issue to be understood. Yet, the knowledge about the formation mechanism of the α-U_2N_3 phase is limited, divergent, and does not address its physical localisation in the UN-UO_2 microstructure in detail. This sesquinitride is detrimental to fuel performance since it can dissociate into UN and N_2 upon heating in operating conditions, which would increase the fuel pin pressure (causing cladding embrittlement) and cause additional cracks in the fuel at high temperatures under irradiation [59]. Therefore, advanced fabrication, characterisation, and evaluation processes are necessary to manufacture dense and oxidation-resistant UN-UO_2 fuel pellets without the α-U_2N_3 phase.

1.4 Thesis objectives

Given the potential application and lack of understanding of UN-UO_2 composites, this study will aim at developing and evaluating an innovative ATF concept

for LWRs: encapsulated UN spheres as additives to the standard UO_2 fuel. The research objectives that will fit the thesis aim are:

- To understand the formation mechanism of the α-U_2N_3 phase.

- To study and propose potential coating candidates to protect the UN spheres against interaction with UO_2 during fabrication.

- To develop and study the feasibility of different coating methodologies by using surrogate spheres for the UN spheres: powder coatings, chemical vapour deposition (CVD) and physical vapour deposition (PVD).

- To encapsulate the UN spheres, sinter the composites by SPS, and characterise the fuel pellets using complementary techniques.

- To evaluate the oxidation resistance of the composite fuels, and compare their behaviours with UO_2 and UN references.

- To estimate the thermal behaviour of uncoated and encapsulated UN-UO_2 composites as a function of the weight fractions of UN, coating materials, and thicknesses.

This study will contribute to the nuclear community on skills development by incorporating methodologies for fabricating, characterising, and evaluating accident tolerant fuels within LWRs. Thus, it will help address the current demand for research in this area and provide real-world value to fuel manufacturers and, consequently, the society in such advanced fuel design. This study will limit its application to coating materials within the family of refractory metals, not intending to study different materials, alloys or multilayered structures. Furthermore, not all possible coating techniques are explored due to limited time and resources. Also, the developments involving the fabrication of high-density UN spheres (>95 %TD) are not considered in this thesis.

1.5 Thesis structure

The thesis is based on Papers I to VIII and will be organised into four Chapters, including the Introduction, Methodology, Results, and Conclusions and outlook. These Chapters provide the reader with a roadmap of the research development to achieve the objectives of this thesis. Fig. 1.1 schematically illustrates the main steps to develop and evaluate encapsulated UN-UO_2 accident tolerant fuel.

In Chapter 1, the background and context of the thesis has been introduced. The research aim and objectives have been identified, and the significance and value of such research are argued for. Limitations of the study have also been discussed.

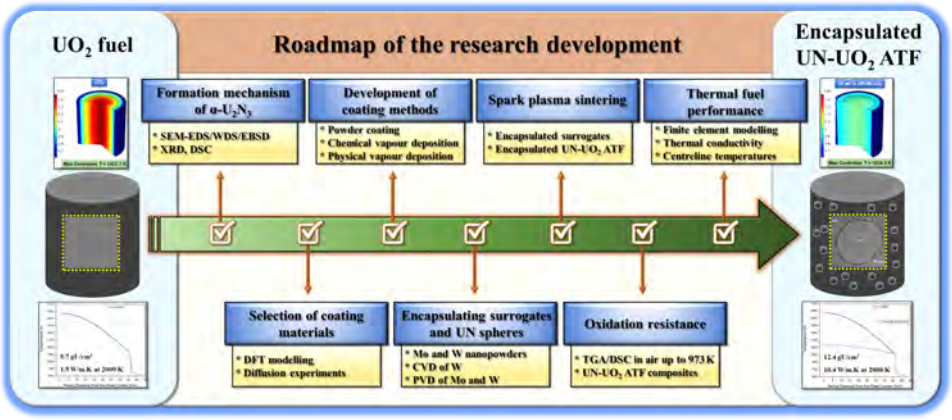

Figure 1.1: Roadmap of the research development.

In Chapter 2, the methodology will be presented. The raw materials and processes used to fabricate all sintered materials will be described, including the techniques to characterise and evaluate the ATF composites. Limitations of the methodology will also be discussed.

In Chapter 3, the results will be reported and discussed as follow:

1) The studies involving the uncoated UN-UO_2 composites, including the formation mechanism of α-U_2N_3 and the influence of the main sintering parameters on its amount, morphology, and crystalline orientation in the UO_2 matrix (Paper I).

2) The evaluation of potential coating candidates within the refractory metals group, using both modelling and experiments, to identify the most promising candidates (Papers II and III).

3) The coating techniques used to encapsulate the UN spheres, including development processes using ZrN and steel spheres as surrogates for UN spheres (Papers IV, V and VI).

4) The studies involving the encapsulated UN-UO_2 accident tolerant fuels, including the fabrication by SPS and characterisation by complementary techniques (Papers IV and VI).

5) The oxidation resistance of the uncoated UN-UO_2 composites, including a proposed mechanism for the fuel oxidation in air up to 973 K (Paper VII).

6) The thermal behaviour of the uncoated and encapsulated composites, including the influence of the amount of UN spheres, coating materials and thicknesses on thermal conductivity and operating fuel centreline temperature in a simulated fuel pin (Paper VIII).

In Chapter 4, the conclusions and outlook will summarise the achievements of this thesis and propose future works in the ATF field.

Chapter 2

Methodology

This chapter will detail the different materials, experiments and characterisation techniques used in this thesis to develop and evaluate encapsulated UN-UO_2 accident tolerant fuel. First, the raw materials will be described, followed by the coating methods, spark plasma sintering experiments, composite fuels evaluations, and characterisation techniques. Main methodological limitations will also be described and discussed in this section.

2.1 Raw materials

The uranium dioxide (UO_2) powder used in this study was supplied by Westinghouse Electric Sweden AB, and was reported to have an O/U ratio of 2.13, apparent density of 2.19 g/cm^3, specific surface area of 5.33 m^2/g, mean particle size of 20.20 μm, and 900 ppm of H_2O as the main contaminant. Fig. 2.1 shows the morphology of the as-received powder, characteristic of the industrial ammonium uranium carbonate (AUC) wet route [60]. More details regarding powder morphology and crystalline structure are presented in Papers I and VII.

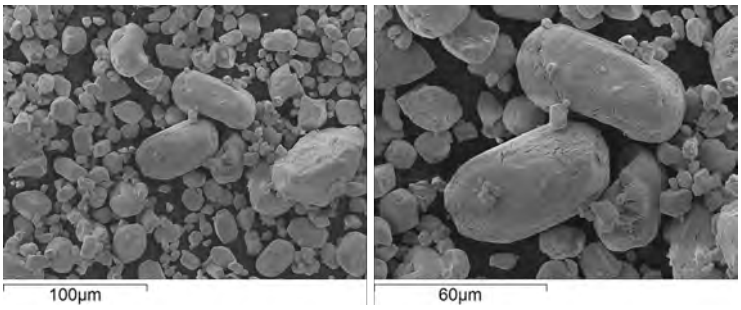

Figure 2.1: Morphology of the $UO_{2.13}$ powder supplied by Westinghouse Electric Sweden AB.

The zirconium nitride (ZrN) and uranium nitride (UN) spheres were fabricated at Chalmers University of Technology by an internal sol-gel method consisting of three main processes: internal gelation, reduction to oxide, and nitridation [61,62], as schematised in the twelve steps in Fig. 2.2.

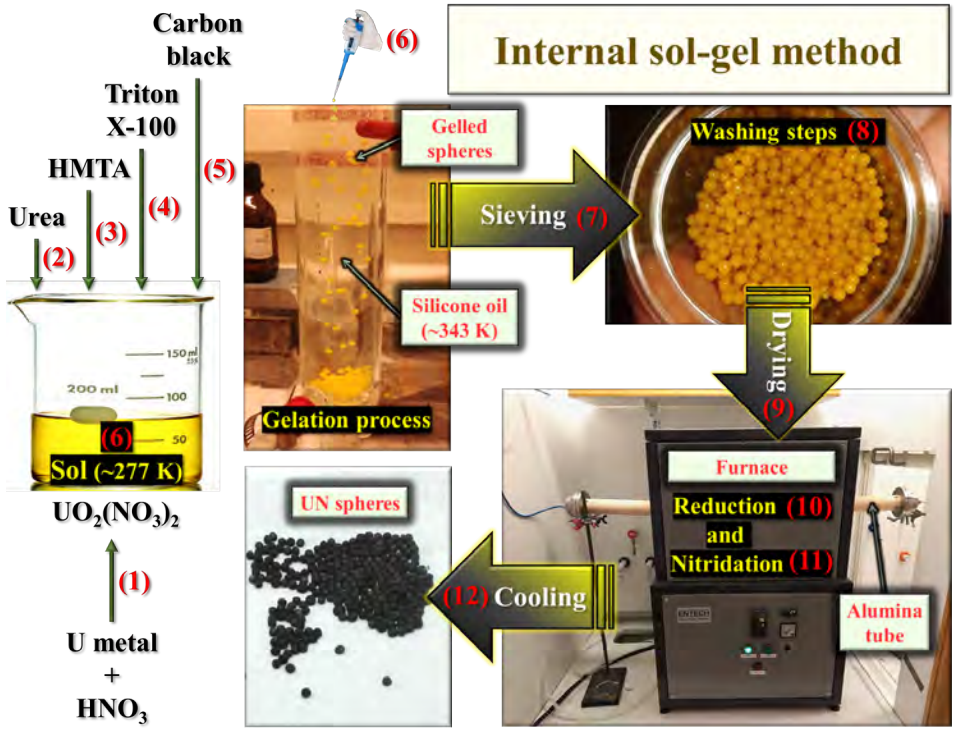

Figure 2.2: Schematic illustration of an internal sol-gel method adopted to fabricate UN spheres [61], (Papers I and VI). More details for ZrN spheres fabrication are found in [62].

In summary, depleted uranium metal was dissolved in nitric acid (HNO_3, 67 %, Merck) to obtain the precursor solution of uranyl nitrate ($UO_2(NO_3)_2$). This solution was kept under magnetic stirring at approximately 277 K. Then, urea (Sigma Aldrich, solid form) was added to obtain a urea/metal molar ratio of 1.3. After its dissolution, HTMA (hexamethylenetetramine, Sigma Aldrich) was gradually added to guarantee its complete dissolution and an HMTA/metal molar ratio of 1.7. Afterwards, Triton X-100 (carbon dispersion agent, Sigma Aldrich) was poured into the solution to a concentration of 0.02 g/mL. Finally, carbon black (Supelco, ~200 nm in particle diameter) was added to reach a C/metal molar ratio of 2.5, followed by an extra 10 min of stirring before the gelation step. The final solution was manually pipetted in the gelation column filled with silicone oil (Rhodorsil, oil

47) at about 343 K. Then, the gelled spheres ($UO_3.H_2O$) were sieved and washed twice with petroleum ether, and then once with ammonium hydroxide and water to leach all unreacted chemicals. Lastly, the gelled spheres dried overnight in air at room temperature.

To obtain the UN spheres, the gelled and dried samples were reduced and nitrided in the furnace to temperatures above 1773 K in a H_2/N_2 atmosphere followed by cooling. More details about these steps for the UN spheres are found in [61] and Papers I and VI. For the ZrN spheres, the operational details are in [62] and Paper V. The as-synthesised ZrN and UN spheres are represented in Fig. 2.3. In general, the spheres were porous (50-75 %TD) with diameters between 800 μm and 1100 μm. Papers I and VI detail the morphology, crystalline structure and fabrication processes for the UN spheres, and Paper V for the ZrN spheres.

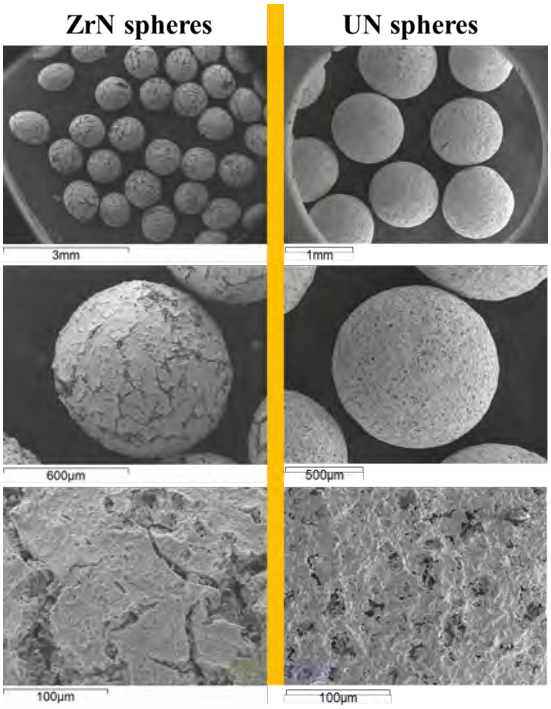

Figure 2.3: Morphology of the as-fabricated ZrN and UN spheres.

UN powder was synthesised by a hydriding-nitriding-denitriding route [61] at the Nuclear Fuel Laboratory at KTH. Fig. 2.4 pictures the UN fabrication facility, which is mainly composed of a furnace, a controller, gas suppliers, flow meters, and a gas mixer. Uranium metal was loaded in a quartz tube and heated in H_2 to obtain uranium hydride (UH_3), followed by the nitriding process at 773 K and denitriding at 1423 K, as detailed in Fig. 2.5. After cooling in argon, the UN

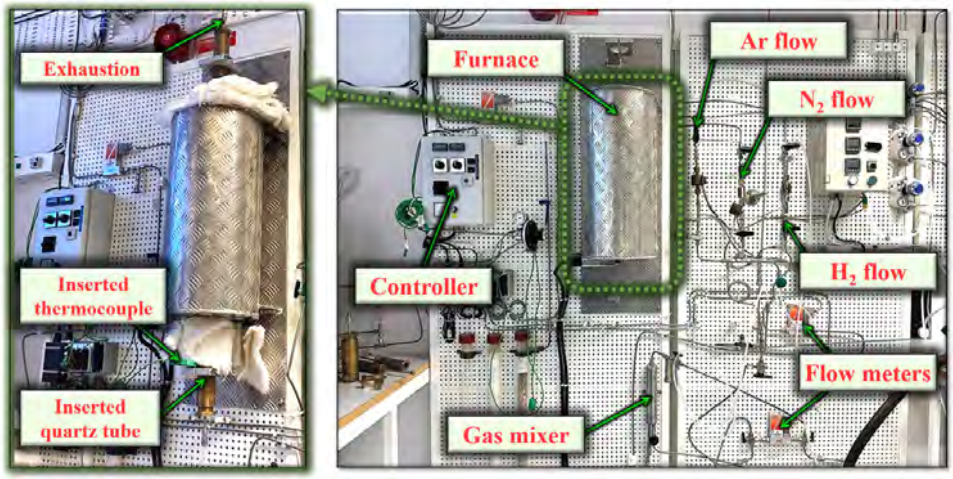

Figure 2.4: UN powder fabrication facility at the Nuclear Fuel Laboratory at KTH.

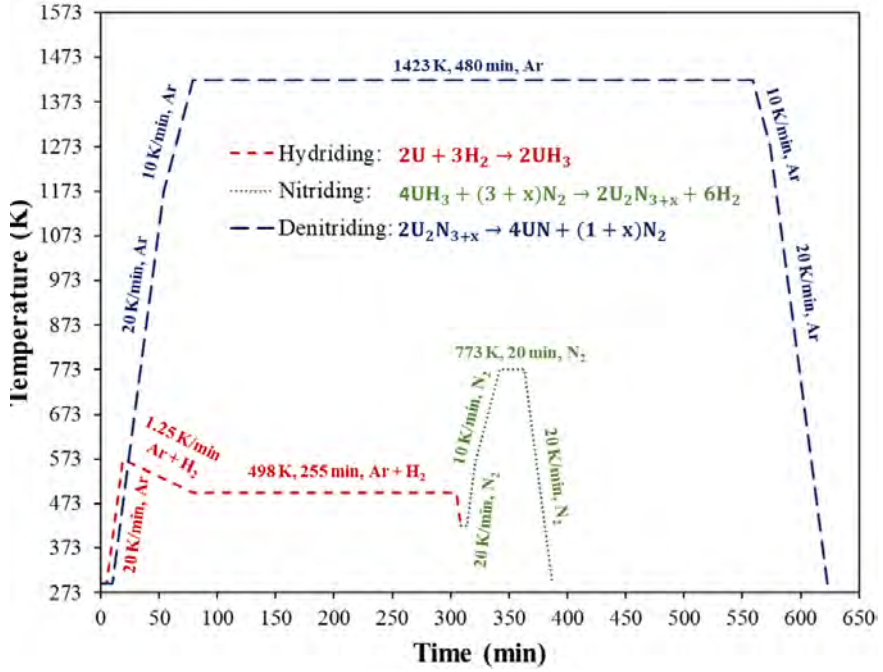

Figure 2.5: Thermal profiles used in the hydriding (red), nitriding (green), and denitriding (blue) processes [61]. Argon was used during the denitriding process to avoid U_2N_3 formation.

powder was collected and characterised. Fig. 2.6 shows its flaky morphology with particle sizes varying from ∼3 μm to large agglomerates (>100 μm), as previously observed [16,34]. Oxygen and nitrogen contents were about 1550 ppm and 5.4 wt%, respectively. Additional detail regarding powder morphology and crystalline structure are described in Paper III.

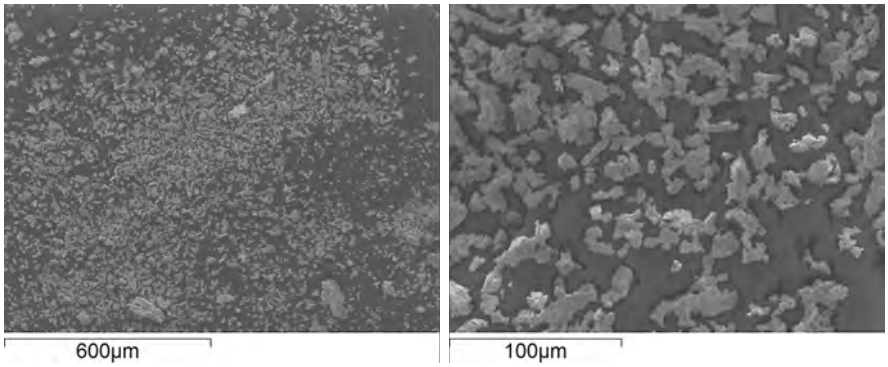

Figure 2.6: Morphology of the as-fabricated UN powder showing a flaky morphology with particle sizes varying from ∼3 μm to large agglomerates (>100 μm).

2.2 Coating methods

Coating technology is rapidly progressing to keep pace with the current demand for advanced materials applications. Conventional methods, such as physical and chemical vapour depositions, are also being adapted to produce coating structures with improved performance and properties not achievable before. Moreover, new processes are being developed to achieve new compositions and enhanced physical properties [63].

Different coating methods were used in this thesis, including the developed powder coatings, chemical vapour deposition (CVD), and physical vapour deposition (PVD). As mentioned, this thesis is limited to these techniques and does not consider all possible coating techniques available due to time, logistics, and budget constraints.

Table 2.1 presents the identification of the encapsulated spheres based on the coating materials, coating methods, type of spheres, and appearance in the papers included in this thesis. The following sections describe the details regarding the methodology and limitations of the powder, CVD and PVD coating methods, respectively.

Table 2.1: Encapsulated spheres and their appearance in the papers included in the thesis.

Sample	**Metal**	**Coating method**	**Spheres**	Paper
Mo(wet)/ZrN	Molybdenum	Powder (wet)	ZrN	IV, V
Mo(binder)/ZrN	Molybdenum	Powder (binder)	ZrN	V
W(binder)/ZrN	Tungsten	Powder (binder)	ZrN	V
Mo(nano)/UN	Molybdenum	Powder (binder)	UN	VI
W(nano)/UN	Tungsten	Powder (binder)	UN	VI
W(CVD)/ZrN	Tungsten	CVD	ZrN	V
Mo(PVD)/SS	Molybdenum	PVD	Steel	VI
W(PVD)/SS	Tungsten	PVD	Steel	VI
Mo(PVD)/UN	Molybdenum	PVD	UN	VI

2.2.1 Powder coating

Powder coating is demonstrated to be an inexpensive, simple, and quick method to encapsulate particles in a matrix [64, 65]. In this thesis, molybdenum (99.9 %) or tungsten nanopowders (99.95 %) (US Research Nanomaterials, Inc.) were used to encapsulate ZrN (surrogate) and UN spheres. Fig. 2.7 shows the morphologies of the powders, with Mo having spherical particles (25-90 nm) and small agglomerates (200-1200 μm), and W with elongated particles (∼150x60 nm) and larger agglomerates (∼3000 μm).

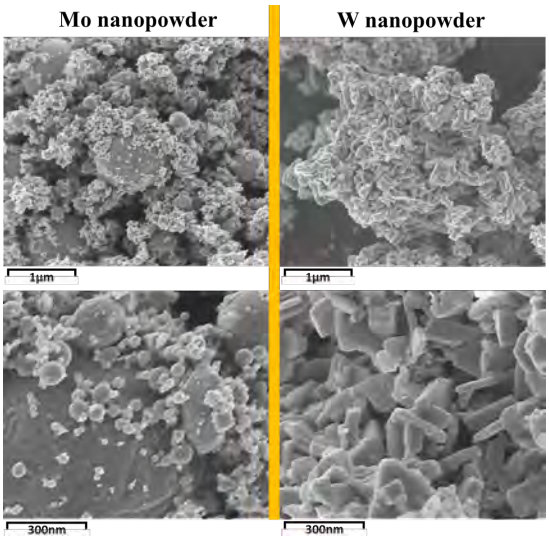

Figure 2.7: SEM-SE images of Mo and W nanopowder morphologies.

Two powder coating methods were developed: wet and binder, as schematised in Fig. 2.8 and Fig. 2.9, respectively. The wet method consisted of using acetone under 30 min of magnetic stirring to disperse nanopowders. Then, about 10 mL of this suspension was transferred to another container and mixed with spheres. After drying the acetone in air, the encapsulated spheres were placed in a quartz boat and loaded into a quartz tube inserted in a horizontal furnace. The encapsulated samples were heat treated at 1373 K for 1 h in argon to improve the contact between powder-powder particles and layers-substrates (pre-sintering step). More details regarding the development and procedures are found in Papers IV and V.

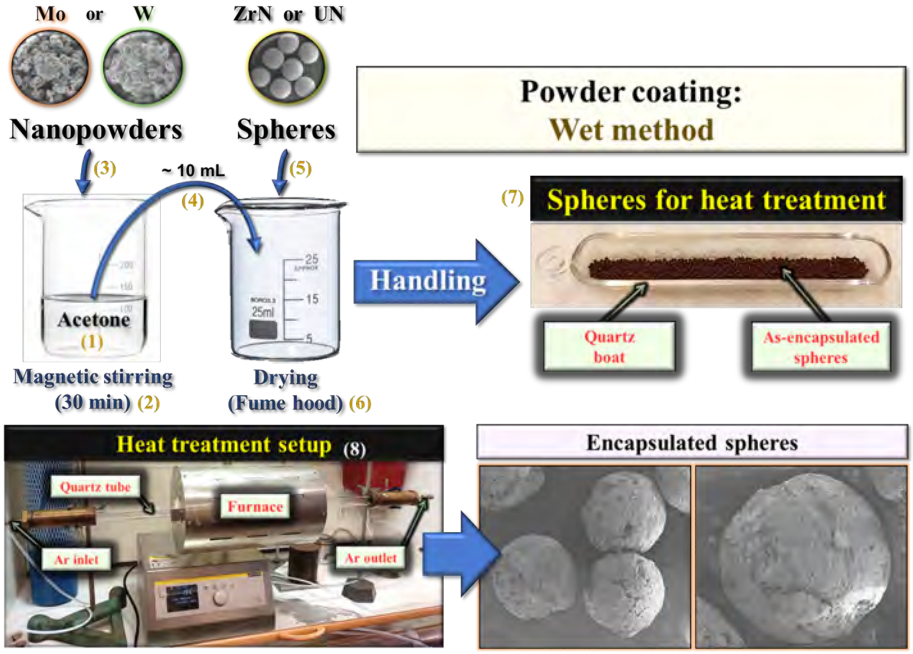

Figure 2.8: Schematic representation of the developed wet coating method. The as-encapsulated spheres were heat treated at 1373 K for 1 h in argon.

The binder method consisted of using a binder agent (Shell Omala S2 G320) to improve the adherence of Mo and W nanopowders onto the spheres (Fig. 2.9). It is demonstrated in Paper IV that W nanopowder has not adhered well to the spheres using the wet method. In the binder procedure, the spheres and binder were mixed using a small beaker (25 mL) and spatula, and sieved out to remove the excess binder. After the addition of Mo or W nanopowders, the beaker was rotated to guarantee powder-sphere contact. The as-encapsulated samples were also heat treated at 1373 K for 1 h in argon to pre-sinter the coating layer, as well as to eliminate the organic binder at moderate temperatures (> 773 K). More details of these procedures are described in Papers IV and V.

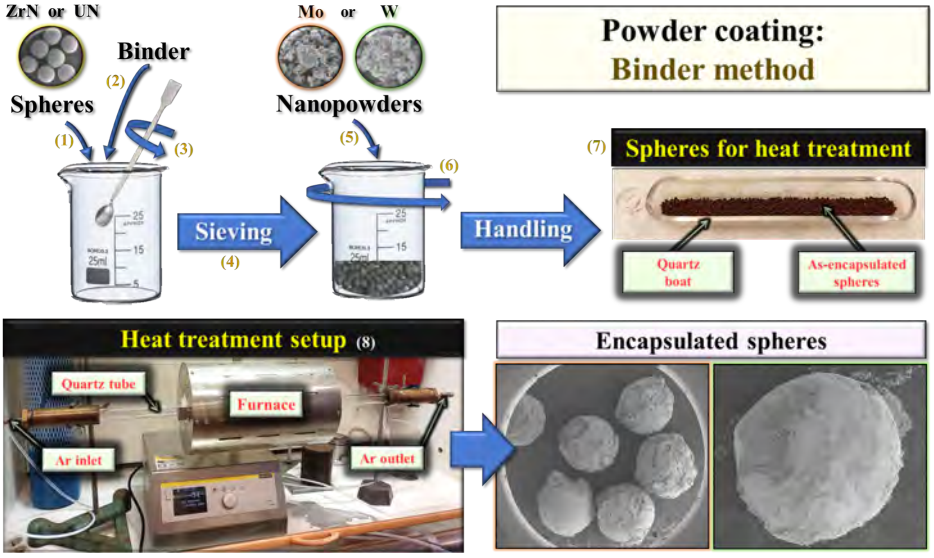

Figure 2.9: Schematic representation of the developed binder coating method. The as-encapsulated spheres were heat treated at 1373 K for 1 h in argon.

2.2.2 Chemical vapour deposition

Chemical vapour deposition (CVD) is employed in several coating applications, including conductors, passivation layers, oxidation barriers, corrosion-resistant coatings, and more [63]. In CVD processes, gaseous reactants are fed into a reactor with a substrate at a specific temperature. On a substrate surface and its vicinity, a chemical reaction produces a solid material that is deposited onto a substrate's surface. In this thesis, the CVD of W was used to encapsulate surrogate spheres (ZrN) as a development process for coating UN spheres.

As schematised in Fig. 2.10, the spheres were loaded in an alumina boat and placed into the chamber of a CVD reactor specially designed at Archer Technicoat Ltd. for W coatings. This CVD of W used tungsten hexafluoride (WF_6) and hydrogen as reactive gases at 623 K and 10 mbar in an established argon flow. Original images and additional details about the design of the CVD apparatus are not allowed to be shared due to intellectual property. Additional information regarding the experimental parameters and methodology are described in Paper V.

The results of UN spheres encapsulated with W by the CVD method are not included in this thesis because of time constraints due to additional administrative work to export and process the spheres at a non-nuclear related industry in the United Kingdom. Nevertheless, the results of this ongoing experiment will be presented and discussed in the final version of Paper VI.

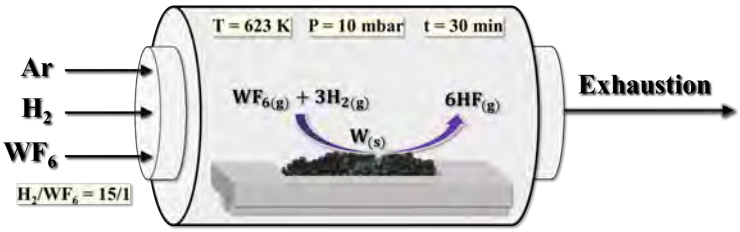

Figure 2.10: Illustration of a chemical vapour deposition process developed to encapsulate spheres with tungsten metal.

2.2.3 Physical vapour deposition

Physical vapour deposition (PVD) technology is a versatile technique that produces films and coatings of thickness varying from Ångstroms to millimetres. In the sputtering process, a glow discharge at a given pressure produces gas ions (usually argon) that bombard the target material (or cathode) and remove atoms from it. These atoms then pass into the vapour phase and deposit onto the substrate [63].

Fig. 2.11 pictures a simplified sputtering process and the designed PVD coater at the Belgian Nuclear Research Centre (SCK CEN). The PVD coater installation consists of common parts of a PVD coater device, which includes a vacuum chamber, pre-vacuum pump, molecular turbo-pump and targets. What is unique in this system is a vibrating unit positioned underneath the holder plate to agitate particles. The vibration creates a circular and spinning motion of the spheres around the plate (located under the targets). Thus, a uniform coating layer is deposited onto the spheres' surface. Additional images and details about the design of the PVD system are not allowed to be shared due to intellectual property rights.

To perform the coatings, an aluminium plate was mounted on the vibrating apparatus, and approximately 10 g of spheres were loaded with a filler material (stainless steel spheres of 0.5 mm in diameter). The steel spheres were essential because the PVD apparatus is qualified to handle larger batches (2000 g). Thus, the samples and filler covered the plate to a reasonable volume so that the spheres kept a circular movement to be evenly coated.

The depositions were performed in a process vacuum of $5.0\text{x}10^{-3}$ mbar under an argon flow of approximately 70 mL/min for 4.5 h. The current was set constant at 2 A, and the voltage varied according to the target material. The as-coated spheres were separated from the filler by sieving.

The results concerning the surrogate steel spheres coated with Mo and W are described in this thesis, as well as UN spheres coated with Mo. However, due to administrative work to export UN spheres to Belgium and to obtain authorisation to use the recently qualified PVD coater at SCK CEN with nuclear materials, the ongoing experiments on coating UN spheres with W will only be reported in the final version of Paper VI.

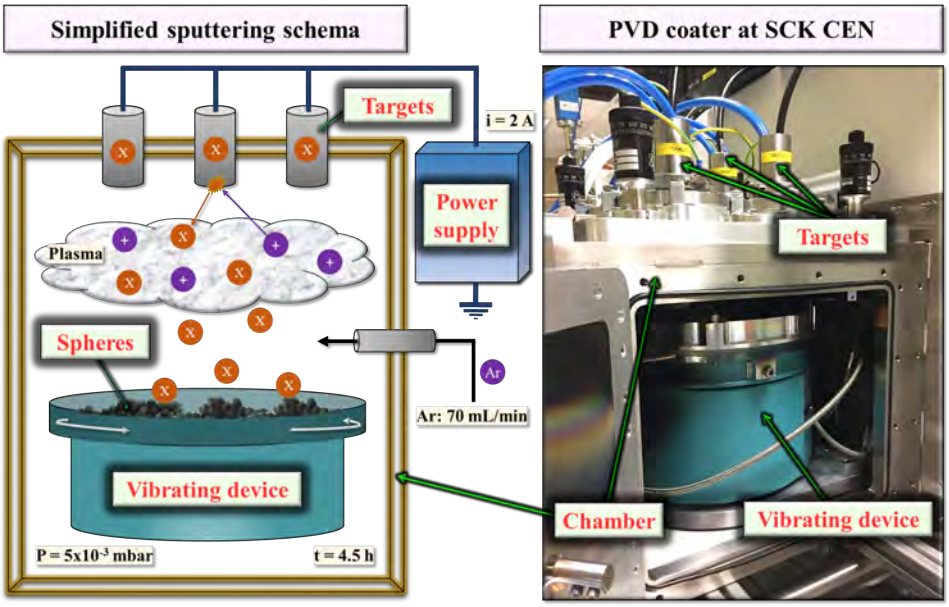

Figure 2.11: Illustration of a simplified sputtering process and the PVD coater used at SCK CEN, where X = Mo or W metals and + = Ar ions.

2.3 Spark plasma sintering

The spark plasma sintering (SPS) method, also named field-assisted sintering technology (FAST), electric pulse assisted consolidation (EPAC), and pulsed electric current sintering (PECS), is a technique amply used to consolidate several materials to practically full density, including metals, oxides, nitrides, carbides, composites, polymers, and more [66,67]. SPS is a versatile process that allows fast heating and cooling rates, short sintering times, low or high pressures and temperatures under an electric field. Thus, most materials can be consolidated at low temperatures and pressures using short sintering times.

A simplified representation of an SPS unit is portrayed in Fig. 2.12. It consists of a water-cooled chamber and pressure device with upper and lower rams, a DC pulse generator, and a controller that monitors the sintering temperature, total Z-displacement (shrinkage), vacuum pressure, average current and voltage during sintering. A powder sample is loaded in an SPS die with upper and lower punches, often made of graphite. Then, the assembled die is placed in an SPS chamber under a specified pressure for sintering.

All sintering experiments in this thesis were performed by SPS at the National SPS Facility in Stockholm, Sweden, using a modified Dr Sinter SPS machine inside an argon-filled glove box (< 0.1 ppm O_2). Fig. 2.13 shows the SPS machine used, including the glove boxes for sample preparation, die assembly and sintering (SPS

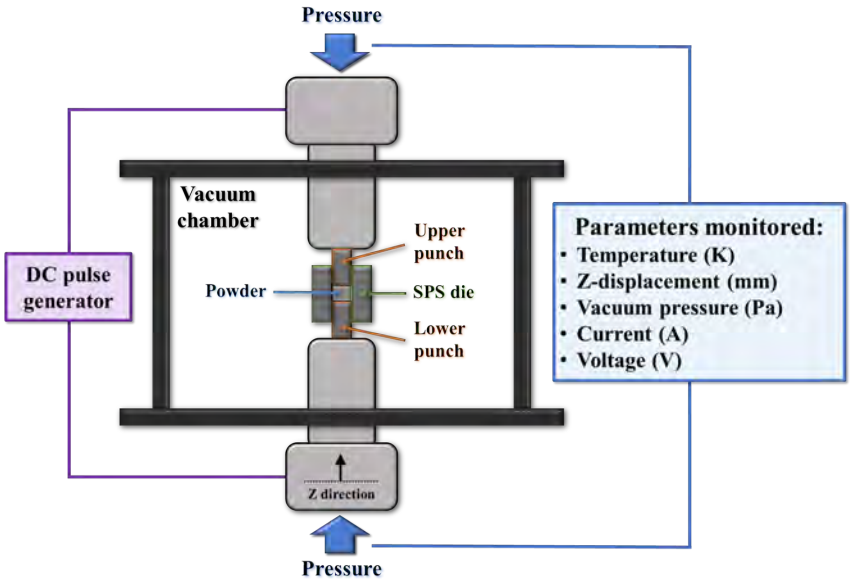

Figure 2.12: Simplified representation of an SPS unit showing an SPS die with powder and punches loaded in the SPS vacuum chamber.

chamber). The optical pyrometer was used to monitor the external temperature of the SPS graphite die.

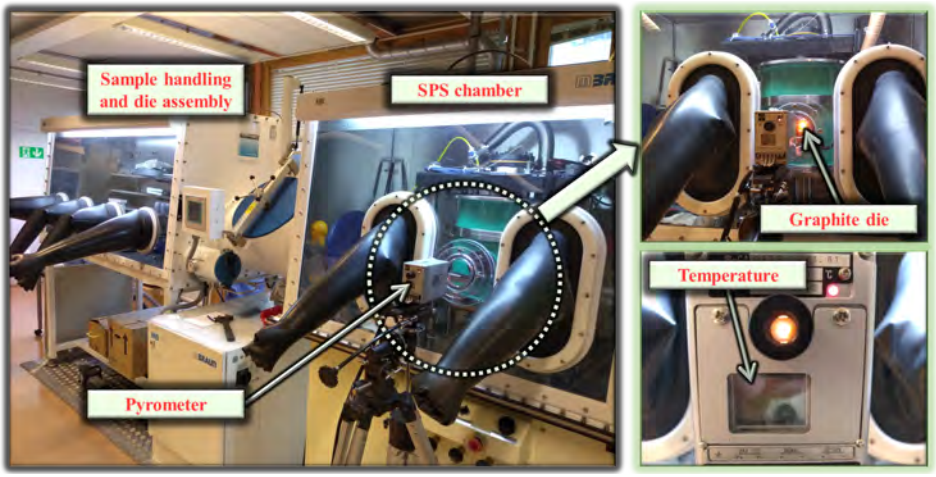

Figure 2.13: Modified Dr Sinter SPS machine at the National SPS Facility in Stockholm.

Fig. 2.14 schematically represents the main steps from sample preparation to a final sintered pellet. In summary, the samples were weighted and mixed (composite fuels) inside a glove box connected to the SPS machine (Fig. 2.13). The inner surface of the graphite dies (9.50 mm in diameter) was covered with a thin graphite paper to avoid direct contact between the samples and dies. Graphite punches were used to compact the powders and mixtures at the desired uniaxial loading pressures. Small graphite disks were placed in the assembled dies to avoid direct contact between the samples and punches. The external surfaces of the dies were covered with three sheets of graphite felt to reduce heat loss. Circular windows of about 10 mm were cut into the felt to allow temperature measurements on the external surface of the dies by an optical pyrometer. The lower limit of detection of the pyrometer was 673 K, which means that the heating profiles started at this temperature.

The SPS chamber was loaded with the assembled dies and depressurised to about 5 Pa. Some parameters were monitored as a function of time during the sintering process, including external die wall temperature, applied uniaxial pressure (sintering pressure), total z-axis displacement of the punches (shrinkage), vacuum line pressure, current, and voltage. In this thesis, the external temperature of the dies, which might be slightly different from the temperature in the centre of the samples, is considered the "sintering temperature" of the experiments, and the applied uniaxial pressure is reported as the sintering pressure. Additionally, the total z-displacement considers the elastic and thermal deformations of the materials, combining the effects of temperature, applied pressure, and sample weight. Finally, the samples were sintered at different temperatures, pressures, holding times, and heating and cooling rates, as detailed in the subsequent sections.

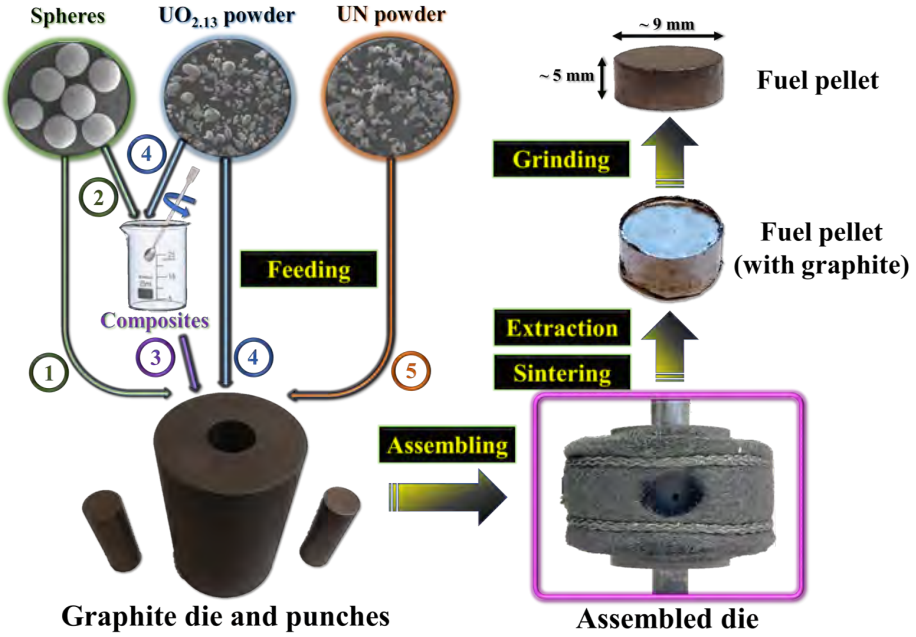

Figure 2.14: Schematic representation of the main steps used to sinter the samples by SPS. Pure UN spheres (1), $UO_{2.13}$ powder (4) and UN powder (5), as well as uncoated and encapsulated UN-UO_2 ATF composites (3), were sintered in assembled dies, extracted, and ground to obtain the final fuel pellets.

2.3.1 Uncoated UN-UO_2 composites

Uncoated UN-UO_2 composites sintered by SPS were relevant to understand the interaction between UN and UO_2, and how the SPS parameters affect the amount and morphology of the phases in the sintered composites. Based on that, a mechanism for the α-U_2N_3 phase formation was proposed. Thus, pure $UO_{2.13}$ powder, pure UN spheres, and mixtures of 10, 30 and 50 wt% of UN spheres and $UO_{2.13}$ powder were sintered as described in Paper I.

The materials were sintered at different temperatures, pressures, holding times, and cooling rates to evaluate the influence of each parameter on the sintering behaviours, densities, and microstructures. Table 2.2 summarises the selected SPS parameters. The samples are named UN(X)-UO_2(T/P/t/SC or FC), where "X" is the amount of UN spheres in weight percent (wt%), "T" is the sintering temperature, "P" is the applied pressure, and "SC" and "FC" are the slow (SC) and fast cooling (FC) rates, respectively. For instance, the sample UN(30)-UO_2(1373/80/3/SC) is related to a mixture of 30 wt% of UN spheres and 70 wt% of $UO_{2.13}$ powder, sintered at T = 1373 K and P = 80 MPa for t = 3 min at 1373 K, and using a slow cooling rate from 1373 K (SC) until room temperature.

Table 2.2: SPS parameters used to sinter uncoated UN-UO_2 composite fuels and the references UO_2 and UN (Paper I).

Parameters	Values
UN spheres, X (wt%)	0, 10, 30 and 50
Sintering temperature, T (K)	1373 and 1773
Sintering pressure, P (MPa)	40 and 80
Sintering time, t (min)	3 and 60
Heating rates 1373 K / 1773 K (K/min)	100 until 1273 K / 1573 K
	50 until 1373 K / 1773 K
Slow cooling from 1373 K, SC (K/min)	10 until 1173 K
	20 until 973 K
Slow cooling from 1773 K, SC (K/min)	10 until 1573 K
	20 until 1373 K
	50 until 973 K
Fast cooling from 1373 K or 1773 K, FC (K/min)	50 until 1173 K

The sintered materials were extracted from the graphite dies and prepared for characterisation, which consisted of removing all residual graphite by grinding with SiC paper (grit 280) (Fig. 2.14).

2.3.2 UN-X-UO_2 systems

This section presents the studies to select promising coating candidates in the UN-X-UO_2 systems (X = V, Nb, Ta, Cr, Mo, W). As previously stated, this thesis does not aim to cover all possible coating candidates; instead, it focuses on refractory metals as a starting point for further studies. The subsections will present density functional theory (DFT) calculations (Paper II) and pressure-assisted diffusion experiments (Paper III) to evaluate the most suitable refractory metals for coating UN spheres.

2.3.2.1 Electronic structure calculations

Density functional theory (DFT) calculations [68,69] with Hubbard corrections [70–72] were performed to evaluate the interface interactions and diffusion behaviours at the UN-X interfaces. The compatibility of the materials was investigated by computing the reaction energies of the prospective interface reactions to evaluate the formation of new phases. Moreover, thermodynamics analysis of the interfaces helped to understand the stability of (potential) newly created phases and their evolution. The calculation methodologies are reported in Paper II.

2.3.2.2 Pressure-assisted diffusion experiments

The developed pressure-assisted diffusion setup used to investigate the interface interactions in UN-X-UO_2 is portrayed in Fig. 2.15. All materials were assembled in SPS graphite dies (9.5 mm inner diameter), with the UN pellet at the bottom, the metal disks in the middle, and the $UO_{2.13}$ powder on top. The polished UN pellets and both surfaces of the metal foils were lastly polished inside the SPS glove box (< 0.1 ppm O_2), using a diamond paste of 0.25 μm, to minimise oxidation of the surfaces. Afterwards, the materials were placed inside the SPS dies and transferred to the SPS chamber for the heat treatments at 1773 K and 80 MPa for 10 min in a vacuum of ∼5 Pa. These parameters were chosen based on the most severe condition used to sinter uncoated UN-UO_2 (Paper I). More details regarding the sample preparation and heat treatment are found in Paper III.

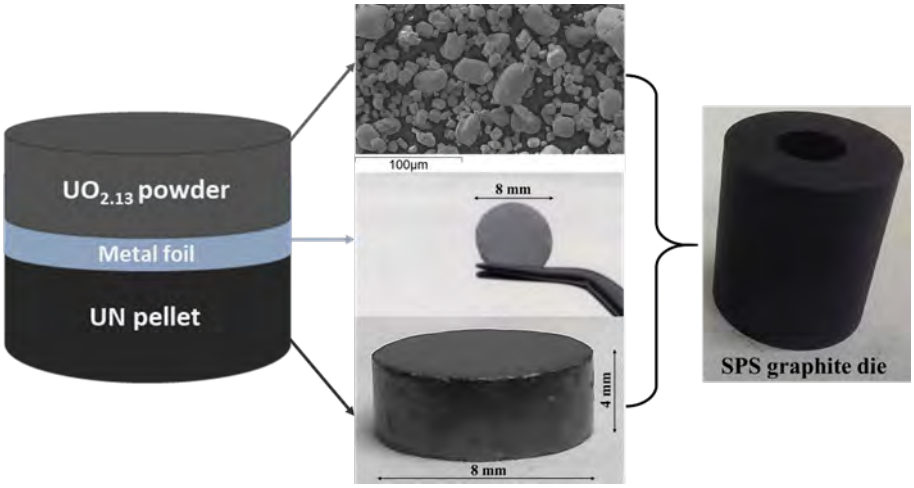

Figure 2.15: Experimental setup for the developed pressure-assisted diffusion experiments. This system consisted of a polished UN pellet at the bottom of the graphite die, a polished metal disk in the middle, and the $UO_{2.13}$ powder on top.

Fig. 2.16 shows the developed methodology for characterising the systems and minimising cracks and spalls at the interfaces UN-metal-UO_2 during sample preparation for analysis. The heat-treated samples were extracted from the dies and directly mounted in a resin, without grinding the external surfaces to remove residual graphite. Subsequently, the mounted specimens were cut in half to expose the cross-sections for ceramography and FIB milling of selected samples.

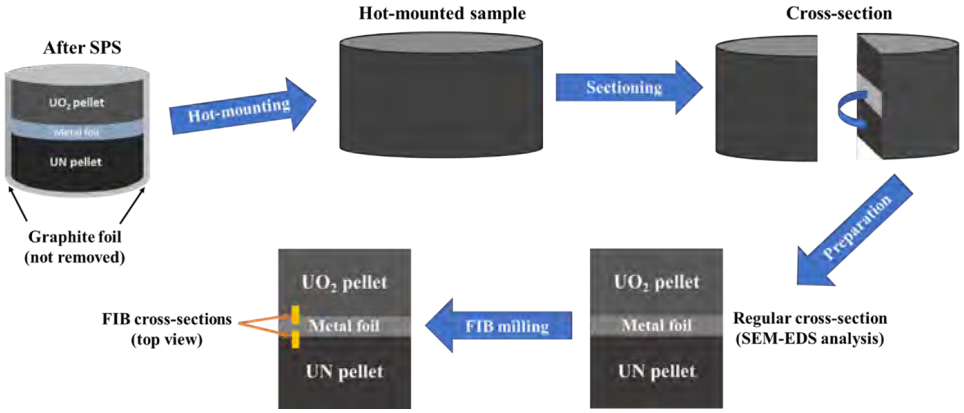

Figure 2.16: Experimental steps from the heat-treated samples until the characterisations. FIB cross-sections were obtained in some specific samples to better examine the bulk interfaces.

2.3.3 Encapsulated surrogate composite fuels

Coated ZrN-UO_2 surrogates were fabricated to develop and evaluate the powder (Mo, W) and CVD (W) coating methodologies, aiming for the characterisation of the layers and potential interactions with UO_2 during fabrication. To do so, composite fuels containing about 15 wt% of (uncoated) ZrN, Mo(wet)/ZrN, Mo(binder)/ZrN, W(binder)/ZrN, or W(CVD)/ZrN spheres in UO_2 were fabricated by SPS. The spheres were manually mixed with $UO_{2.13}$ in a beaker and poured out in a graphite die (9.5 mm inner diameter) inside an argon-filled glove box (< 0.1 ppm O_2) connected to the SPS machine. The SPS chamber was then depressurised to about 5 Pa to sinter the samples at 1773 K and 80 MPa for 3 min, i.e., the most severe condition used previously (Paper I). Additional details regarding the powder- and CVD-coated surrogates are reported in Paper V.

Similarly, about 15 wt% of steel spheres (SS) coated with Mo (Mo(PVD)/SS) or W (W(PVD)/SS) were mixed with $UO_{2.13}$ and sintered by SPS at 1373 K and 80 MPa for 3 min, as described in the powder-coated composites. This lower temperature was due to the lower melting point of the steel spheres (< 1773 K), but it is high enough to provide a dense UO_2 matrix with embedded spheres when SPS is used (Paper I). More details are found in Paper VI.

2.3.4 Encapsulated UN-UO_2 composite fuels

Encapsulated UN-UO_2 accident tolerant fuels were fabricated by mixing $UO_{2.13}$ with 15 wt% of UN spheres coated with Mo or W nanopowders, followed by sintering using the same SPS parameters used to sinter the surrogate fuels: 1773 K, 80 MPa, 3 min in vacuum (Papers V and VI).

Ongoing experiments regarding encapsulated composites containing UN spheres coated with W (CVD and PVD) or Mo (PVD) are not presented in this thesis due to time constraints. However, these encapsulated fuels will be included in the final version of Paper VI.

2.4 Evaluation of composite fuels

Uncoated and encapsulated UN-UO_2 composite fuels were tested and evaluated. The following subsections will describe the oxidation resistance of uncoated UN-UO_2 in air up to 973 K, and the thermal properties of uncoated and encapsulated UN-UO_2 composites using finite element modelling.

2.4.1 Oxidation behaviour in air

The oxidation kinetics of the uncoated composites were assessed by thermogravimetric analyses (TGA) in synthetic air, using a heating rate of 5 K/min until 973 K and 10 min at this plateau. The sintered composites were crushed into small pieces of about 45 mg for the experiments. The oxidation onset temperature (OOT) was defined as the temperature at which 5 % of the total weight variation was observed, while the maximum reaction temperatures (MRTs) were obtained by analyses of the first derivatives of the weight variation curves (%/min). Experimental details and discussions are reported in Paper VII.

All TG runs were performed in triplicate to obtain the standard deviations of the mean values of total weight variation (%), OOTs, and MRTs, as well as the repeatability and reliability of the TG results. $UO_{2.13}$ powder and pristine UN spheres were also oxidised to provide insights into their oxidation behaviours and data for comparison with pure UO_2 and UN sintered samples.

Additionally, differential scanning calorimetry (DSC) analysis was performed under a synthetic air flow in a sintered specimen containing (initially) 50 wt% of UN spheres in $UO_{2.13}$. This experiment evaluated the thermodynamics involved during oxidation of the three phases present in the sintered material, i.e., UO_2, UN and α-U_2N_3. The material was also heated at 5 K/min up to 973 K, kept at this temperature for 10 min, and cooled to room temperature. Additional details and discussions are also reported in Paper VII.

Due to laboratory issues, and time and logistic limitations to coat the UN spheres, the oxidation behaviours of encapsulated UN-UO_2 ATF composites will only be presented in the final version of Paper VI. In these experiments, spark plasma sintered pellets of about 9 mm in diameter and 5 mm in height will be oxidised in air at 10 K/min up to 973 K to evaluate the oxidation kinetics, oxidation onset temperatures, and maximum reaction rates of encapsulated fuels containing 30 wt% of coated spheres (Mo(nano)/UN, W(nano)/UN, W(CVD)/UN, Mo(PVD)/UN or W(PVD)/UN). These results will be compared with the UO_2 pellet and uncoated UN-UO_2 composite reference samples, also sintered by SPS using the same parameters.

2.4.2 Thermal properties

Thermal analyses were performed by finite element modelling (FEM), using the FEM tool COMSOL Multiphysics® [73]. Thermal conductivity of UN-UO_2 and UN-X-UO_2 (X = Mo, W) composites, containing different weight fractions of UN (10, 30, 50, 70 wt%) and coating thicknesses (1 μm and 5 μm), were computed assuming no interactions between the spheres, coating materials and UO_2 matrix. Then, the resulting effective thermal conductivity of the composites was used to evaluate the thermal fuel performance of the composites in a nuclear fuel pellet under normal operating conditions in LWRs. The maximum fuel centreline temperatures are compared with that in UO_2 as a benchmark. Details of this study are reported in Paper VIII.

2.5 Characterisation techniques

Several techniques were used in this thesis to characterise the samples according to their chemical compositions, crystalline phases, morphologies, chemical distributions, crystallographic orientations, and thermal properties. The following subsections describe each technique used, its importance, and limitations.

2.5.1 Chemical analyses

Chemical analyses were performed to quantify the amount of nitrogen, oxygen, and carbon in the UN spheres. N and O analyses were performed by the inert fusion method, using a LECO TC436DR instrument inside a nitrogen-filled glove box to minimise oxygen incorporation during sample preparation and analyses. C content was obtained by the combustion method using a LECO CS744 instrument. Additional details regarding the techniques and calibration procedures are described in Papers I and VII.

2.5.2 X-ray diffaction

X-ray diffraction (XRD) is a tool used to investigate the fine structures of matter. This technique is widely used to determine (but not limited to) crystal structures, crystalline phases, and weight fractions of crystalline materials following the Bragg Law of diffraction [74, 75]. In this thesis, all XRD examinations were performed using a Siemens D5000 diffractometer with a Cu_{K_α} radiation (Ni filter), 2θ within 20° and 120°, and a step of 0.02° with either 9 s (Papers I and VII) or 4 s (Paper III) of acquisition time. The weight fractions of each phase in the samples and the lattice parameters were computed using the software MAUD (Materials Analysis Using Diffraction) [76].

Before the analysis, the solid samples (i.e., spheres and pellets) were milled into powder inside a glove box (argon atmosphere) and encapsulated in a holder for XRD acquisitions under inert atmospheres to avoid oxidation during analysis.

$UO_{2.13}$, U_2N_{3+x}, and UN powders were also characterised using the same sample holder. More details about sample preparation, XRD analysis, and software MAUD are described in Papers I, III and VII.

2.5.3 Scanning electron microscopy

Scanning electron microscopy is a powerful technique to observe and characterise organic and inorganic materials on a micrometre (μm) and nanometre (nm) scale [77, 78]. In an SEM (Fig. 2.17), a focused electron beam interacts with the sample in a microvolume either in a static way, to obtain a local analysis, or scan across a specimen to form images. This interaction generates signals in a specific emission volume within the sample that is used to examine surface topography, crystallography, composition, etc.

The signals of utmost interest in the SEM are the secondary (SE) and backscattered (BSE) electrons, as well as the characteristic X-rays, originated during electron bombardment, as illustrated in Fig.2.17. SE is restricted to a very small volume near the sample surface and is useful to assess topographic details at a resolution about the size of the focused electron beam. BSE is obtained from a deeper region in the sample and provides important contrast between atomic numbers, which is useful to differentiate elements, phases, precipitates, and so on. Characteristic X-rays emitted from samples are measured by an energy-dispersive spectrometer (EDS) detector that is often coupled to the SEM. This detector is used to qualitatively and quantitatively obtain chemical information from a deeper region in the form of a spectrum. This interaction volume is a function of the electron beam accelerating voltage (kV), electron probe current (A), electron probe diameter (nm), and so on [77, 78].

In this thesis, SEM analyses were performed with energy-dispersive X-ray spectroscopy (EDS) [77, 78], wavelength-dispersive X-ray spectroscopy (WDS) [78, 79], electron backscatter diffraction (EBSD) [78,80], and focused ion beam (FIB) [78,81]. The different microscopes used for each purpose are described in the enclosed Papers.

The SEM parameters such as accelerating voltage (E), electron beam current (i), working distance (WD), and detector mode were adjusted to induce the generation of SE, BSE, or X-rays at low (250-5000 X) and higher magnifications (25000-200000 X). As a general rule, low voltages (3-5 kV), short working distances ($\leq$ 5 mm), and low currents ($\leq$ 0.40 nA) were selected to increase the yield of SE while acquiring topographical details. For the SEM-EDS measurements, higher currents (1.8-8.6 nA) at WD = 5 mm and an overvoltage (U = E/E_c) of 2.5 were often used to effectively generate X-rays at an optimum interaction volume [78], where E = instantaneous beam energy (7-15 keV) and E_c = critical ionisation energy (depending on the element in the K-, L-, or M-shells, in keV).

SEM-EDS was used to (qualitatively) visualise the chemical distribution of elements and phases in the samples and to identify (semi-quantitatively) the phases in the samples. Additionally, WDS analyses were performed to corroborate some

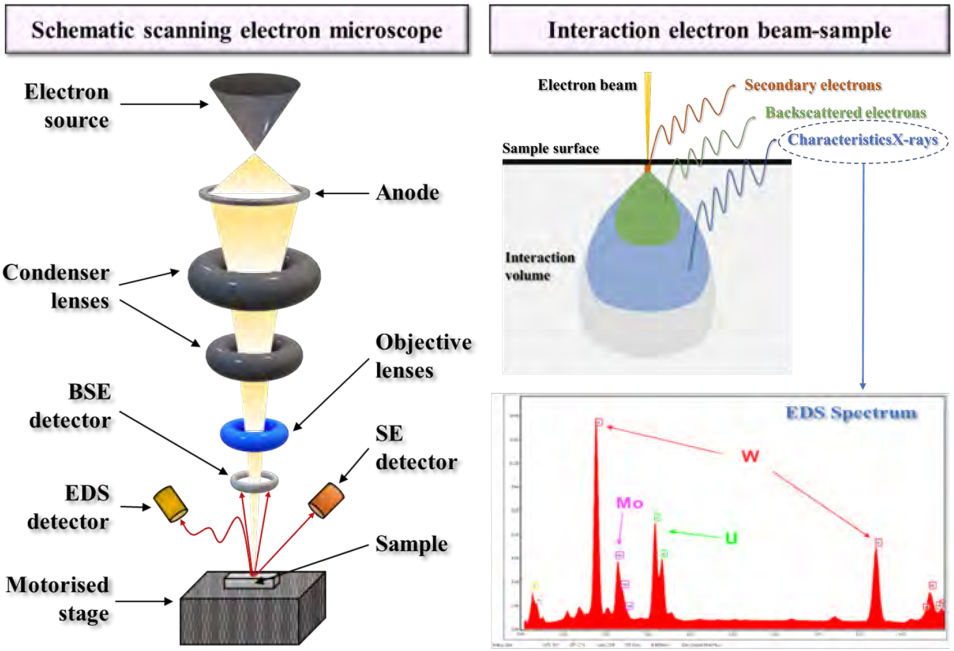

Figure 2.17: Schematic representation of the main components of a scanning electron microscope and an illustration of the interaction between the electron beam and the sample.

EDS measurements when identifying and differentiating the UO_2, UN and U_2N_3 phases in the composites. EBSD was also applied to identify the α-U_2N_3 phase and to assess the grain morphologies, sizes, and crystallographic orientations in the encapsulated composites. FIB milling was used to evaluate fresh cross-sections, excluding any influence of regular cross-section preparation (cutting, grinding and polishing). Table 2.3 summarises the principal parameters used for characterisation and the respective papers where they appear.

Table 2.3: Summary of the main parameters used for the microscopy examinations.

Analysis	Voltage (kV)	Current (nA)	WD* (mm)	Papers
SEM-SE	3 - 5	≤ 0.40	≤ 5	I,III-VII
SEM-BSE/EDS	7 - 15	1.8 - 8.6	5 - 10	I,III-VII
WDS	6 - 10	> 5	9 - 10	I
EBSD	15 - 20	1 - 10	12 - 20	I,V
FIB	2 - 30	0.05 - 9	5 - 7	III,V,VI

*Working distance.

2.5.4 Thermal analysis

Thermogravimetric analysis (TGA) and differential scanning calorimetry (DSC) were used in this thesis to assess the thermal properties of the samples. TGA is an amply used technique to obtain quantitative information on the change in mass as a function of time as the sample is heated, cooled, or kept at constant temperatures. The atmosphere used in the experiments is also vital to properly characterise the mass evolution of the specimen [82, 83]. In this thesis, TGA was used to assess the oxidation behaviours of the raw materials and ATF composites using a TGA Discovery analyser (TA Instruments). The weight variations (wt%), oxidation onset temperatures (OOTs), and maximum reaction temperatures (MRTs) were obtained from each experiment. More details regarding the tool, sample preparation, and procedure are found in Paper VII. In summary, the samples were heated in a synthetic air flow of 20 mL/min at 5 K/min up to 973 K, kept at this plateau for 10 min, and then cooled to room temperature.

DSC is a thermal method that provides quantitative results of the amount of heat required to increase the temperature of a sample and a reference material as a function of temperature. This technique is commonly used to identify phase transitions based on more (or less) heat needed to flow to the sample than the reference to maintain both temperatures equal. Depending on whether the flow to the sample is less or more, the process is characterised as exothermic or endothermic [82, 83].

The DSC runs were performed in a Netzsch STA 449 F3 Jupiter under a synthetic air flow and heating rate of 5 K/min up to 973 K with a holding time of 10 min at this plateau. These experiments were used to evaluate the thermodynamics involved during the oxidation of the reference samples and ATF composites. More details regarding sample preparation, procedures, and processing parameters are reported in Paper VII.

Chapter 3

Results

This chapter will present the results of this thesis that are reported in detail in Papers I to VIII, presented in the List of Publications included in this thesis. First, the fabrication and characterisation of uncoated UN-UO_2 composite fuels are presented, followed by the selection of potential coating materials, developments and coating techniques adopted, fabrication and characterisation of coated composites, and composite fuel evaluations.

3.1 Uncoated UN-UO_2 composite fuels

This section is focused on understanding how the sintering parameters influence the fuel microstructure and phases; how UN and UO_2 interact during sintering; and then proposing a mechanism for the α-U_2N_3 formation. Paper I is dedicated to this section.

3.1.1 Influence of sintering parameters

The influence of the initial amount of UN spheres (wt%), sintering temperature, applied pressure, sintering time, and cooling rates on the composite densities and microstructures are presented and discussed in this section. Fig. 3.1 summarises the impact of these parameters on the sintered densities and amount of phases in the composites.

The results show that the faster the cooling, the higher the amount of UN and the lower the α-U_2N_3 content. This behaviour is observed by comparing the samples UN(30)-UO_2 (1373/80/3/SC) and UN(30)-UO_2 (1373/80/3/FC), in which the UN content increased from 10.3 $\pm$ 0.2 wt% to 13.3 $\pm$ 0.5 wt%, and the amount of α-U_2N_3 decreased from 15.1 $\pm$ 0.7 wt% to 12.7 $\pm$ 0.7 wt% when the system was cooled faster. The influence of temperature and pressure followed the same trend: the higher the temperature (or pressure), the higher the amount of α-U_2N_3 and the lower the amount of UN. Additionally, by increasing the sintering temperature from

1373 K to 1773 K, the densities increased from 88.3 - 89.9 %TD to 91.3 - 95.6 %TD, respectively. This behaviour is expected since the sintering process is a temperature-driven diffusion mechanism [84]. However, the increment in sintering time from 3 min to 60 min did not significantly affect the sintered density and amount of phases in the final composites, as shown in samples UN(10)-UO_2 (1773/80/3/FC) and UN(10)-UO_2 (1773/80/60/FC).

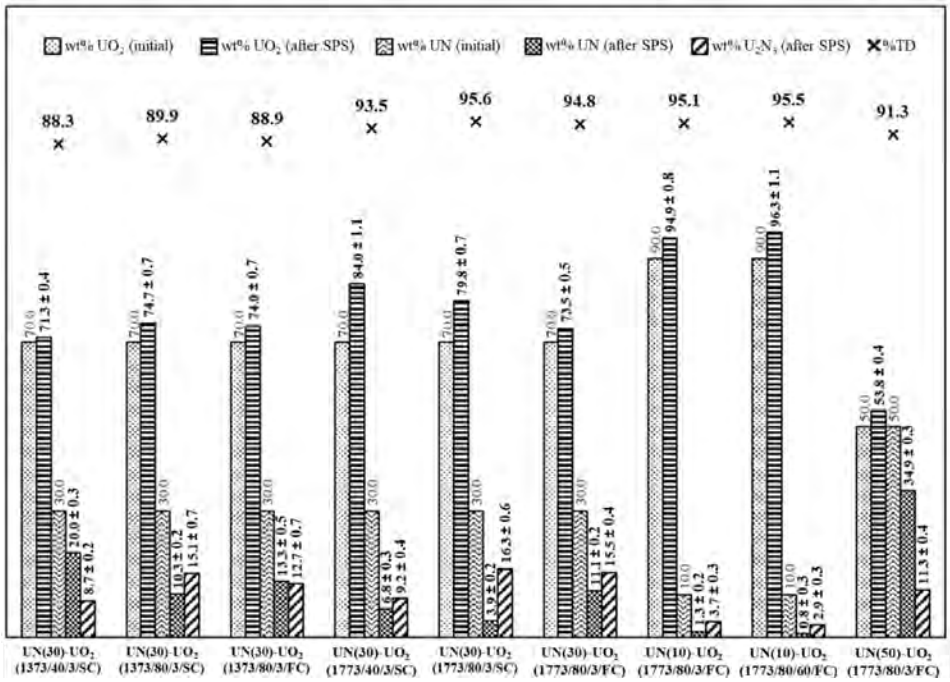

Figure 3.1: Influence of the initial amount of UN, temperature, pressure, time and cooling rates on the sintered densities and amount of phases after sintering. The samples are identified according to Table 2.2.

3.1.2 Mechanism for α-U_2N_3 formation

A typical microstructure of an uncoated UN-UO_2 composite is shown in Fig. 3.2. The lower magnification images (Figs. 3.2(a) and (b)) show UN spheres embedded in the UO_2 matrix, while Fig. 3.2(c) highlights the interface between UN and UO_2, the phases in the composite (UN, UO_2, and α-U_2N_3), an additional oxide layer inside the UN sphere, and the oxygen and nitrogen paths during sintering. This figure summarises the interactions between the UN spheres and $UO_{2.13}$ powder during sintering.

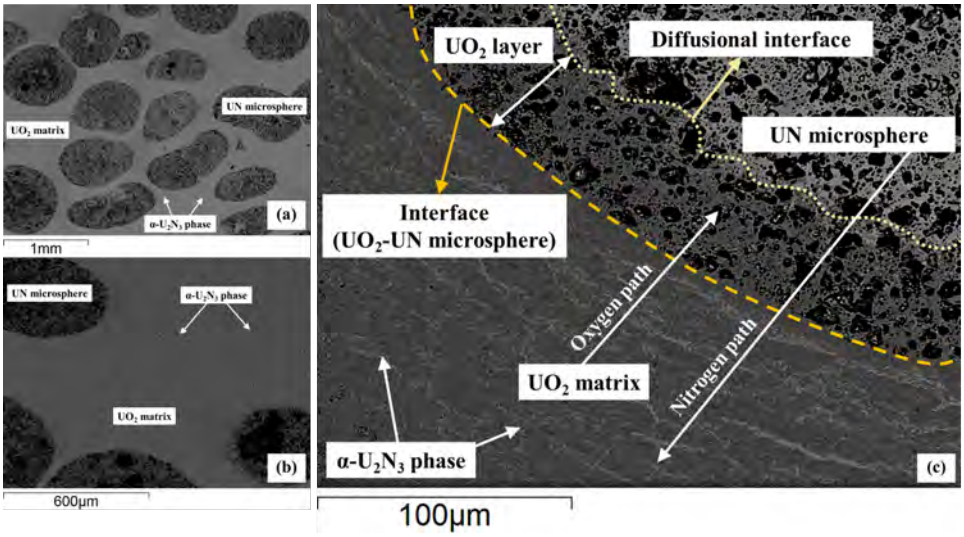

Figure 3.2: SEM images of an uncoated UN-UO_2 composite fuel, showing the embedded UN spheres and highlighting the interface between both fuels, the phases, an additional oxide layer inside UN, and the oxygen and nitrogen paths during sintering.

The formation mechanism for the sesquinitride phase may be explained by the interdiffusion of O and N during the heating step of sintering, followed by a precipitation phenomenon during cooling. During heating, oxygen from the oxide powder migrates towards the UN spheres and interacts with the nitride phase, forming an oxide layer inside the UN. This assumption is based on the sintering behaviour (SPS vacuum pressure) and DSC analysis (UN(30)-UO_2 composite), as described in detail in Paper I. Briefly, the release of oxygen, which starts at about 1100 K, as observed during the sintering of pure $UO_{2.13}$ powder, is not observed when sintering the composites. Moreover, the DSC result shows a broad exothermic peak also starting at approximately 1100 K, which suggests that oxygen from the oxide fuel is reacting with UN and not leaving the sample.

Following the opposite direction, nitrogen diffuses into the oxide phase due to the increase of its solubility in UO_2 with temperature [85]. Therefore, a long-ranged solid solution, such as $UO_{2-x}N_x$, is suggested to form in the UO_2 matrix. Thus, nitrogen from UN can stabilise the UO_{2-x} matrix after the mutual incorporation of N in UO_{2-x} and O from UO_{2+x} in UN. Additionally, oxygen can also diffuse from the stoichiometric ($UO_{2.0}$) [49] and hypo-stoichiometric (UO_{2-x}) forms [86].

At the sintering temperatures and holding times, the proposed solid solution $UO_{2-x}N_x$ is at its maximum amount and dispersion. During cooling, the solubility of nitrogen in UO_2 decreases and N is then redistributed from $UO_{2-x}N_x$ into the UO_2 matrix to form the sesquinitride phase. DCS analysis reported in Paper I

shows that this precipitation starts at about 1250 K and continues until approximately 1000 K, when the broad exothermic peak disappears. The morphology and extension of the α-U_2N_3 precipitates mostly depend on the sintering temperature and cooling rates, as shown in Fig 3.3. The precipitates formed in the sample sintered at 1373 K are finer than the ones at 1773 K. Moreover, the morphology of α-U_2N_3 is formless at 1373 K and does not have the sharp and interconnected lamellar structure observed at 1773 K (Fig 3.3 top). This long-range structure has an average thickness of $\sim$4 µm and is $\sim$15 µm long, while the quasi-lamellar structure at 1373 K has dispersed and much finer precipitates of a few microns in average sizes ($\sim$1–2 µm). Thus, higher temperatures allow an extended dissolution of N in UO_2 and, therefore, provide a greater amount of precipitates in the matrix to form the lamellae during cooling.

The morphology and size of the precipitates are significantly affected by the variations in the cooling rates. Fig 3.3(bottom) compares the samples sintered at 1773 K and 80 MPa for 3 min using the slow (SC) and fast (FC) cooling profiles (Table 2.2). As discussed before, the SC profile provided a long-ranged lamellar structure. However, in the fast-cooled sample, the morphology and size of the precipitates drastically changed to a "coarse grain" structure of different sizes ($\sim$5–35 µm). This coarse structure is characteristic of a precipitation mechanism [87], in which nitrogen is redistributed within UO_2 due to its solubility decrease in the $UO_{2-x}N_x$ solid solution at lower temperatures [85]. Thus, the faster the cooling, the lower the N redistribution time and, consequently, the less homogeneous the structure.

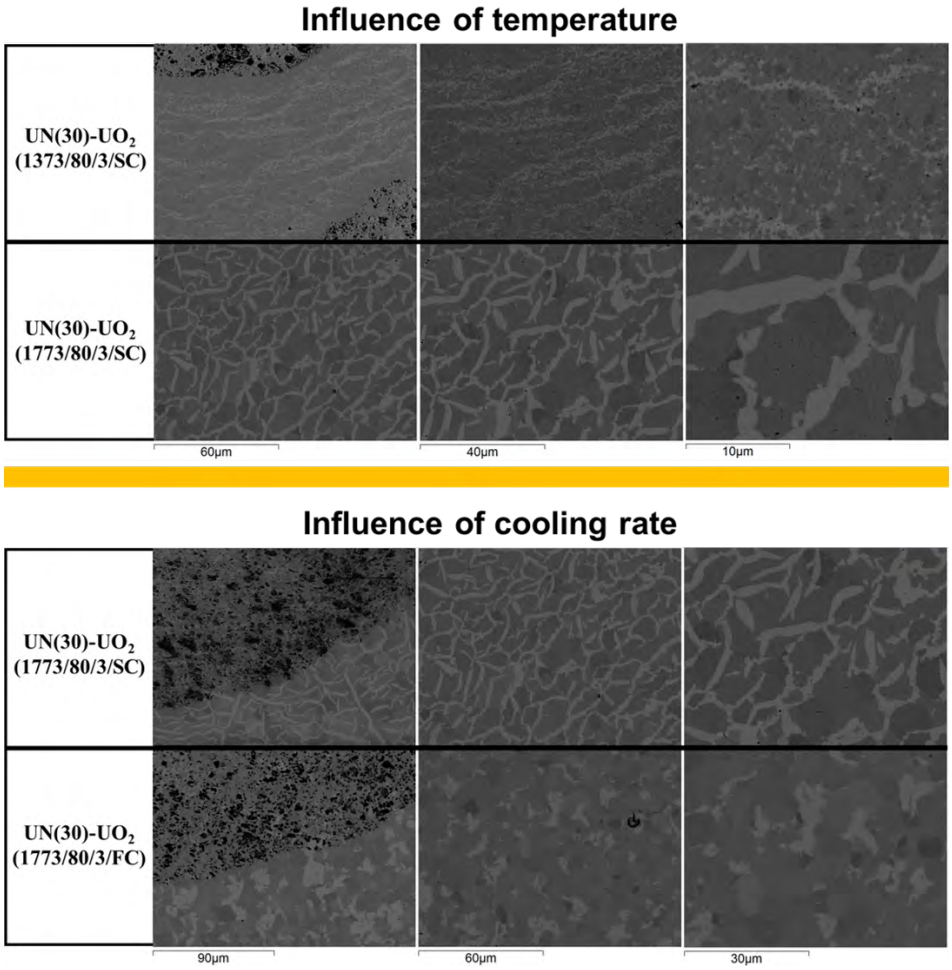

Figure 3.3: Influence of the sintering temperature (top) and cooling rates (bottom) on the morphology and extension of the precipitates (α-U_2N_3).

Based on the results presented in this section, it becomes possible to minimise the formation of the undesired α-U_2N_3 while obtaining a dense composite fuel ($\sim$96 %TD). For instance, low temperatures ($\leq$1173 K) and pressures ($\leq$40 MPa), combined with a fast cooling rate (FC), are efficient to maximise the amount of UN in the composite and, consequently, minimise the sesquinitride formation. However, the UN spheres would interact with UO_2 at high temperatures (>1173 K) anyway, e.g. during operation in LWRs. Thus, further developments are needed to avoid this interaction. To address this issue, the use of encapsulated UN spheres can prevent the interactions between both fuels and eliminate the formation of the sesquinitride phase.

3.2 Coating candidates

This section will present modelling and experimental studies to select the most suitable refractory metals to encapsulate the UN spheres.

3.2.1 Compatibility of UN-metal and UO_2-metal by DFT

Density functional theory (DFT) calculations were performed to study the interactions and kinetics at the UN-X interfaces (X = V, Nb, Ta, Cr, Mo, and W), which are described in detail in Paper II. The compatibility was characterised by computing the reaction energies at the UN/X interfaces to verify the formation of new phases. All possible UN-X interface reactions enthalpies (ΔH_r) were calculated and the lowest values are listed in Table 3.1.

Table 3.1: UN/X reaction enthalpies (ΔH_r), in eV/atom, where X = V, Nb, Ta, Cr, Mo, and W. The reactions with the highest and lowest reaction enthalpies are highlighted in bold.

Metal	**Reaction**	ΔH_r **(eV/atom)**
V	UN+8V=V_8N+U	0.01
Nb	2UN+Nb=$UNbN_2$+U	0.11
Ta	**2UN+Ta=$UTaN_2$+U**	**-0.21**
Cr	3UN+Cr=U_2CrN_3+U	0.20
Mo	UN+2Mo=Mo_2N+U	0.55
W	**3UN+2W=W_2N_3+U**	**0.88**

The reaction between UN and Ta has a negative ΔH_r, which indicates that the ternary $UTaN_2$ is spontaneously formed within UN at the UN/Ta interface. The UN/V reaction has an approximately zero reaction enthalpy, suggesting that V_8N may form in V at UN/V driven by entropy at finite temperatures. All the other metals have positive reaction entropy values, which indicate no interactions with UN. However, it is worth mentioning that these reaction enthalpies were calculated at 0 K and some of them may occur at finite temperatures or under irradiation, leading to the formation of different interface phases. Since the reaction enthalpies at UN/Mo and UN/W have the highest positive values, Mo and W can be considered less prone to react with UN. Thus, the DFT results suggest that Mo and W are the most promising coating candidates to protect UN against interaction with UO_2. The other interface analyses and phase evolution at the interfaces are provided in Paper II.

Additional DFT studies were performed to evaluate the reactions and potential phase evolutions at the UO_2-W and UO_2-Ta interfaces [72]. The results indicate no interaction between both metals with UO_2 at 0 K, but they might interact at higher temperatures driven by entropy. Experimental investigations in the UN-X-UO_2 systems were performed at 1773 K and are summarised in the next section.

3.2.2 Pressure-assisted diffusion experiments

This section presents the experimental results in the UN-X-UO_2 composite systems (X = V, Nb, Ta, Cr, Mo, W) at 1773 K and 80 MPa for 10 min in vacuum, using the SPS method as a pressure-assisted diffusion apparatus. Paper III is dedicated to detail these experiments.

The regular cross-sections of all UN-X-UO_2 systems are summarised in Fig 3.4. The integrity of the interfaces between UO_2 and W, Ta, Nb, V and Cr were somehow compromised during the heat treatment. Yet, there were interactions between the UN pellet and Ta, Nb, V and Cr metals. Molybdenum behaved well and kept its structure after the high-temperature process. All the interface interactions are detailed and discussed in Paper III.

Based on both modelling and experiments, Mo and W have been demonstrated to be the most promising coating candidates among the refractory metals studied in this thesis. Thus, a more detailed investigation of the UN-Mo-UO_2 and UN-W-UO_2 interfaces is extracted from Paper III and is presented here.

Fig 3.5 shows the regular and FIB cross-sections of the UN-W-UO_2 system. Top-left SEM-EDS images show an irregular interface with voids between UO_2 and W. Additionally, the EDS map of W shows the presence of tungsten around some cracked regions within UO_2 (highlighted in the figure). The same pattern is observed in the two FIB cross-sections presented on the top-right side. The EDS chemical maps of U, W and O indicate that these elements are present around the cracks at the interfaces in both regular and FIB cross-sectioned images.

These results at the UO_2-W interface suggest that the thermodynamic relations between $UO_{2.13}$ and W are relevant at high temperatures. It seems that a ternary U-W-O phase was present during the heat treatment and left its original shape (forming voids and cracks) and trace compositions. Such assumption agrees with a previous study [88] that proposed a new fabrication process of UO_2-W composite fuels, which consists of a continuous W channel on the UO_2 grain boundary. Based on thermodynamic calculations, the authors controlled the sintering atmosphere to oxidise dispersed W particles to WO_3 above its melting point ($\sim$1743 K). Then, liquid WO_3 diffused via grain boundary and, finally, reduced to W metal in H_2 at 1923 K to form the W channels. It is reported that about 1 at.% of W was present in the UO_2 grains by electron probe microanalysis (EPMA), demonstrating that W has a certain solubility in UO_2 during such liquid-phase sintering process. Likewise, the qualitative EDS chemical map of W in Fig.3.5(top) might indicate some solubility of W in UO_2 during the heat treatment at 1773 K.

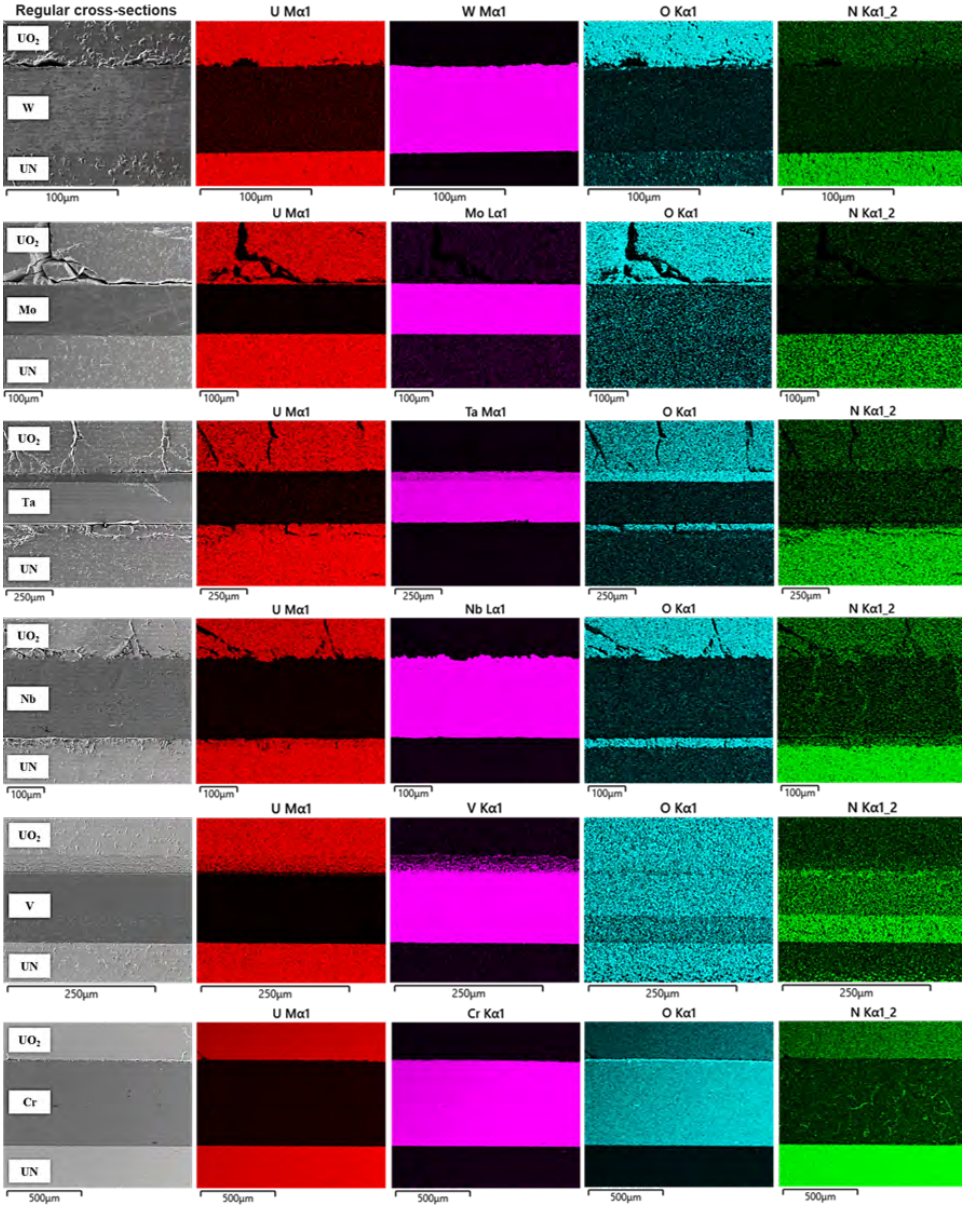

Figure 3.4: SEM-EDS images of the UN-X-UO_2 (X = W, Mo, Ta, Nb, V, Cr) regular cross-sections obtained after heat treatments at 1773 K and 80 MPa. The sample preparation and characterisation are described in Fig. 2.15 and Fig. 2.16, respectively.

A FIB cross-section of the W-UN interface in Fig.3.5(bottom) shows a well-defined and crack-free interface, but with O contamination from the UN pellet surface. In this image, EDS chemical maps of U, W, O and N are reported, together with an EDS line measurement to qualitatively assess the chemical composition profiles across the interface. The short-ranged variation ($< 0.5\mu$m) in the atomic compositions (at%) of U, W and N at the interface indicates that W acted as a barrier against N diffusion. This evidence validates the DFT calculations presented (details in Paper II). Previous experimental studies also show chemical stability between W and UN, even at high temperatures (1773–2273 K) in both Ar (with or without N_2) [89] and in high-purity He [90]. However, at very high temperatures (2573–2993 K), W and UN interact and form a eutectic containing W and liquid U as a result of UN dissociation [59, 90, 91].

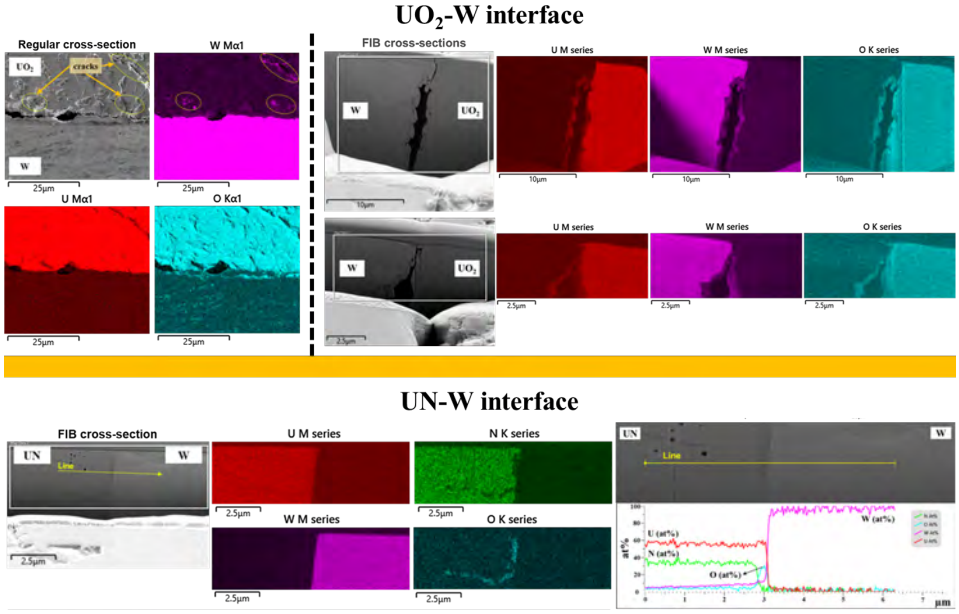

Figure 3.5: Regular and FIB cross-sections of the UN-W-UO_2 system showing the SEM-EDS maps and line measurements at the interfaces UO_2-W (top) and UN-W (bottom).

The UN-Mo-UO_2 system, previously reported in Fig.3.4, showed a cracked UO_2 bulk but a sharp interface between UO_2 and Mo. This crack behaviour, which is also observed in previous studies [24,92–94], may be formed due to differences in the linear thermal expansion coefficients (e.g. at 1773 K) of UO_2 ($14.6 \times 10^{-6}K^{-1}$ [95]) and Mo ($8.3 \times 10^{-6}K^{-1}$ [96], or due to differences in sintering shrinkage between the materials.

The FIB cross-section of the UO_2-Mo interface in Fig.3.6(top) shows a crack-free but irregular interface with a depth of less than 1 μm. Additionally, the EDS qualitative line measurements report an abrupt change in the U and Mo concentration across the interface, within a gradient of about 0.5 μm. A previous study [93] also reported no distinct reaction products at the UO_2-Mo interface of composites sintered at 1473 - 1873 K, with the interdiffusion of U and Mo occurring to an extent of just several nanometres. Therefore, a thin and dense layer of Mo in an UN-Mo-UO_2 composite fuel would be sufficient to avoid the interaction between UO_2 and UN during fabrication. Additional investigations regarding irradiation-induced diffusion of U, O, N and Mo need to be considered to better understand the system.

Fig.3.6(bottom) reports a sharp and crack-free interface between UN and Mo, with O contamination on the UN pellet surface. Similarly to UN-W, the qualitative line measurements portray a transition region at the interface of less than 0.5 μm

without forming a U-W-N ternary. These results agree with a recent study [97] that presents an innovative method to fabricate UN-Mo cermet fuels: sintered UN spheres encased in a Mo matrix by the SPS method at 1873 - 1973 K and 25 - 65 MPa (10 min, vacuum). Also, no interactions between UN and Mo were observed by the authors. It is reported that UN and Mo are inert even at high temperatures (up to 2473 K) in the presence of N_2 (10 v%) in Ar, but can react via liquid-phase sintering both in vacuum [89] and in N_2 (0.85 atm) at a very high temperature (2673 K) [91].

The experimental investigations at the W-N and Mo-UN interfaces reported in this thesis are in good agreement with the DFT calculations briefly presented above, which also demonstrate that W and Mo are chemically compatible with UN (Paper II). Thus, both results (modelling and experiments) indicate that W and Mo are good candidates to avoid interactions between UO_2 and UN during fabrication. Further analysis regarding the effect of irradiation should be performed to better understand the UO_2-W-UN and UO_2-Mo-UN systems and the effectiveness of the W and Mo coating layer.

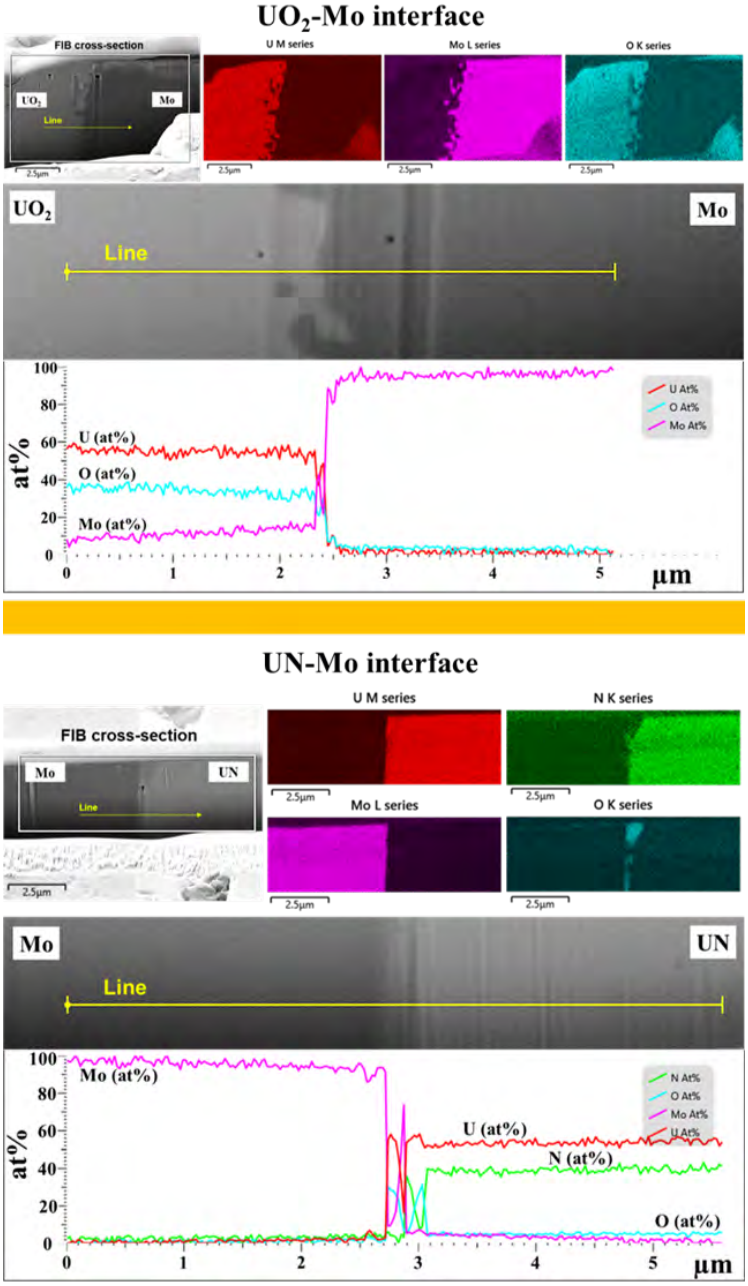

Figure 3.6: FIB cross-sections at the UO_2-Mo (top) and UN-Mo (bottom) interfaces, showing the EDS qualitative chemical maps of U, Mo and O, as well as line measurements across the interfaces.

3.3 Encapsulated spheres

This section will present the main results described in Papers IV, V and VI. Initially, ZrN and steel spheres were used as surrogates for UN spheres to develop the powder, CVD and PVD coating methods. Then, UN spheres were encapsulated by the developed methods.

3.3.1 Powder-coated spheres

Mo or W nanopowders were used to coat surrogate ZrN spheres to develop the powder coating methodologies and avoid generating nuclear scraps (Papers IV and V). Based on these results, W or Mo nanopowders were used to encapsulate UN spheres (Paper VI).

Fig.3.7 reports the morphology of the pre-sintered Mo/ZrN and W/ZrN spheres, with the Mo(binder)-coated sphere showing the roughest surface. Both Mo- and W-coated samples had particles connected by necks formed during the pre-sintering step at 1373 K, which is characteristic of initial sintering stages [84, 98–102]. The Mo(wet)/ZrN and Mo(binder)/ZrN morphologies are similar to those presented in a previous study on sintering Mo nanopowders in H_2 [99]. In the study, the authors report that a quenched micrograph of a sample sintered at 1273 K had a density of ∼53 %TD, with the microstructure corresponding to the initial-stage sintering. Another study shows similar microstructures of Mo compacts sintered by SPS at 1273 K (∼65 %TD) and 1373 K (∼75 %TD) in H_2 [100].

As mentioned in the Methodology section, W nanopowder did not adhere well to the spheres by the wet method (details in Paper IV). Thus, only the binder method is shown for W in Fig.3.7. Similarly to Mo, W showed connected particles and a porous structure due to the heat treatment at a moderate temperature (1373 K). This structure is also observed when W powder was sintered at 1473 K by conventional sintering (68 %TD) and SPS (67 %TD) in vacuum [101].

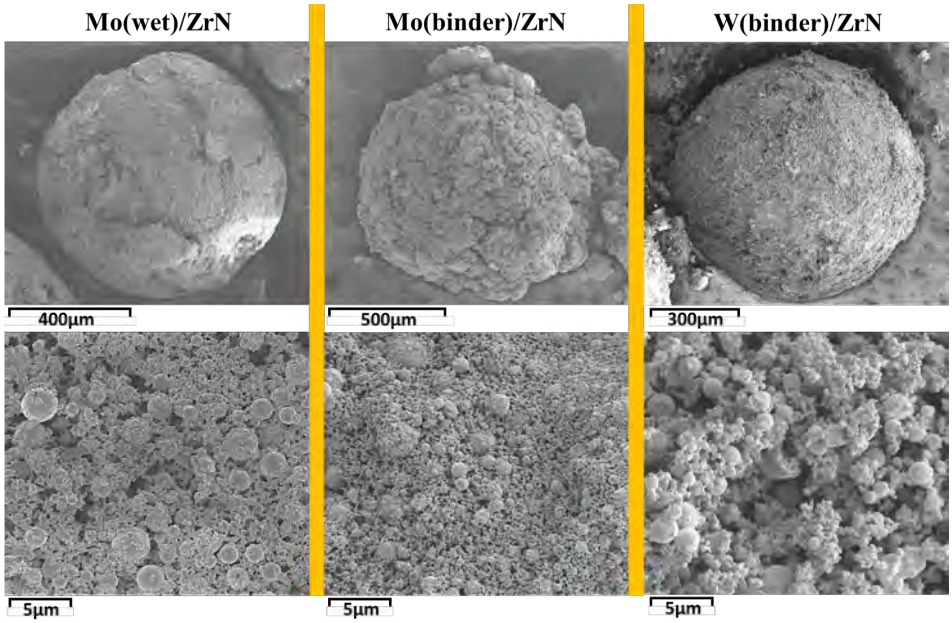

Figure 3.7: Morphology of the Mo(wet)/ZrN, Mo(binder)/ZrN, and W(binder)/ZrN encapsulated spheres. These samples were pre-sintered at 1373 K for 1 h in Ar to enhance the particle-particle bonding, adherence onto the spheres, and to remove the binding agent.

Based on the results with ZrN, UN spheres were coated with Mo or W nanopowders by the same binder methodology. Fig.3.8 reports the morphologies of the as-encapsulated UN spheres after the pre-sintering step. The uncoated UN spheres have a porous structure with a density of about 65 %TD and an average diameter of approximately 1000 μm. The Mo-coated sample has a porous structure with particles connected by the necks formed during the pre-sintering step at 1337 K. This observation agrees with a previous study on the sintering of Mo nanopowders in H_2 [99], where a quenched micrograph of a sample sintered at 1273 K has a density of approximately 53 %TD. Another study also shows similar morphologies of Mo compacts with about 65 %TD and 75 %TD when sintered at 1273 K and 1373 K in H_2, respectively [100].

The W-coated sample in Fig.3.8 has a smoother macroscopic surface than the Mo-coated sphere and a similar porous and particle-connected structure, which suggests that the developed methodology of coating spheres with Mo or W nanopowders is reproducible. A previous study on W powder sintered at 1473 K by conventional sintering (68 %TD) and SPS (67 %TD) also shows a porous structure with agglomerates [101].

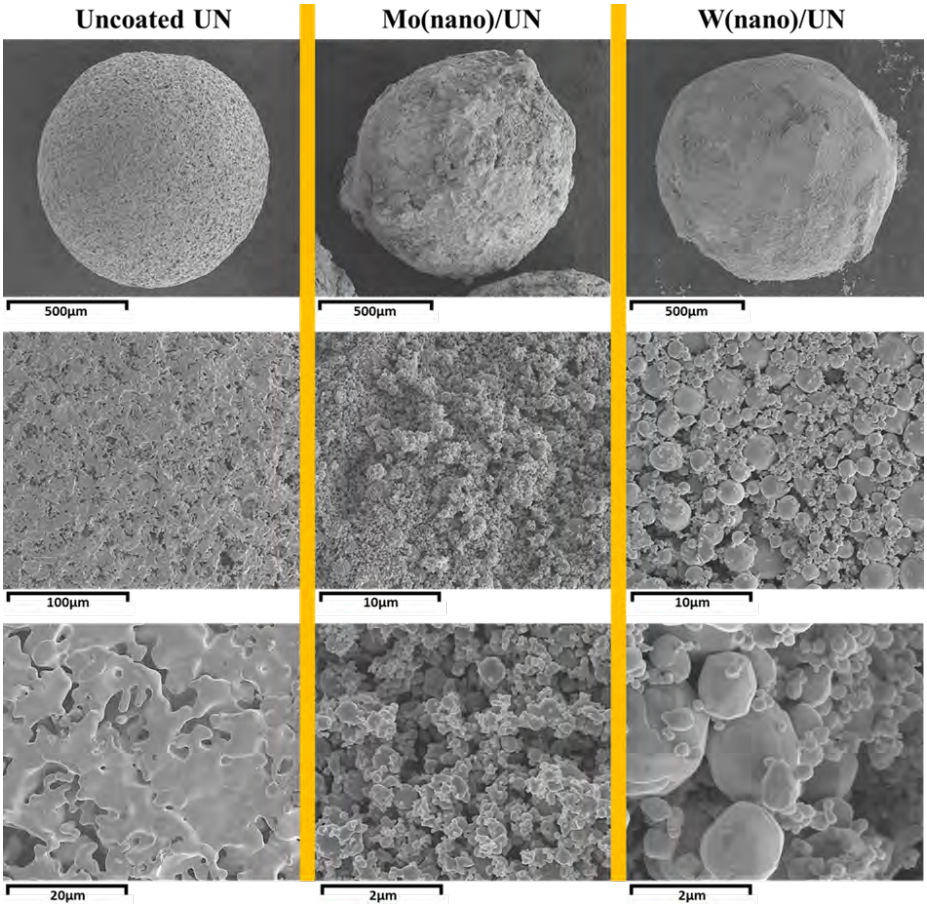

Figure 3.8: SEM images of uncoated and powder-coated UN spheres after the pre-sintering step at 1373 K for 1 h in Ar. UN spheres have a porous structure with a density of about 65 %TD and an average diameter of approximately 1000 μm. Both Mo- and W-coated spheres have porous structures with particles connected by the necks formed during the heat treatment.

3.3.2 CVD-coated spheres

Fig. 3.9 shows the morphology and EDS and EBSD maps of the CVD-W coated surrogate sample, named W(CVD)/ZrN. The SEM image of the unmounted sample reveals that W covered the whole surface, including pores and cracks. The highest magnification image exemplifies the dense and smooth layer of tungsten, which is characteristic of this method [103–105].

Both regular and FIB cross-sections portray a dense and well-adhered layer of

~3 μm that infiltrated via open porosity. The chemical distributions of fluorine show that F was trapped in the pores and inner regions during the growth of the W layer. Further studies are needed to optimise the methodology and avoid this contamination, since it may contribute to pellet-cladding interaction (PCI) and stress corrosion cracking (SCC) in a real fuel [106]. The EBSD map reveals polycrystalline W grains with (mostly) a columnar structure without preferential crystallographic grain orientation, as also observed in [103–105, 107–110].

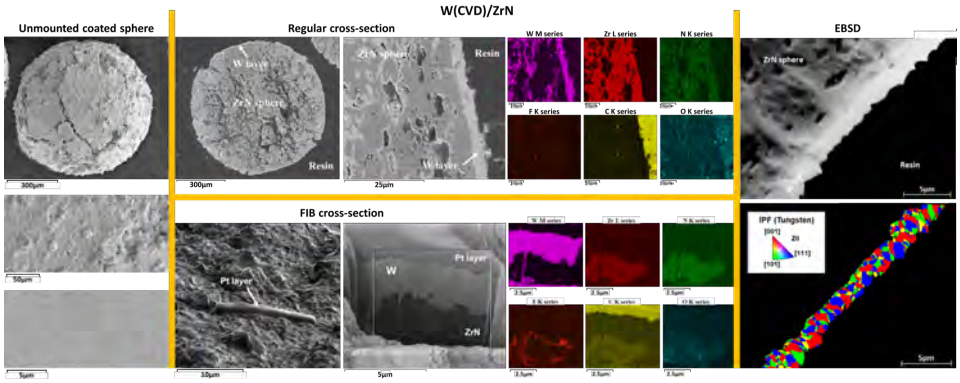

Figure 3.9: SEM, EDS and EBSD images of W(CVD)/ZrN showing a smooth and dense coating layer of about 3 μm that infiltrated via open porosity. The EDS maps reveal that F was trapped in the pores and inner regions of the W layer. EBSD image shows polycrystalline W grains with (mostly) columnar structure without preferential crystallographic orientation.

The results regarding UN spheres encapsulated by CVD of W are not included in this thesis due to time constraints, as well as additional work to export and process nuclear materials in a non-nuclear industry in the UK. But these ongoing experiments will be presented and discussed in the final version of Paper VI.

3.3.3 PVD-coated spheres

Fig.3.10 reports the cross-sections of PVD-coated surrogates (steel spheres), and the SEM-EDS maps of Fe, U, Mo, W, O and C. PVD of Mo provided a uniform and dense layer of 1.0 $\pm$ 0.1 μm, but with cracks at the interface with the steel spheres. Interfacial delamination can occur in PVD of Mo due to residual stresses and poor adhesion on the substrate [111]. Moreover, the process parameters used during deposition alter the kinetic energy of the sputtered Mo particles and affect microstructural properties such as crystal structure, grain orientation, surface morphology, microstrain, and growth rates of Mo layers [111–115]. The EDS chemical maps of Mo and O show a dense coating layer of molybdenum metal without detecting oxygen, which is a contaminant in the steel spheres and resin.

The tungsten layer is also uniform and has a thickness of 4.0 ± 0.3 μm, but its morphology is not as dense as the molybdenum layer. Tungsten agglomerated and formed particles onto the spheres with cracks at the interface. Crystal structure, grain sizes, surface morphology, residual stress, delamination, and crack behaviour are affected by the processing parameters used for sputtering tungsten on a substrate [116–118]. For instance, for a fixed power of 100 watts, finer particles and smother surfaces are obtained when the pressure of the sputtering inert gas increases [118]. The EDS maps of W and O show a uniform layer with oxygen as a contaminant, also observed in the steel spheres.

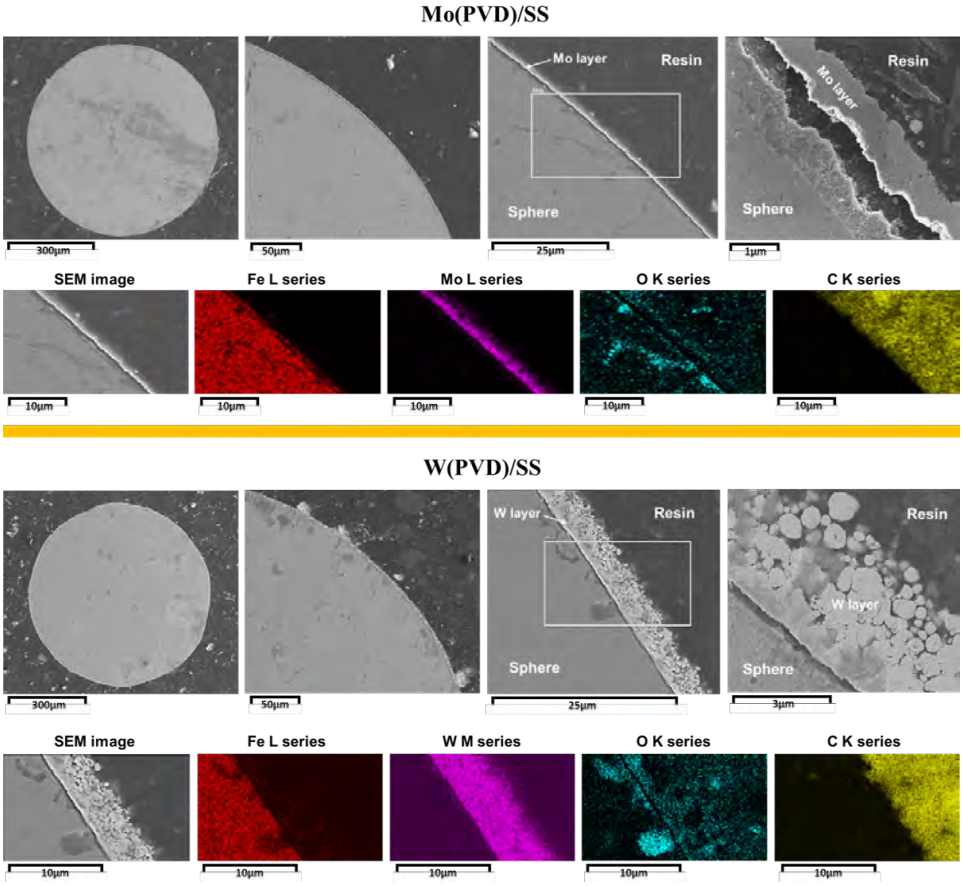

Figure 3.10: SEM images of PVD-coated steel spheres (SS). Mo(PVD)/SS images (top) show a uniform and dense Mo layer of 1.0 ± 0.1 μm, but with cracks at the interface. The W layer in W(PVD)/SS (bottom) is also uniform with a thickness of 4.0 ± 0.3 μm, but it is not as dense and pure as the molybdenum layer.

Uranium nitride spheres were encapsulated with Mo after the development process using steel spheres. The SEM images and FIB cross-sections of Mo(PVD)/UN are shown in Fig. 3.11. It is observed in the SEM images (on the left) that Mo adhered to the carbon tape while the sphere was positioned for analysis. This delamination is observed and characterised by the scotch tape test in previous studies [111, 113, 114]. The adhesion of Mo thin films is a complex function of the deposition power, deposition pressure, and residual stresses [111,113]. For instance, thin films prepared at an argon pressure of 1.50 mTorr (20 mbar) were under compressive residual stress and failed during the tape test, and the ones deposited at 9.23 mTorr (1.23 mbar) passed [111]. Other authors report delamination at an operating pressure of 0.88 Pa (0.88 mbar) and not in the range 1.33-2.66 Pa [113].

The highest magnification SEM image of the PVD-Mo coating in Fig. 3.11 (left) shows a rough surface with coarse grains. Similarly to the delamination behaviour, structural and morphological properties of Mo thin films depend on the sputtering conditions, such as deposition power, pressure, temperature and rate [111–115]. As a general rule from previous results, denser and smother surfaces are deposited at higher power, lower pressure, higher substrate temperature, and lower deposition rate. Ongoing experiments at SCK CEN aim to achieve smoother and better adhered Mo layers.

Fig. 3.11 (right) shows a FIB cross-section and an EDS spot analysis of the as-encapsulated Mo(PVD)/UN sphere. A Mo layer of about 500 nm covered the porous structure of the sphere. From previous results (Papers II and III), a layer of 0.5 μm would be enough to avoid interactions between UN and UO_2 during sintering. However, as observed in the EDS spot analysis, the sample was contaminated with W. As described in Section 2.2.3 (Physical vapour deposition), the procedure at SCK CEN is qualified to coat 2000 g of material. Since the UN batches were approximately 10 g each, it was needed to use a filler to provide a uniform coating layer on such small batches. Thus, the filler used to coat the previous sample (W(PVD)/SS) delaminated while coating the UN spheres with Mo and contaminated the surface. To avoid this issue, a process to coat small batches is under development, and the ongoing experiments will be presented and discussed in the final version of Paper VI. Regardless of the contamination issue, the results show good adherence and uniformity of the Mo layer onto UN, as seen in the regions where the arrows are pointing. Therefore, it was possible to encapsulate UN spheres with Mo using the designed PVD coater at SCK CEN.

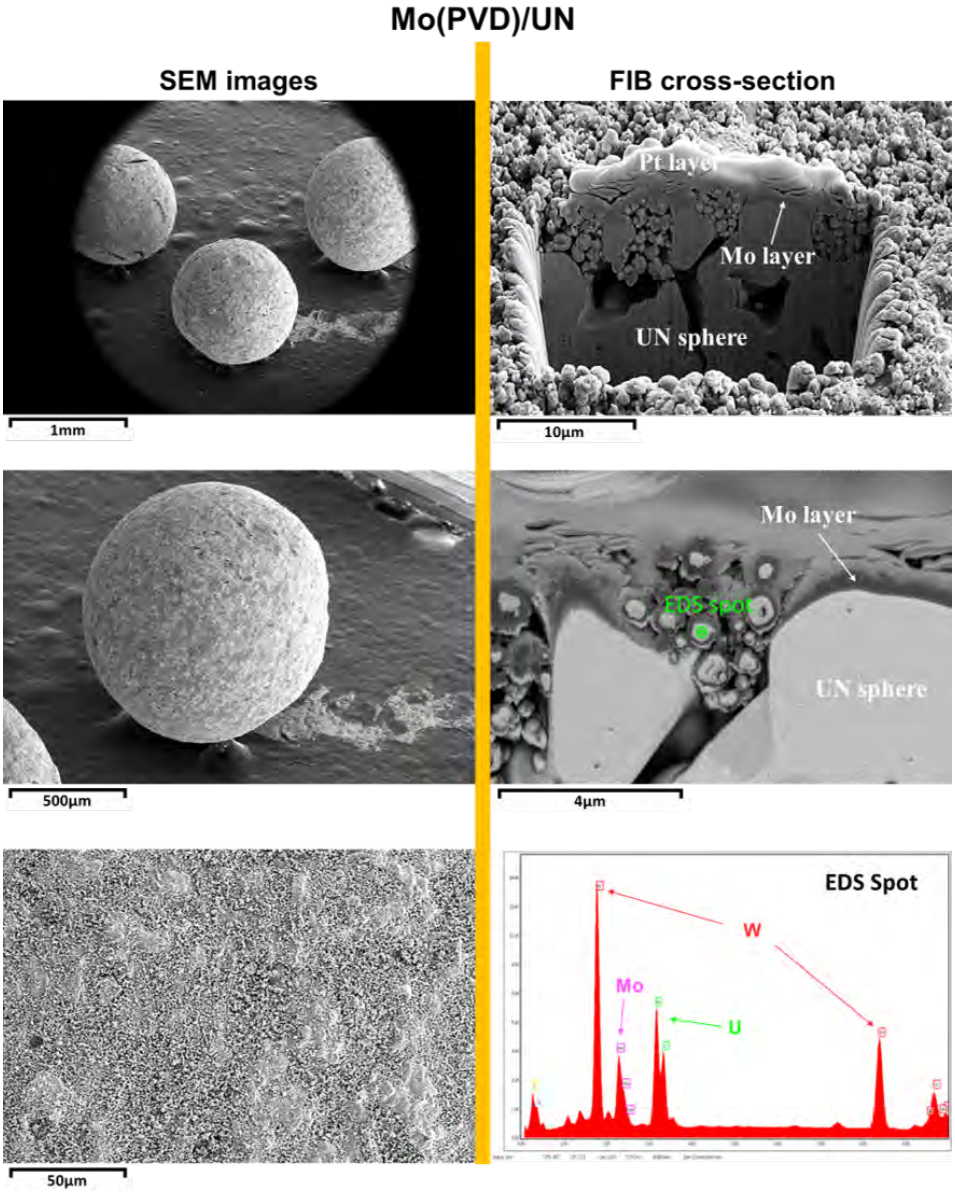

Figure 3.11: SEM-EDS and FIB analyses of UN spheres encapsulated with Mo by the designed PVD apparatus at SCK CEN. A Mo layer of about 500 nm covered the porous structure of the sphere, which was contaminated with W from a previous deposition.

3.4 Encapsulated UN-UO_2 accident tolerant fuel

This section will describe the main results reported in Papers V and VI, where surrogate and UN spheres encapsulated with Mo or W by different coating methods were used to fabricate composite fuels.

3.4.1 Encapsulated surrogate-UO_2 composite fuel

Encapsulated surrogates were fabricated using approximately 15 wt% of coated ZrN or steel spheres and $UO_{2.13}$ powder from Westinghouse. The mixtures were consolidated by SPS and prepared for characterisation. First, the composites containing powder-coated spheres will be presented, followed by the composites with CVD- and PVD-coated spheres.

3.4.1.1 Powder-coated surrogate fuel

Fig.3.12 shows the SEM images and EDS maps of the powder-coated fuels. The Mo(wet)/ZrN-UO_2 sample had a dense and non-uniform Mo layer with a sharp interface between Mo and UO_2. The EDS map of Mo shows that a Mo layer of about 20 μm covered the spheres, with thicker regions at the porosity and cracks on the surface. Moreover, the Mo and O maps demonstrate that the Mo particles sintered and became a dense Mo layer with no interaction with the UO_2 phase. This result agrees with the pressure-assisted diffusion experiment of the UN-Mo-UO_2 system in Paper III.

The EDS maps of Mo(binder)/ZrN-UO_2 in Fig.3.12 show a thicker Mo layer ($\sim$65 μm) than the wet method ($\sim$20 μm). Additionally, no C contamination from the binder agent is observed in the coating layer. As in the wet method, the coat was dense, non-uniform and without interactions with UO_2. This denser structure, compared with the pre-sintered spheres in Fig. 3.7, confirms that the porous structure densified during SPS (>95 %TD), as previously reported under similar sintering condictions [98–100, 119].

SEM-EDS images of W(binder)/ZrN-UO_2 in Fig. 3.12 report a dense, inert, and non-uniform W coating layer of $\sim$12 μm. Similarly to the Mo-coated composites, the porous coat of the pre-sintered W(binder)/ZrN spheres (Fig. 3.7) was densified to a higher density during SPS. Previous studies under similar conditions reported sintered densities >95 %TD [120–123].Thus, the pre-sintered W layer was densified to (at least) 95 %TD after SPS at 1773 K and 80 MPa. However, some regions in both Mo(wet and binder)/ZrN-UO_2 and W(binder)/ZrN-UO_2 composites were not encapsulated properly by the powder coating method. Further studies are encouraged to improve the methodology in order to obtain thinner and full-encapsulated spheres.

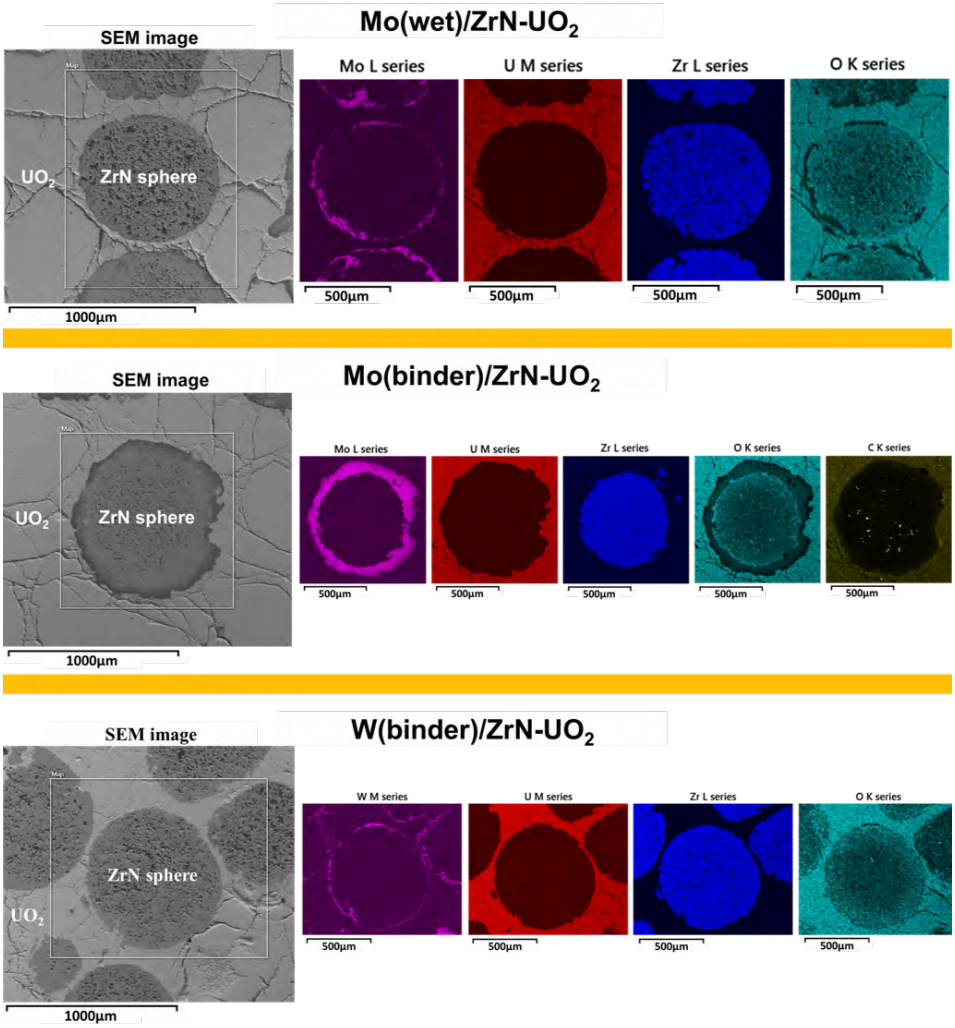

Figure 3.12: Powder-coated ZrN-UO_2 surrogate composites containing spheres encapsulated with Mo by the wet (top) and binder (middle) methods, and W by the binder (bottom) method.

3.4.1.2 CVD-coated surrogate fuel

SEM-EDS maps of W and F in Fig.3.13 indicate the infiltration of WF_6 during CVD, as observed in the as-coated W(CVD)/ZrN spheres in Fig. 3.9. At the interface, a dense, inert, and uniform W layer of $\sim$3 μm is observed. This result demonstrates that the W layer was dense and stable enough to keep its thickness

and sharpness, even after undergoing the most severe SPS conditions used in this thesis (1773 K and 80 MPa) (Paper I). Thus, in the ongoing experiments, the CVD method is used to coat the UN spheres. Then, an encapsulated UN-UO_2 accident tolerant fuel will be fabricated by SPS. These results will be included in the final version of Paper VI. Moreover, by using denser UN spheres and fine tuning some CVD parameters (e.g., H_2/WF_6 pressure ratio), the infiltration and trapping of F inside the spheres can be minimised [107, 124–126].

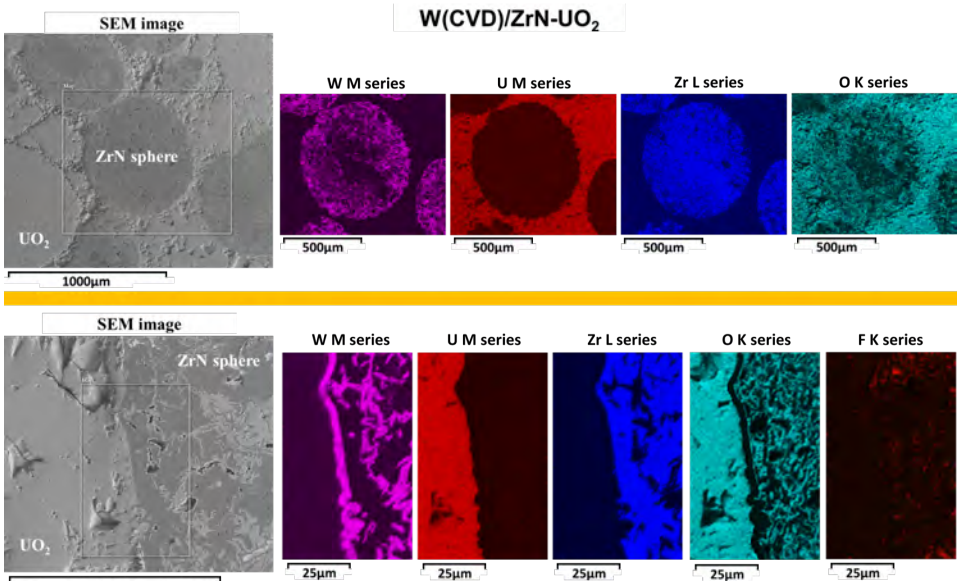

Figure 3.13: SEM-EDS images of W(CVD)/ZrN-UO_2 showing infiltration of WF_6 via open porosity and cracks in the spheres. A dense, inert, and uniform W layer of ∼3 μm was obtained by CVD and maintained after SPS.

3.4.1.3 PVD-coated surrogate fuel

Fig.3.13 reports the SEM images and EDS maps of Mo(PVD)/SS-UO_2 (top) and W(PVD)/SS-UO_2 (bottom). The PVD-coated layers of Mo and W in the composites were 0.9 ± 0.2 μm and 5.7 ± 1.0 μm, respectively, which are approximately the same as in the as-encapsulated samples (Fig. 3.10). The surrogate spheres deformed, along with the coating layers, more than the UN spheres due to induced plastic deformation and densification under uniaxial loads and high current during SPS [66, 67]. The cracks in both layers may have resulted during cooling due to severe deformation of the steel spheres, which might have acted as diffusion paths for O and Fe through the coatings. This interdiffusion behaviour may be the mechanism for the Fe- and O-rich zones within UO_2, observed in the EDS maps. Oxygen

is also observed in W but not in Mo, indicating that W acts as an oxygen gatherer and Mo as a diffusion barrier.

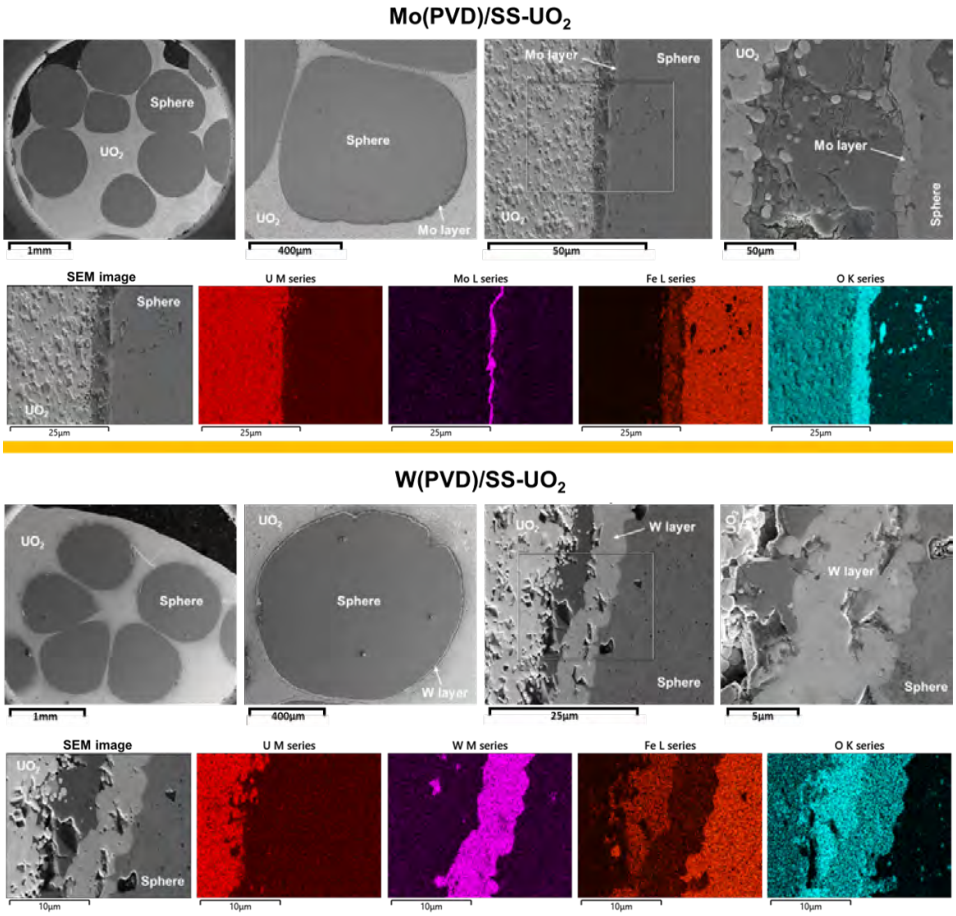

Figure 3.14: SEM images and EDS maps of cross-sections of Mo(PVD)/SS-UO_2 (top) and W(PVD)/SS-UO_2 (bottom) surrogate composites. The PVD-coated layers of Mo and W were 0.9 ± 0.2 μm and 5.7 ± 1.0 μm, respectively, without observable interactions with UO_2.

The results with PVD-coated surrogate spheres are promising and potentially applicable to UN spheres. In the case of UN, dense and pure Mo and W layers with fewer cracks are expected to be obtained since the UN spheres deform less during SPS (Papers I, IV, and VI). Ongoing work at SCK CEN on PVD coating of Mo and W onto UN spheres will be used to fabricate encapsulated (Mo(PVD) or W(PVD))/UN-UO_2 accident tolerant fuels by SPS. These results will be reported and discussed in the final version of Paper VI.

3.4.2 Encapsulated UN-UO_2 composite fuel

The cross-sections and EDS chemical maps of the encapsulated UN-UO_2 composite fuels are shown in Fig.3.15. UN spheres were coated by the developed powder (binder) method. The lower magnification images of Mo(nano)/UN-UO_2 reveal a dense and non-uniform Mo layer of 28 $\pm$ 14 μm, which is thinner and smoother than the encapsulated ZrN-UO_2 surrogate fuels (Fig. 3.12). Additionally, the UN spheres deformed during SPS along with the Mo layer, as discussed in Paper I. Some spheres were fully covered, but there were regions without Mo. This issue might be due to contact points between UN spheres, which might have impaired the powder to cover the spheres, or while handling the as-coated spheres and transferring them for the pre-sintering process (Fig. 2.9). The higher magnification images at the interface reveal both intergranular and transgranular cracking on the Mo layer, which may be due to compressive stress, the presence of impurities at the grain boundaries, grain boundary misorientation, and dislocation pileups and plastic strain incompatibilities [127–130].

The EDS map of Mo in Fig.3.15 reveals a dense, pure, and well-adhered Mo layer. This result confirms that the porous Mo layer, obtained after the pre-sintering step at 1373 K (Fig. 3.8), was densified during SPS at 1773 K and 80 MPa. The spots of an N-rich phase in the UO_2 matrix represent sesquinitride (α-U_2N_3) precipitates, which result from the interactions between uncoated regions of UN and UO_2 powder during sintering (Paper I).

Similarly to Mo(nano)/UN-UO_2, the lower magnification images of W(nano)/UN-UO_2 in Fig.3.15 portray fully covered and slightly deformed spheres with a dense and non-uniform W layer of 32 $\pm$ 21 μm. This coat evidences that the porous and pre-sintered W(nano)/UN structure (Fig. 3.8) was densified by SPS at 1773 K and 80 MPa, which agrees with the surrogate composites and previous studies on SPS of W nanopowder [120–123]. The EDS map of W also demonstrates a dense and pure W layer, while the N map shows lamellae of α-U_2N_3 in UO_2 due to interactions between uncovered UN (from another region) and UO_2 during fabrication. This microstructure suggests that there were more uncoated areas in W(nano)/UN-UO_2 than in Mo(nano)/UN-UO_2 since the amount of sesquinitride is proportional to the amount of uncoated UN (Paper I).

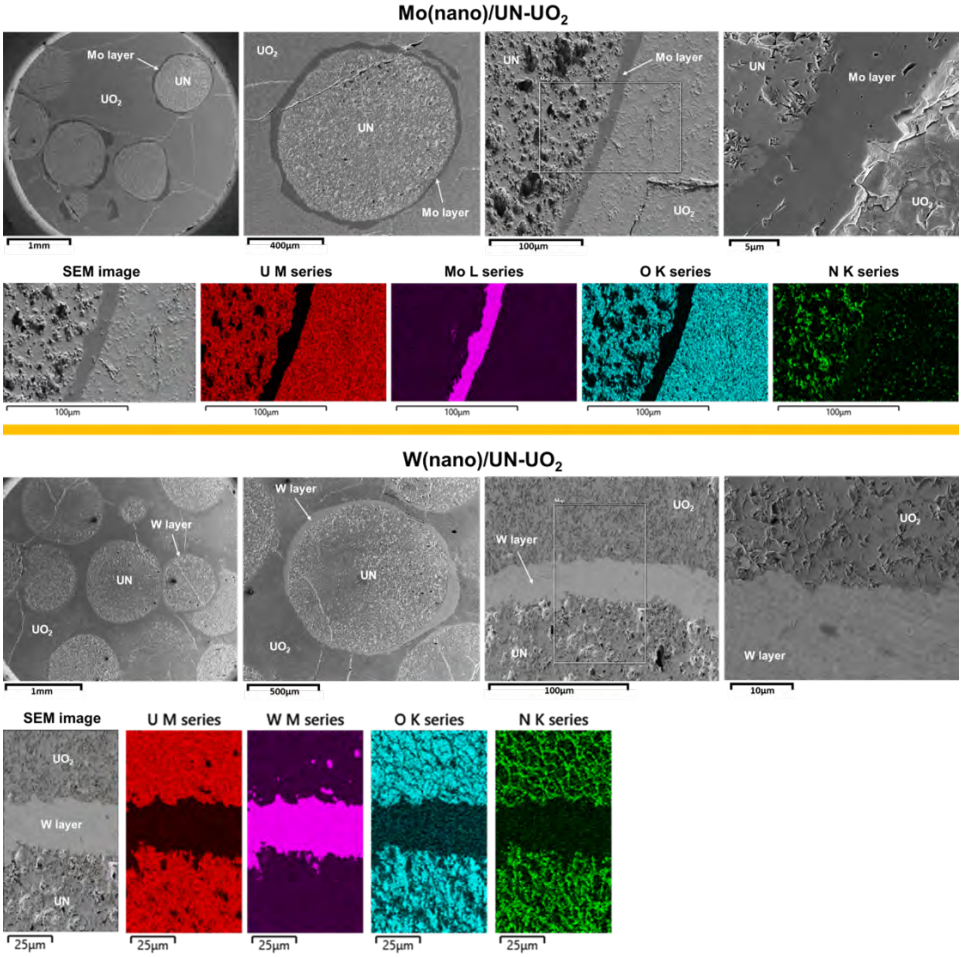

Figure 3.15: SEM-EDS maps of the encapsulated Mo(nano)/UN-UO_2 (top) and W(nano)/UN-UO_2 (bottom) accident tolerant fuels. The images show dense, pure, and non-uniform layers of Mo (∼28 μm) and W (∼32 μm) with no interaction with UN and UO_2. N-rich regions in the UO_2 matrix in both samples indicate the formation of α-U_2N_3 due to interactions between uncoated UN regions and UO_2 during sintering (Paper I).

3.5 Oxidation resistance of the composite fuels

This section will present the oxidation of uncoated UN-UO_2 composites in synthetic air up to 973 K. These experiments aimed to evaluate the effectiveness of UO_2 as an oxidation barrier for the nitride phases, as reported in detail in Pa-

per VII. In summary, thermogravimetric investigations (TGA/DSC) of uncoated UN-UO_2 composite fuels, sintered at 1773 K and 80 MPa for 3 min (91-97 %TD), were performed in triplicate to assess the mass variations (%), oxidation onset temperatures (OOTs), and maximum reaction temperatures (MRTs). The composites selected for this purpose were UN(10)-UO_2 (FC), UN(30)-UO_2 (SC), UN(30)-UO_2 (FC), UN(50)-UO_2 (FC), where the numbers in parenthesis represent the initial weight fractions of UN spheres added (wt%), and SC and FC are the slow and fast cooling profiles using to fabricate the composites, respectively. More details regarding sample nomenclature, SPS parameters, and weight fractions of each phase in the sintered composites are found in Table 2.2 and Fig. 3.1.

Figs. 3.16(a) and (b) show the influence of the amount of UN spheres (wt%) on the oxidation behaviours, while Figs. 3.16(c) and (d) illustrate the impact of the cooling rates. The results show that the higher the initial UN content, the higher the total weight variation. This increment is also affected by the presence of α-U_2N_3 in the composites. The total amount of UN plus α-U_2N_3 in UN(10)-UO_2 (FC), UN(30)-UO_2 (FC), and UN(50)-UO_2 (FC) were 5.0 wt%, 26.6 wt% and 46.2 wt%, respectively.

Since the FC profile resulted in a higher amount of nitrides in UN(30)-UO_2 (FC) (26.6 wt%) than in UN(30)-UO_2 (FC) (20.2 wt%), the weight variation was higher in the former. The cooling rate did not affect the onset temperatures significantly but caused a reduction of MRT when the composite was cooled faster. This reduction is due to a higher amount of nitrides present in the fast-cooled sample.

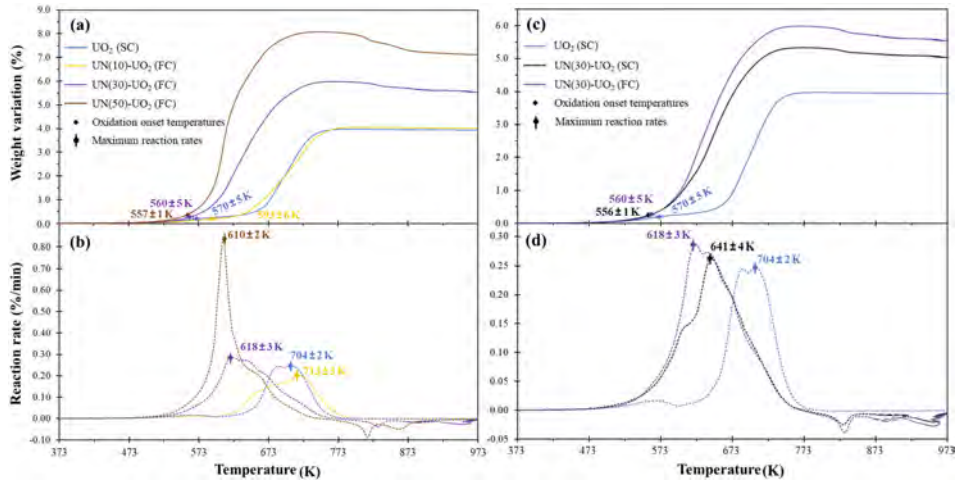

Figure 3.16: Influence of the initial amount of UN microspheres (wt%) (a, b) and cooling rates (c, d) on the oxidation kinetics. The higher the initial UN content, the higher the total weight variation and the lower the MRTs and OOTs. A faster cooling profile resulted in a higher weight variation and lower MRT but similar OOT.

Fig. 3.17 shows TGA and DSC results of UN(50)-UO_2 (FC), together with normalised TGAs of UO_2 (SC) and UN spheres obtained from Paper VII. The data for the composite fuel show two linear kinetic regions (TGA), associated with exothermic peaks (DSC), at 573-650 K and 660-685 K.

Based on the presented results and previous studies [50, 131–135], a mechanism for the oxidation of UN/U_2N_3-UO_2 composites in three steps is proposed. First, the oxidation starts at the external surface of UO_2 with an incubation time, at which a fine layer of U_3O_7 is formed at lower temperatures (< 523 K) [50, 131]. This layer increases until reaching a critical thickness ($\sim$400 nm) and then spalls from UO_2 as powder, generating cracks and exposing fresh UO_2 regions. These cracks can be associated with a stress state created by U_3O_7 on UO_2, since U_3O_7 has a smaller lattice parameter than UO_2 [133]. Afterwards, the oxidation reaction continues via UO_2 grain boundary attack with simultaneous cracking and nucleation of U_3O_8 via linear kinetics, which depends on the rate of macro-cracking of the U_3O_7 critical layer [50, 132–134]. Second, the α-U_2N_3 phase presents along and inside the UO_2 grains (Fig. 3.3, and Papers I and VII) starts to oxidise simultaneously to the nucleation of U_3O_8 and grain boundary attack, during the first linear region. Finally, the embedded UN spheres oxidise and result in a severe exothermic peak during the second linear region [135].

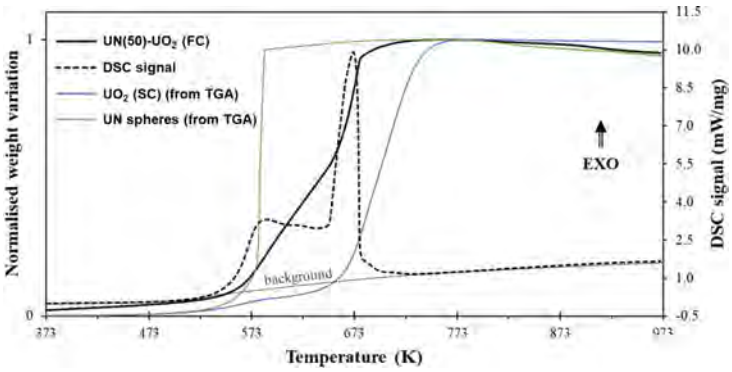

Figure 3.17: DSC analysis of UN(50)-UO_2 heated at 5 K/min up to 973 K at 40 mL air/min. Normalised UO_2 (SC) and UN microspheres weight variations (from TGA experiments in Paper VI) are plotted as illustrative references. The data shows two linear kinetic regions associated with exothermic peaks at 573-650 K and 660-685 K. Additionally, the UO_2 matrix reduced the severity of the oxidation reaction and retarded the oxidation of the nitride phase.

Fig. 3.18 shows the oxidised microstructures of as-fabricated and oxidised UN-UO_2 composite fuels. In general, the oxidised fuels showed a corroded surface with intergranular cracking and spalling, and some intragranular cracks originated from the oxidation of the sesquinitride phase within the UO_2 grains. Ex-situ SEM examinations are not ideal to have a complete visualisation of how the oxidation

reactions evolved. In-situ oxidation analyses of UO_2 fuel demonstrate two types of cracks [133]: macro-cracks at the grain boundaries after 30 min of isothermal oxidation, followed by micro-cracking at the cracked surfaces, which enhanced spallation. The authors also show that the sample was still oxidising when the pellet was completely cracked with a constant weight variation, i.e., no more reactive surfaces were created. At this final stage, nucleation and growth of U_3O_8 proceeded until the total consumption of the UO_2 phase.

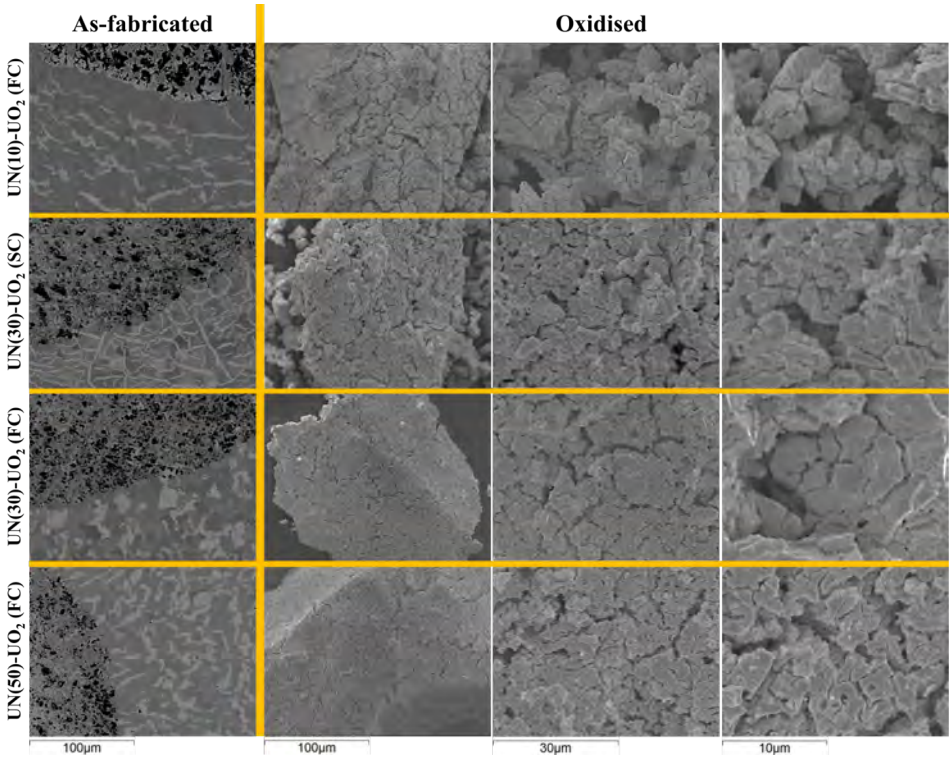

Figure 3.18: Micrographs of as-fabricated and oxidised UN(10)-UO_2 (FC), UN(30)-UO_2 (SC), UN(30)-UO_2 (FC), and UN(50)-UO_2 (FC) composite fuels. All the oxidised morphologies had a corroded surface with mostly intergranular cracking and spalling, with some intragranular cracking as well.

The results described in this section indicate that the UO_2 matrix retards and smooths the oxidation of the nitride phases present in the composites, even when the initial amount of UN spheres was as high as 50 wt% (Fig. 3.17). However, only UO_2 is not enough to make UN waterproof. A coating layer would enhance even more the oxidation resistance of UN in air. The ongoing experiments on the oxidation of encapsulated UN-UO_2 composite fuel pellets will be presented and discussed in the final version of Paper VI.

3.6 Thermal fuel performance

Fig. 3.19 shows the thermal conductivity profiles as a function of temperature for uncoated and encapsulated UN-UO_2 accident tolerant fuels containing 10, 30, 50, and 70 wt% of uncoated and Mo- or W-coated UN spheres. For the calculations, it was considered that the UN spheres do not interact with the coating layers nor with the UO_2 matrix, even though it is not the case for the uncoated spheres (Paper I). The results suggest that the thermal conductivity of the composite increases as the amount of uncoated or coated UN (wt%) increases due to the higher thermal conductivity of UN, when compared to UO_2. The values for the fuels with 10, 30, 50, and 70 wt% are approximately 1.5, 1.8, 2.7, and 5.7 times higher than that of the UO_2 reference at 2000 K. Additionally, at higher UN contents (i.e., 50 and 70 wt%) and lower temperatures (< 500 K), the thermal conductivity of the encapsulated composites exceeds that of pure UN independent of the coating material, but with UN-W-UO_2 having a slightly higher thermal conductivity than UN-Mo-UO_2. No significant difference was observed when the coating thicknesses varied from 1 μm to 5 μm, for the 70 wt% cases coated with W and Mo.

A previous study reports the change in thermal conductivity of high-density UN(10, 30, 50 wt%)-UO_2 composites sintered by hot pressing at 1863 K [47]. The authors also considered no interactions between UN and UO_2 during sintering to perform the thermal diffusivity experiments. Thus, the α-U_2N_3 phase was included in the UO_2 phase and the composites were considered a simple mixture of UN and UO_2 due to limited data on the thermophysical properties of α-U_2N_3 and its relative small fraction in the composites (≤ 4.8 wt%). The results show that the thermal conductivity of the composites increased remarkably with the increase in the UN content (wt%), with the UN(39.3 wt%)-UO_2(60.7 wt%, including α-U_2N_3) having an increase in uranium density by 13 % and thermal conductivity of up to 100% at 1073 K. This composite pellet was fabricated using initially 70 wt% of UN and, after sintering, the weight fractions of UN, α-U_2N_3, and UO_2 were 39.3 wt%, 3.0 wt% and 57.7 wt%, respectively. Therefore, these experimental results demonstrate that the UN fuel increases the uranium density and thermal conductivity of the standard UO_2 fuel.

Thermal diffusivity measurements are suggested to evaluate the thermal conductivity of encapsulated UN-UO_2 ATF composites and validate the FEM results presented in Paper VIII.

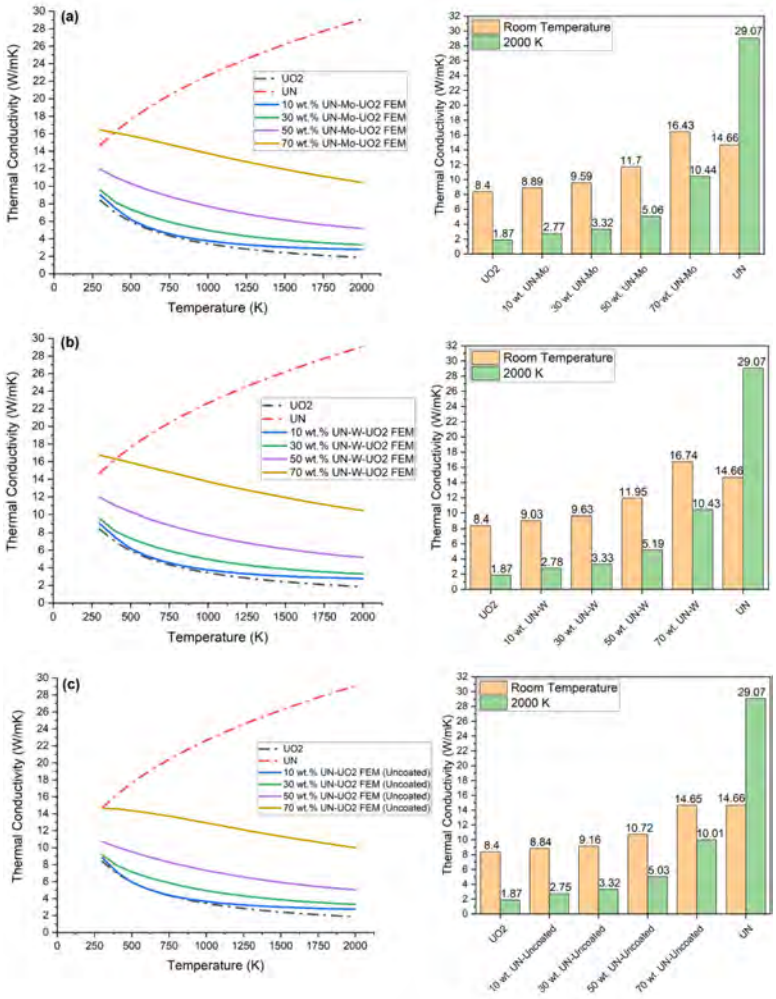

Figure 3.19: Thermal conductivity of the composite fuels encapsulated with (a) Molybdenum, (b) Tungsten, and (c) Uncoated UN-UO_2 as a reference. The addition of UN increases the thermal conductivity of the fuel pellets.

The results in Fig. 3.20 and Fig. 3.21 indicate that encapsulated UN-UO_2 fuels with higher U density may provide higher thermal conductivity, decreased fuel centreline temperatures, and reduced radial thermal gradients during normal operation. Thus, FEM indicates that the fuel centreline temperature may be reduced by more than 400 K when 70 wt% of encapsulated UN spheres are used as compared to the reference UO_2. These improvements would increase the margin to fuel melting and to loss of fuel integrity during normal reactor operations and off-normal conditions.

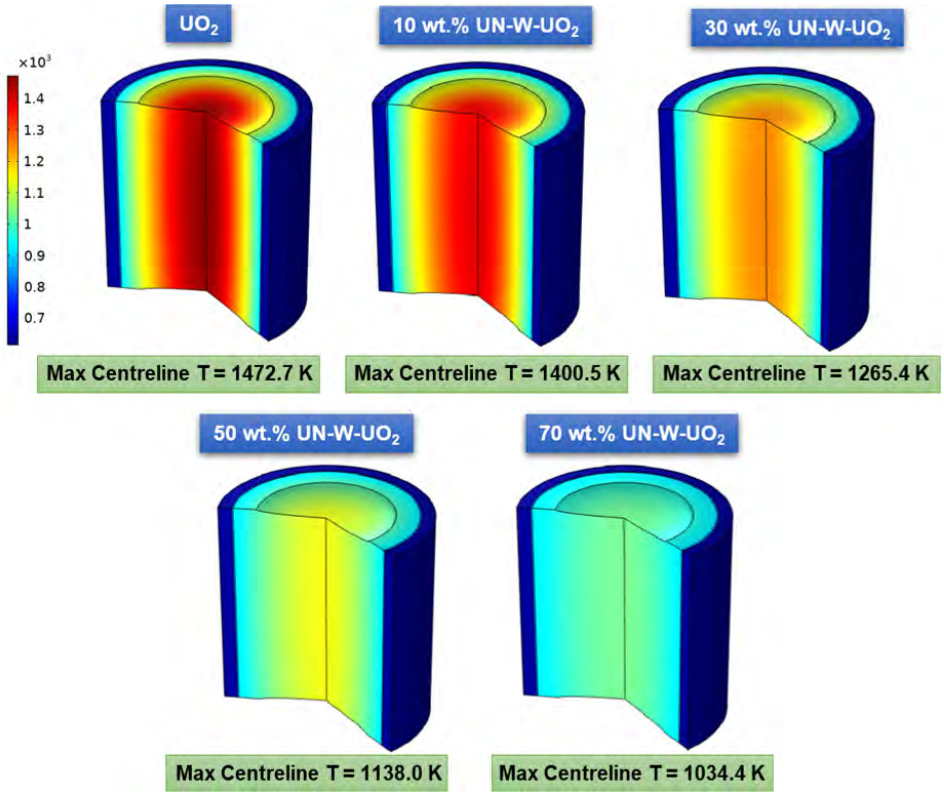

Figure 3.20: 3D temperature profiles showing that the fuel centreline temperatures decrease with the addition of encapsulated UN additives.

A combination of a higher uranium density and enhanced thermal properties would allow the exploration of advanced cladding materials, such as FeCrAl alloys and Cr-coated cladding, without sacrificing the resulting neutron economy in the reactor. In this regard, full-scale neutronic analysis of the encapsulated fuels is encouraged to estimate the effect of higher uranium densities on the neutron economy. Furthermore, it is worth mentioning that all FEM analyses represent steady-state simulations without considering any time-dependent phenomena. Thus, future work should consider time-dependent thermomechanical simulations of normal operation and accident scenarios, including the He-gap conductance variation over time, swelling, and fission gas release effects.

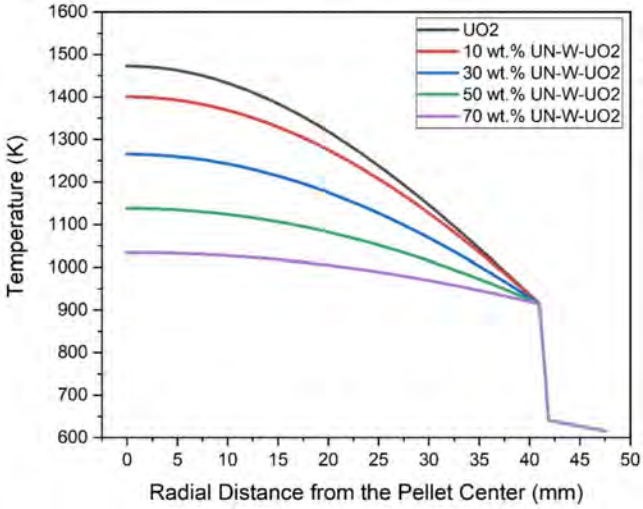

Figure 3.21: Radial temperature profiles of encapsulated UN-W-UO_2 composite fuels and the UO_2 reference. The addition of W-coated UN spheres decreases the centreline temperatures and thermal gradients in the pellets.

Chapter 4

Conclusions and outlook

The main objective of this thesis was to expand the knowledge and ultimately promote the understanding of designing, fabricating, characterising, and evaluating an innovative accident tolerant fuel concept: encapsulated UN spheres as additives to the standard UO_2 fuel.

Several steps were proposed and accomplished to achieve this objective. First, it was desired to understand the formation mechanism of the α-U_2N_3 phase that can form when UN and UO_2 are interacting and, consequently, to know how the sintering parameters affect the amount, size and morphology of the sesquinitride phase. Second, potential coating candidates within the refractory metals group that can hinder the unwanted UN/UO_2 interaction were investigated and tested by combining modelling and experimental results. From both studies, molybdenum and tungsten were shown to be the most promising coating candidates. Third, feasibility studies and the development of three different coating methods were performed: powder coating, chemical vapour deposition, and physical vapour deposition of Mo or W onto surrogate spheres. Forth, based on the studies using surrogates, UN spheres were encapsulated by the powder coating methods using Mo or W nanopowders, followed by the sintering of encapsulated additive nuclear fuels. Additionally, UN spheres were encapsulated with molybdenum by PVD. Fifth, oxidation resistance experiments in air were carried out to understand the oxidation kinetics of uncoated composite fuels, as well as to analyse the influence of the UO_2 phase as an oxidation barrier for the nitride phases and propose an oxidation mechanism for the composite fuel pellets. Last, the thermal behaviours of uncoated and encapsulated composite fuels were estimated by finite element modelling, evaluating the influence of the amount of uncoated and encapsulated UN spheres, and the thickness and coating materials on the thermal conductivity and fuel centreline temperatures.

Based on the results presented in this thesis, encapsulated UN-UO_2 accident tolerant fuels were successfully fabricated by spark plasma sintering and evaluated. It was shown that the powder coating methods form thick, dense, and non-uniform

coating layers onto spheres, while the CVD and PVD methods provide thinner and more uniform layers. Finite element modelling indicates that the fuel centreline temperature may be reduced by more than 400 K when 70 wt% of encapsulated UN spheres are used as compared to the reference UO_2. the severity of the degradation of the nitride phase is reduced when embedded in a UO_2 matrix and may also be reduced even more by the presence of a coating layer.

Future research is needed to optimise the powder coating method and provide fully covered UN spheres with thinner and smoother layers. Additionally, other coating materials should be tested since it was demonstrated that both CVD and PVD are potential coating methods to encapsulate spheres with dense and uniform layers. Also, multilayered and alloyed coatings can be developed and tested using PVD, for instance. It is suggested to synthesise dense UN spheres and perform both oxidation experiments in steam and thermal diffusivity measurements to obtain experimental results to validate the finite element modelling results. Moreover, further developments on cold-pressed encapsulated UN-UO_2 fuels, followed by conventional sintering in a reducing atmosphere (Ar + 4% H_2), could be performed and the results compared to the fuels fabricated by SPS.

The work reported in this thesis contributes to further developments in methodologies for fabricating, characterising, and evaluating accident tolerant fuels within LWRs. Thus, the outcome of this study helps to address the current demand for research in the ATF context and provides real-world value to the fuel manufacturers and, consequently, the society in such advanced fuel design.

References

[1] P. C. Jain, "Greenhouse effect and climate change: scientific basis and overview," *Renewable Energy*, vol. 3, pp. 403–420, 1993.

[2] IEA, "Electricity Market Report 2023," Tech. Rep. 2023, International Energy Egency, February 2023.

[3] IAEA, "Energy, Electricity and Nuclear Power Estimates for the Period up to 2050," Tech. Rep. IAEA-RDS-1/42, International Atomic Energy Egency, September 2022.

[4] E. Heylen, G. Deconinck, and D. V. Hertem, "Review and classification of reliability indicators for power systems with a high share of renewable energy sources," *Renewable and Sustainable Energy Reviews*, vol. 97, pp. 554–568, 2018.

[5] IEA, "Nuclear Power in a Clean Energy System," Tech. Rep. 2019, International Energy Egency, May 2019.

[6] IAEA, "Nuclear Power Reactors in the World," Tech. Rep. IAEA-RDS-2/42, International Atomic Energy Egency, June 2022.

[7] WNA, "World Nuclear Performance Report 2021," Tech. Rep. 2021/004, World Nuclear Association, October 2021.

[8] D. Klein, M. Corradini, and *et al.*, "Fukushima Daiichi: ANS Committee Report," Tech. Rep. ANS2012, American Nuclear Society, March 2012.

[9] NEA, "State-of-the-Art Report on Light Water Reactor Accident-Tolerant Fuels," Tech. Rep. NEA No. 7317, Nuclear Energy Agency, October 2018.

[10] J. T. White, A. T. Nelson, J. T. Dunwoody, D. D. Byler, D. J. Safarik, and K. J. McClellan, "Thermophysical properties of U_3Si_2 to 1773 K," *Journal of Nuclear Materials*, vol. 464, pp. 275–280, 2015.

[11] D. A. Lopes, A. Benarosch, S. Middleburgh, and K. D. Johnson, "Spark plasma sintering and microstructural analysis of pure and Mo doped U_3Si_2 pellets," *Journal of Nuclear Materials*, vol. 496, pp. 234–241, 2017.

[12] R. E. Hoggan, K. R. Tolman, F. Cappia, A. R. Wagner, and J. M. Harp, "Grain size and phase purity characterization of U_3Si_2 fuel pellets," *Journal of Nuclear Materials*, vol. 512, pp. 199–213, 2018.

[13] J. Buckley, D. T. Goddar, and T. J. Abram, "Studies on the spark plasma sintering of U_3Si_2: Processing parameters and interactions," *Journal of Nuclear Materials*, vol. 544, p. 152655, 2021.

[14] T. M. Besmann, D. Shin, and T. B. Lindemer, "Uranium nitride as LWR TRISO fuel: Thermodynamic modeling of U–C–N," *Journal of Nuclear Materials*, vol. 427, pp. 162–168, 2012.

[15] K. D. Johnson, J. Wallenius, M. Jolkkonen, and A. Claisse, "Spark plasma sintering and porosity studies of uranium nitride," *Journal of Nuclear Materials*, vol. 473, pp. 13–17, 2016.

[16] K. D. Johnson and D. A. Lopes, "Grain growth in uranium nitride prepared by spark plasma sintering," *Journal of Nuclear Materials*, vol. 503, pp. 75–80, 2018.

[17] K. A. Terrani, B. C. Jolly, and J. M. Harp, "Uranium nitride tristructural-isotropic fuel particle," *Journal of Nuclear Materials*, vol. 531, p. 152034, 2020.

[18] K. Yang, E. Kardoulaki, D. Zhao, A. Broussard, K. Metzger, J. T. White, M. R. Sivack, K. J. Mcclellan, E. J. Lahoda, and J. Lian, "Uranium nitride (UN) pellets with controllable microstructure and phase–fabrication by spark plasma sintering and their thermal-mechanical and oxidation properties," *Journal of Nuclear Materials*, vol. 557, p. 153272, 2021.

[19] K. D. Johnson, A. M. Raftery, D. A. Lopes, and J. Wallenius, "Fabrication and microstructural analysis of UN-U_3Si_2 composites for accident tolerant fuel application," *Journal of Nuclear Materials*, vol. 477, pp. 18–23, 2016.

[20] J. T. White, A. W. Travis, J. T. Dunwoody, and A. T. Nelson, "Fabrication and thermophysical property characterization of UN/U_3Si_2 composite fuel forms," *Journal of Nuclear Materials*, vol. 495, pp. 463–474, 2017.

[21] B. Gong, E. Kardoulaki, K. Yang, A. Broussard, D. Zhao, K. Metzger, J. T. White, M. R. Sivack, K. J. Mcclellan, E. J. Lahoda, and J. Lian, "UN and U_3Si_2 composites densified by spark plasma sintering for accident-tolerant fuels," *Ceramics International*, vol. 48, pp. 10762–10769, 2022.

[22] W. Zhou, R. Liu, and S. T. Revankar, "Fabrication methods and thermal hydraulics analysis of enhanced thermal conductivity UO_2–BeO fuel in light water reactors," *Annals of Nuclear Energy*, vol. 81, pp. 240–248, 2015.

[23] S. Yeo, R. Baney, G. Subhash, and J. Tulenko, "The influence of SiC particle size and volume fraction on the thermal conductivity of spark plasma sintered UO_2–SiC composites," *Journal of Nuclear Materials*, vol. 442, pp. 245–252, 2013.

[24] D.-J. Kim, Y. W. Rhee, J. H. Kim, K. S. Kim, J. S. Oh, J. H. Yang, Y.-H. Koo, and K.-W. Song, "Fabrication of micro-cell UO_2–Mo pellet with enhanced thermal conductivity," *Journal of Nuclear Materials*, vol. 462, pp. 289–295, 2015.

[25] C. M. Silva, R. D. Hunt, and K. S. Holliday, "An evaluation of tri-valent oxide (Cr_2O_3) as a grain enlarging dopant for UO_2 nuclear fuels fabricated under reducing environment," *Journal of Nuclear Materials*, vol. 553, p. 153053, 2021.

[26] Z. Chen, G. Subhash, and J. S. Tulenko, "Raman spectroscopic investigation of graphitization of diamond during spark plasma sintering of UO_2-diamond composite nuclear fuel," *Journal of Nuclear Materials*, vol. 475, pp. 1–5, 2016.

[27] J. K. Watkins, A. R. Wagner, S. C. Middlemas, M. C. Marshall, K. Metzger, and B. J. Jaques, "Enhancing thermal conductivity of UO_2 with the addition of UB_2 via conventional sintering techniques," *Journal of Nuclear Materials*, vol. 559, p. 153421, 2022.

[28] A. T. Nelson, A. Migdisov, E. S. Wood, and C. J. Grote, "U_3Si_2 behavior in H_2O environments: Part II, pressurized water with controlled redox chemistry," *Journal of Nuclear Materials*, vol. 500, pp. 81–91, 2018.

[29] E. S. Wood, J. T. White, C. J. Grote, and A. Nelson, "U_3Si_2 behavior in H_2O: Part I, flowing steam and the effect of hydrogen," *Journal of Nuclear Materials*, vol. 501, pp. 404–412, 2018.

[30] R. Harrison, C. Gasparrini, R. N. Worth, J. Buckley, M. R. Wenman, and T. Abram, "On the oxidation mechanism of U_3Si_2 accident tolerant nuclear fuel," *Corrosion Science*, vol. 174, p. 108822, 2020.

[31] J. H. Yang, D. S. Kim, D.-J. Kim, S. Kim, J.-H. Yoon, H. S. Lee, Y.-H. Koo, and K. W. Song, "Oxidation and phase separation of U_3Si_2 nuclear fuel in high-temperature steam environments," *Journal of Nuclear Materials*, vol. 542, p. 152517, 2020.

[32] J. E. Antill and B. L. Myatt, "Kinetics of the oxidation of UN and U(CO) in carbon dioxide, steam and water at elevated temperatures," *Corrosion Science*, vol. 6, pp. 17–23, 1966.

[33] G. A. R. Rao, S. K. Mukerjee, V. N. Vaidya, V. Venugopal, and D. D. Sood, "Oxidation and hydrolysis kinetic studies on UN," *Journal of Nuclear Materials*, vol. 185, pp. 231–241, 1991.

[34] J. K. Watkins, D. P. Butt, and B. J. Jaques, "Microstructural degradation of UN and UN-UO_2 composites in hydrothermal oxidation conditions," *Journal of Nuclear Materials*, vol. 518, pp. 30–40, 2019.

[35] K. Yang, E. Kardoulaki, D. Zhao, A. Broussard, K. Metzger, J. T. White, M. R. Sivack, K. J. Mcclellan, E. J. Lahoda, and J. Lian, "Uranium nitride (UN) pellets with controllable microstructure and phase – fabrication by spark plasma sintering and their thermal-mechanical and oxidation properties," *Journal of Nuclear Materials*, vol. 557, p. 153272, 2021.

[36] D. Manara, C. Ronchi, M. Sheindlin, M. Lewis, and M. Brykin, "Melting of stoichiometric and hyperstoichiometric uranium dioxide," *Journal of Nuclear Materials*, vol. 342, pp. 148–163, 2005.

[37] M. Ugajin and A. Itoh, "Experimental investigations on the chemical state of solid fission-product elements in U_3Si_2," *Journal of Alloys and Compounds*, vol. 213, pp. 369–371, 1994.

[38] U. C. Nunez, D. Prieur, R. Bohler, and D. Manara, "Melting point determination of uranium nitride and uranium plutonium nitride: A laser heating study," *Journal of Nuclear Materials*, vol. 449, pp. 1–8, 2014.

[39] R. E. Rundle, A. S. Wilson, N. C. Baenziger, and R. A. McDonald, "The structures of the carbides, nitrides and oxides of uranium," *Journal of the American Chemical Society*, vol. 70, pp. 99–105, 1948.

[40] A. R. Wagner, J. M. Harp, K. E. Archibald, S. C. Ashby, J. K. Watkins, and K. R. Tolman, "Fabrication of stoichiometric U_3Si_2 fuel pellets," *MethodsX*, vol. 6, pp. 1252–1260, 2019.

[41] C. Ronchi, M. Sheindlin, and M. Musella, "Thermal conductivity of uranium dioxide up to 2900 K from simultaneous measurement of the heat capacity and thermal diffusivity," *Journal of Applied Physics*, vol. 85, pp. 776–789, 1999.

[42] S. L. Hayes, J. K. Thomas, and K. I. Peddicord, "Material property correlations for uranium mononitride III. Transport properties," *Journal of Nuclear Materials*, vol. 171, pp. 289–299, 1990.

[43] Y. Mishchenko, K. D. Johnson, J. Wallenius, and D. A. Lopes, "Design and fabrication of UN composites: From first principles to pellet production," *Journal of Nuclear Materials*, vol. 553, p. 153047, 2021.

[44] Y. Mishchenko, K. D. Johnson, D. Jädernäs, J. Wallenius, and D. A. Lopes, "Uranium nitride advanced fuel: an evaluation of the oxidation resistance of coated and doped grains," *Journal of Nuclear Materials*, vol. 556, p. 153249, 2021.

[45] K. Yang, E. Kardoulaki, D. Zhao, B. Gong, A. Broussard, K. Metzger, J. T. White, M. R. Sivack, K. J. Mcclellan, E. J. Lahoda, and J. Lian, "Cr-incorporated uranium nitride composite fuels with enhanced mechanical performance and oxidation resistance," *Journal of Nuclear Materials*, vol. 559, p. 153486, 2022.

[46] T. J. Davies and P. E. Evans, "The preparation and examination of mixtures of aluminium nitride (AlN) and uranium monotride (UN)," *Journal of Nuclear Materials*, vol. 13, pp. 152–168, 1964.

[47] J. H. Yang, D.-J. Kim, K. S. Kim, and Y.-H. Koo, "UO_2-UN composites with enhanced uranium density and thermal conductivity," *Journal of Nuclear Materials*, vol. 465, pp. 509–515, 2015.

[48] B. J. Jaques, J. Watkins, J. R. Croteau, G. A. Alanko, B. Tyburska-Püschel, M. Meyer, P. Xu, E. J. Lahoda, and D. P. But, "Synthesis and sintering of UN-UO_2 fuel composites," *Journal of Nuclear Materials*, vol. 466, pp. 745–754, 2015.

[49] Y. Mishchenko, *Composite UN-UO_2 fuels*. Master thesis in Nuclear Energy Engineering, KTH Royal Institute of Technology, Stockholm, Sweden, 2018.

[50] R. J. McEachern and P. Taylor, "A review of the oxidation of uranium dioxide at temperatures below 400°C," *Journal of Nuclear Materials*, vol. 254, pp. 87–121, 1998.

[51] J. Rest, M. W. D. Cooper, J. Spino, J. A. Turnbull, P. V. Uffelen, and C. T. Walker, "Fission gas release from UO_2 nuclear fuel: A review," *Journal of Nuclear Materials*, vol. 513, pp. 310–345, 2019.

[52] J. K. Fink, "Thermophysical properties of uranium dioxide," *Journal of Nuclear Materials*, vol. 279, pp. 1–18, 2000.

[53] P. Malkki, *The manufacturing of uranium nitride for possible use in light water reactors*. Licentiate thesis in Reactor Physics, KTH Royal Institute of Technology, Stockholm, Sweden, 2018.

[54] A. P. Shivprasad, A. C. Telles, and J. T. White, "Report on waterproofing of UN studies," Tech. Rep. LA-UR-19-28422, Los Alamos National Laboratory (LANL), September 2019.

[55] R. B. Matthews, "Irradiation performance of nitride fuels," in *Proceedings of Specialist Conference on Space Nuclear Power and Propulsion Technologies - Materials and Fuels*, (Podolsk-Moscow, Russia), pp. 1–14, 1993.

[56] J. Zakova and J. Wallenius, "Fuel residence time in BWRs with nitride fuels," *Annals of Nuclear Energy*, vol. 47, pp. 182–191, 2012.

[57] G. J. Youinou and R. S. Sen, "Impact of accident-tolerant fuels and claddings on the overall fuel cycle: A preliminary systems Analysis," *Nuclear Technology*, vol. 188, pp. 123–138, 2017.

[58] H. Zhao, D. Zhu, K. S. Chaudri, S. Qiu, W. Tian, and G. Su, "Preliminary transient thermal-hydraulic analysis for new coated UN and UC fuel options in SCWR," *Progress in Nuclear Energy*, vol. 71, pp. 152–159, 2014.

[59] R. B. Matthews, K. M. Chidester, C. W. Hoth, R. E. Mason, and R. L. Petty, "Fabrication and testing of uranium nitride fuel for space power reactors," *Journal of Nuclear Materials*, vol. 151, pp. 334–344, 1998.

[60] M.-C. Lee and C.-J. Wu, "Conversion of UF_6 to UO_2: a quasi-optimization of the ammonium uranyl carbonate process," *Journal of Nuclear Materials*, vol. 185, pp. 190–201, 1991.

[61] C. Ekberg, D. R. Costa, M. Hedberg, and M. Jolkkonen, "Nitride fuel for Gen IV nuclear power systems," *Journal of Radioanalytical and Nuclear Chemistry*, vol. 318, pp. 1713–1725, 2018.

[62] M. Hedberg, M. Cologna, A. Cambriani, J. Somers, and C. Ekberg, "Zirconium carbonitride pellets by internal sol gel and spark plasma sintering as inert matrix fuel material," *Journal of Nuclear Materials*, vol. 479, pp. 137–144, 2016.

[63] P. Martin, *Handbook of Deposition Technologies for films and Coatings: Science, Applications and Technology*. Elsevier, third ed., 2016.

[64] D. Tucker, M. Barnes, L. Hone, and S. Cook, "High density, uniformly distributed W/UO_2 for use in Nuclear Thermal Propulsion," *Journal of Nuclear Materials*, vol. 486, pp. 246–249, 2017.

[65] J. Zillinger, B. Segel, K. Benensky, D. Tucker, and M. Barnes, "Investigation of production parameter effects on spark plasma sintered molybdenum cermet wafers for nuclear thermal propulsion applications," in *Proceedings of Nuclear and Emerging Technologies for Space*, (Richland, WA, USA, February 28^{th}), pp. 1–5, 2019.

[66] O. Guillon, J. Gonzalez-Julian, B. Dargatz, T. Kessel, G. Schierning, J. Räthel, and M. Herrmann, "Field-Assisted Sintering Technology/Spark Plasma Sintering: Mechanisms, Materials, and Technology Developments," *Advanced Engineering Materials*, vol. 16, pp. 830–849, 2014.

[67] P. Cavaliere, *Spark Plasma Sintering of Materials: Advances in Processing and Applications*. Springer Nature Switzerland AG, first ed., 2019.

[68] N. M. Harrison, "An Introduction to Density Functional Theory," *Computational Materials Science*, pp. 1–26, 2001.

[69] R. Parr and Y. Weitao, *Density-Functional Theory of Atoms and Molecules*. Oxford Science Publications, first ed., 1989.

[70] A. I. Liechtenstein, V. I. Anisimov, and J. Zaanen, "Density-functional theory and strong interactions: Orbital ordering in Mott-Hubbard insulators," *Physical Review B*, vol. 52, pp. R5467–R, 1995.

[71] A. Claisse, M. Klipfel, N. Lindbom, M. Freyss, and P. Olsson, "GGA+U study of uranium mononitride: A comparison of the U-ramping and occupation matrix schemes and incorporation energies of fission products," *Journal of Nuclear Materials*, vol. 478, pp. 119–124, 2016.

[72] H. Liu, ***Ab initio*** *driven modeling of advanced nuclear fuels*. Doctoral Thesis in Physics/Nuclear Engineering, KTH Royal Institute of Technology, Stockholm, Sweden, 2022.

[73] W. Zimmerman, *Multiphysics Modelling with Finite Element Methods*. World Scientific Publishing Co. Pte. Ltd., first ed., 2006.

[74] B. Cullity, *Elements of X-Ray Diffraction*. Addison-Wesley Publishing Company, second ed., 1978.

[75] B. Warren, *X-Ray Diffraction*. Dover Publications, third ed., 2012.

[76] L. Lutterotti, M. Bortolotti, G. Ischia, I. Lonardelli, and H.-R. Wenk, "Rietveld texture analysis from diffraction images," *Zeitschrift fur Kristallographie, Supplement*, vol. 26, pp. 125–130, 2007.

[77] P. Goodhew, J. Humphreys, and R. Beanland, *Electron Microscopy and Analysis*. Taylor and Francis Books UK, third ed., 2014.

[78] J. Goldstein, D. Newbury, P. Echlin, D. Joy, C. Lyman, E. Lifshin, L. Sawyer, and J. Michael, *Scanning Electron Microscopy and X-Ray Microanalysis*. Springer, third ed., 2003.

[79] D. Williams, J. Goldstein, and D. Newbury, *X-Ray Spectrometry in Electron Beam Instruments*. Springer, first ed., 1995.

[80] A. Schwartz, M. Kumar, B. Adams, and D. Field, *Electron Backscatter Diffraction in Materials Science*. Springer, second ed., 2000.

[81] L. Giannuzzi and F. Stevie, *Introduction to Focused Ion Beams: Instrumentation, Theory, Techniques and Practice*. Springer, first ed., 2005.

[82] P. Gabbott, *Principles and Applications of Thermal Analysis*. Blackwell Publishing Ltd., first ed., 2008.

[83] P. Haines, *Thermal Methods of Analysis: Principles, Applications and Problems*. Springer, first ed., 1995.

[84] R. M. German, *Sintering: from empirical observations to scientific principles.* Butterworth-Heinemann, Oxford, first ed., 2014.

[85] M. Tagawa, "Phase relations and thermodynamic properties of the uranium-nitrogen system," *Journal of Nuclear Materials*, vol. 51, pp. 78–89, 1974.

[86] K. C. Kim and D. R. Olander, "Oxygen diffusion in UO_{2-x}," *Journal of Nuclear Materials*, vol. 102, pp. 192–199, 1981.

[87] R. Smallman and A. Ngan, *Modern Physical Metallurgy.* Elsevier, Oxford, eighth ed., 2014.

[88] J. H. Yang, K. W. Song, K. S. Kim, and Y. H. Jung, "A fabrication technique for a UO_2 pellet consisting of UO_2 grains and a continuous W channel on the grain boundary," *Journal of Nuclear Materials*, vol. 353, pp. 202–208, 2006.

[89] P. D. Takkunen, "Fabrication of cermets of uranium nitride and tungsten or molybdenum from mixed powders and from coated particles," Tech. Rep. NASA-TN-D-5136, NASA Lewis Research Center Cleveland, April 1969.

[90] V. G. Baranov, A. V. Tenishev, R. S. Kuzmin, S. A. Pokrovskiy, V. V. Mikhalchik, V. Astafyev, M. L. Taubin, and E. S. Solntseva, "Thermal stability investigation technique for uranium nitride," *Annals of Nuclear Energy*, vol. 87, pp. 784–792, 2016.

[91] C. Politis, F. Thümmler, and H. Wedemeyer, "Untersuchungen in den systemen uranmononitrid-molybdän und uranmononitrid-wolfram bei hohen temperaturen," *Journal of Nuclear Materials*, vol. 38, pp. 132–142, 1971.

[92] W. F. Cureton, J. Zillinger, J. Rosales, R. P. Wilkerson, M. Lang, and M. Barnes, "Microstructural evolution of Mo-UO_2 cermets under high temperature hydrogen environments," *Journal of Nuclear Materials*, vol. 538, p. 152297, 2020.

[93] L. Cheng, R. Gao, B. Yan, C. Zhang, R. Li, C. Ma, Z. Yang, B. Li, Y. Wang, Y. Zhong, M. Chu, B. Bai, and P. Zhang, "Investigation of the residual stress in UO_2-Mo composites via a neutron diffraction method," *Ceramics International*, vol. 46, pp. 15889–15896, 2020.

[94] M. K. Tummalapalli, J. A. Szpunar, A. Prasad, and L. Bichler, "EBSD studies on microstructure and crystallographic orientation of UO_2-Mo composite fuels," *Nuclear Engineering and Technology*, vol. 53, pp. 4052–4059, 2021.

[95] J. K. Fink, "Thermophysical properties of uranium dioxide," *Journal of Nuclear Materials*, vol. 279, pp. 1–18, 2000.

[96] K. Wang and R. R. Reeber, "The role of defects on thermophysical properties: thermal expansion of V, Nb, Ta, Mo and W," *Materials Science and Engineering*, vol. 23, pp. 101–137, 1998.

[97] A. M. Raftery, R. Seibert, D. Brown, M. Trammell, A. Nelson, and K. Terrani, "Fabrication of un-mo cermet nuclear fuel using advanced manufacturing techniques," in *Proceedings of Nuclear and Emerging Technologies for Space - Track 2: Nuclear Fission Power and Propulsion*, (Knoxville, TN, USA, April 6^{th} - 9^{th}), pp. 118–122, 2020.

[98] P. Garg, S. J. Park, and R. M. German, "Effect of die compaction pressure on densification behavior of molybdenum powders," *International Journal of Refractory Metals and Hard Materials*, vol. 25, pp. 16–24, 2007.

[99] G. S. Kim, H. G. Kim, D. G. Kim, S. T. Oh, M. J. Suk, and Y. D. Kim, "Densification behavior of Mo nanopowders prepared by mechanochemical processing," *Journal of Alloys and Compounds*, vol. 469, pp. 401–405, 2009.

[100] G. D. Sun, G. Zhang, and K. C. Chou, "An industrially feasible pathway for preparation of Mo nanopowder and its sintering behavior," *International Journal of Refractory Metals and Hard Materials*, vol. 84, p. 105039, 2019.

[101] N. Senthilnathan, A. R. Annamalai, and G. Venkatachalam, "Synthesis of tungsten through spark plasma and conventional sintering processes," *Materials Today: Proceedings*, vol. 5, pp. 7954–7959, 2018.

[102] J. M. Byun, E. S. Lee, Y. J. Heo, Y. K. Jeong, and S. T. Oh, "Consolidation and properties of tungsten by spark plasma sintering and hot isostatic pressing," *International Journal of Refractory Metals and Hard Materials*, vol. 99, p. 105602, 2021.

[103] S. K. Chen, J. H. Du, G. R. Gao, and Z. X. Li, "Microstructure study of CVD W coating on Mo single crystal rods with <111> axial orientation by EBSD," *Materials Science and Engineering: A*, vol. 434, pp. 95–98, 2006.

[104] J. Song, Y. Lian, Y. Lv, J. Liu, Y. Yu, X. Liu, B. Yan, Z. Chen, Z. Zhuang, X. Zhao, and Y. Qi, "Development of CVD-W coatings on CuCrZr and graphite substrates with a PVD intermediate layer," *Journal of Nuclear Materials*, vol. 455, pp. 531–536, 2014.

[105] Y. Lv, J. Song, Y. Lian, Y. Yu, X. Liu, and Z. Zhuang, "The thermal properties of high purity and fully dense tungsten produced by chemical vapor deposition," *Journal of Nuclear Materials*, vol. 457, pp. 317–323, 2015.

[106] M. H. A. Piro, D. Sunderland, S. Livingstone, J. Sercombe, R. W. Revie, A. Quastel, K. A. Terrani, and C. Judge, "2.09 - Pellet-clad interaction behavior in zirconium alloy fuel cladding," *Comprehensive Nuclear Materials*, vol. 2, pp. 248–306, 2020.

[107] H. Gietl, J. Riesch, J. W. Coenen, T. Höschen, and R. Neu, "Production of tungsten-fibre reinforced tungsten composites by a novel continuous chemical vapour deposition process," *Fusion Engineering and Design*, vol. 146, pp. 1426–1430, 2019.

[108] Y. Lian, X. Liu, J. Wang, F. Feng, Y. Lv, J. Song, and J. Chen, "Influence of surface morphology and microstructure on performance of CVD tungsten coating under fusion transient thermal loads," *Applied Surface Science*, vol. 390, pp. 167–174, 2016.

[109] J. D. Murphy, A. Giannattasio, Z. Yao, C. J. D. Hetherington, P. Nellist, and S. G. Roberts, "The mechanical properties of tungsten grown by chemical vapour deposition," *Journal of Nuclear Materials*, vol. 586, pp. 583–586, 2009.

[110] Y. Lian, F. Feng, J. Wang, X. Liu, J. Song, Y. Wang, Z. Chen, and J. Chen, "Effect of high temperature annealing on the microstructure and thermal shock resistance of tungsten coatings grown by chemical vapor deposition," *Journal of Nuclear Materials*, vol. 513, pp. 241–250, 2019.

[111] M. Khan, M. Islam, A. Akram, Z. Qi, and L. Li, "Residual strain and electrical resistivity dependence of molybdenum films on DC plasma magnetron sputtering conditions," *Materials Science in Semiconductor Processing*, vol. 27, pp. 343–351, 2014.

[112] M. Andritschky and V. Teixeira, "Residual stress and adhesion of molybdenum coatings produced by magnetron sputtering," *Vacuum*, vol. 43, pp. 455–458, 1992.

[113] P. Chelvanathan, S. A. Shahahmadi, F. Arith, K. Sobayel, M. Aktharuzzaman, K. Sopian, F. H. Alharbi, N. Tabet, and N. Amin, "Effects of RF magnetron sputtering deposition process parameters on the properties of molybdenum thin films," *Thin Solid Films*, vol. 638, pp. 213–219, 2017.

[114] H. Rashid, K. S. Rahman, M. I. Hossain, A. A. Nasser, F. H. Alharbi, M. Akhtaruzzaman, and N. Amin, "Physical and electrical properties of molybdenum thin films grown by DC magnetron sputtering for photovoltaic application," *Results in Physics*, vol. 14, p. 102515, 2019.

[115] A. M. Minkin and V. M. Kozlov, "Preferred growth of molybdenum thin films during magnetron sputtering," *Journal of Solid State Chemistry*, vol. 304, p. 122543, 2021.

[116] J. A. Thornton and D. W. Hoffman, "Stress-related effects in thin films," *Thin Solid Films*, vol. 171, pp. 5–31, 1989.

[117] T. Ganne, J. Crépin, S. Serror, and A. Zaoui, "Cracking behaviour of PVD tungsten coatings deposited on steel substrates," *Acta Materialia*, vol. 50, pp. 4149–4163, 2002.

[118] K. Bouziane, M. Mamor, and F. Meyer, "DC magnetron sputtered tungsten: W film properties and electrical properties of W/Si Schottky diodes," *Applied Physics A*, vol. 81, pp. 209–215, 2005.

[119] R. Ohser-Wiedemann, U. Martin, H. J. Seifert, and A. Müller, "Densification behaviour of pure molybdenum powder by spark plasma sintering," *International Journal of Refractory Metals and Hard Materials*, vol. 28, pp. 550–557, 2010.

[120] S. Deng, H. Zhao, R. Li, T. Yuan, L. Li, and P. Cao, "The influence of the local effect of electric current on densification of tungsten powder during spark plasma sintering," *Powder Technology*, vol. 356, pp. 769–777, 2019.

[121] J. Matějíček, J. Veverka, C. Yin, M. Vilémová, D. Terentyev, M. Wirtz, M. Gago, A. Dubinko, and H. Hadraba, "Spark plasma sintered tungsten – mechanical properties, irradiation effects and thermal shock performance," *Journal of Nuclear Materials*, vol. 542, p. 152518, 2020.

[122] H. C. Kim, E. Bang, N. Kwak, Y. Oh, H. N. Han, H. Choi, K. Kim, and S. H. Hong, "Thermal and microstructural properties of spark plasma sintered tungsten for the application to plasma facing materials," *Fusion Engineering and Design*, vol. 146, pp. 2649–2653, 2019.

[123] J. Choi, H. M. Sung, K. B. Roh, S. H. Hong, G. H. Kim, and H. N. Han, "Fabrication of sintered tungsten by spark plasma sintering and investigation of thermal stability," *International Journal of Refractory Metals and Hard Materials*, vol. 69, pp. 164–169, 2017.

[124] J. R. Creighton, "The surface chemistry and kinetics of tungsten chemical vapor deposition and selectivity loss," *Thin Solid Films*, vol. 241, pp. 310–317, 1994.

[125] L. Raumann, J. W. Coenen, J. Riesch, Y. Mao, D. Schwalenberg, T. Wegener, H. Gietl, T. Höschen, C. Linsmeier, and O. Guillon, "Modeling and experimental validation of a W_f/W-fabrication by chemical vapor deposition and infiltration," *Nuclear Materials and Energy*, vol. 28, p. 101048, 2021.

[126] L. Raumann, J. W. Coenen, J. Riesch, Y. Mao, D. Schwalenberg, H. Gietl, C. Linsmeier, and O. Guillon, "Improving the W coating uniformity by a COMSOL model-based CVD parameter study for denser W_f/W composites," *Metals*, vol. 11, pp. 1089–1104, 2021.

[127] C. B. Carter and M. G. Norton, *Ceramic Materials: Science and Engineering*. Springer Science+Business Media, LLC, second ed., 2013.

[128] F. M. A. Carpay, S. Mahajan, G. Y. Chin, and J. J. Rubin, "Slip-induced cracking in molybdenum single crystals," *Scripta Metallurgica*, vol. 9, pp. 451–457, 1975.

[129] J.-S. Wang and P. M. Anderson, "Fracture behavior of embrittled F.C.C. metal bicrystals," *Acta Metallurgica et Materialia*, vol. 39, pp. 779–792, 1991.

[130] D. M. Bond and M. A. Zikry, "Differentiating between intergranular and transgranular fracture in polycrystalline aggregates," *Journal of Materials Science*, vol. 53, pp. 5786–5798, 2018.

[131] R. J. McEachern, "A review of kinetic data on the rate of U_3O_7 formation on UO_2," *Journal of Nuclear Materials*, vol. 245, pp. 238–247, 1997.

[132] F. Valdivieso, V. Francon, F. Byasson, M. Pijolat, A. Feugier, and V. Peres, "Oxidation behaviour of unirradiated sintered UO_2 pellets and powder at different oxygen partial pressures, above 350°C," *Journal of Nuclear Materials*, vol. 354, pp. 85–93, 2006.

[133] L. Quémard, L. Desgranges, V. Bouineau, M. Pijolat, G. Baldinozzi, N. Millot, J.-C. Nièpce, and P. Arnaud, "On the origin of the sigmoid shape in the UO_2 oxidation weight gain curves," *Journal of the European Ceramic Society*, vol. 29, pp. 2791–2798, 2009.

[134] P. Taylor, D. D. Wood, and A. M. Duclos, "The early stages of U_3O_8 formation on unirradiated CANDU UO_2 fuel oxidized in air at 200-300°C," *Journal of Nuclear Materials*, vol. 189, pp. 116–123, 1992.

[135] R. Dell and V. Wheeler, "The ignition of uranium mononitride and uranium monocarbide in oxygen," *Journal of Nuclear Materials*, vol. 21, pp. 328–336, 1967.